Experimentelle Physik

Dissertationsthema

Lifetime analysis of the HFS states in hydrogen- and lithium-like bismuth and development of an in-beam detection system for extreme UV photons

Inaugural-Dissertation
zur Erlangung des Doktorgrades
der Naturwissenschaften im Fachbereich Physik
der Mathematisch-Naturwissenschaftlichen Fakultät
der Westfälischen Wilhelms-Universität

vorgelegt von
Jonas Vollbrecht, geb. Mader
aus Münster

- 2016 -

Dekan:	Prof. Dr. Chr. Weinheimer
Erster Gutachter:	Prof. Dr. Chr. Weinheimer
Zweiter Gutachter:	Apl. Prof. Dr. A. Khoukaz

Tag der mündlichen Prüfung:	29.06.2016
Tag der Promotion:	29.06.2016

Abstract

The LIBELLE experiment contributes to a better understanding of bound state quantum electrodynamics in extreme fields. For that purpose highly charged bismuth ions in hydrogen- or lithium-like electron configurations were stored in the Experimental Storage Ring (ESR) at the "Gesellschaft für Schwerionenphysik" (GSI) in Darmstadt. The remaining electrons experience high electric and magnetic field strengths in the vicinity of the nucleus, which by far exceed the fields, that can be generated in the laboratory via pulsed lasers or superconducting magnets. A method to test QED predictions in these systems without being hampered by uncertainties due to the nuclear structure contributions has been suggested by Shabaev and coworkers [SAY$^+$01]. It is based on a comparison of hyperfine structure (HFS) splittings in hydrogen-like and lithium-like configurations of the same isotope. The respective transition wavelengths of the hyperfine splittings in bismuth were determined in two LIBELLE beam times by the means of collinear, and anti-collinear laser spectroscopy. The experiment provided the first successful observation of the HFS transition in $^{209}Bi^{80+}$in a laser spectroscopy measurement [LJG$^+$14]. In addition the lifetimes of the excited HFS states were measured and the analysis of the lifetime data is presented in this work. While systematic uncertainties in the measured lifetime were discussed only hypothetically before, data taken to investigate the systematics of the transition wavelength measurement also allows in a limited way, to look at possible systematic effects in the lifetime. Here the influence of the bunching amplitude, the electron cooler current and the ion beam current on the lifetime are investigated.

Furthermore a calculation of the bound electron g-factor is presented. For that purpose the transition energy as well as the lifetime of the HFS state of the respective species needs to be known. To be able to identify the QED contribution to the g-factor the lifetime has to be measured with a precision of about $\frac{\Delta\tau}{\tau} < 0.2$ %.

While the transition wavelength in hydrogen-like bismuth was already observed before, a novel detector system was mandatory to successfully measure the HFS transition wavelength and lifetime in lithium-like bismuth [HAG$^+$13]. The success of this measurement inspired the adaption of the movable mirror system to detect extreme ultra-violet (XUV) fluorescence photons. The design of the new detector, corresponding

simulations with the software package SimIon as well as the realization were part of this work. First tests were performed and compared to simulations, resulting in a good understanding of the new system. For the further development of the detector some possible improvements are identified.

Zusammenfassung

Das LIBELLE Experiment hat zum besseren Verständnis der Quantenelektrodynamik (QED) gebundener Zustände in extremen Feldern beigetragen. Zu diesem Zweck wurden hoch geladene Ionen in Wasserstoff- oder Lithium-ähnlicher Elektronenkonfiguration im Experimentellen Speicher Ring (ESR) der Gesellschaft für Schwerionenphysik (GSI) in Darmstadt gespeichert. Die verbleibenden Elektronen erfahren in der Nähe des Kerns hohe elektrische und magnetische Feldstärken, welche jene Felder übersteigen, die durch gepulste Laser oder supraleitende Magnete im Labor erzeugt werden können. Eine Möglichkeit, die Vorhersagen der QED in solchen Systemen zu testen, ohne durch Unsicherheiten gehindert zu sein, die durch Beiträge der Kernstruktur eingeführt werden, wurde von Shabaev und Mitarbeitern vorgeschlagen [SAY$^+$01]. Es basiert auf einem Vergleich der Hyperfeinstruktur (HFS) Aufspaltungen des gleichen Isotops einmal in Wasserstoff- und einmal in Lithium-ähnlicher Elektronenkonfiguration. Die jeweilige Übergangswellenlänge der Hyperfeinaufspaltungen wurde in zwei LIBELLE Strahlzeiten mit Hilfe von kollinearer bzw. anti-kollinearer Laserspektroskopie bestimmt. Mit dem Experiment wurde zum ersten mal erfolgreich der HFS-Übergang in $^{209}Bi^{80+}$durch eine laserspektroskopische Messung beobachtet [LJG$^+$14]. Zusätzlich wurde die Lebensdauer der angeregten HFS-Zustände gemessen, die Analyse der Lebensdauer-Daten wird in dieser Arbeit vorgestellt.

Während systematische Unsicherheiten bisher nur hypothetisch diskutiert wurden, erlauben die aufgezeichneten Daten zur Bestimmung systematischer Unsicherheiten bezüglich der Übergangswellenlänge im begrenzten Maße eine Möglichkeit systematische Effekte bzgl. der Lebensdauer zu betrachten. Hier konnte der Einfluss der Bunch-Amplitude, des Elektronen-Kühler Stroms und des Ionenstrahl Stroms auf die Lebensdauer untersucht werden.

Darüber hinaus wird die Berechnung des g-Faktors des gebundenen Valenzelektrons vorgestellt. Für diesen Zweck wird sowohl die Übergangswellenlänge, als auch die Lebensdauer des HFS-Zustands der jeweiligen Bismut-Spezies benötigt. Um in der Lage zu sein, die Beiträge der QED zum g-Faktor identifizieren zu können, muss die Lebensdauer mit einer Präzision von ungefähr $\frac{\Delta\tau}{\tau} < 0.2$ % gemessen werden.

Auch wenn die Übergangswellenlänge in Wasserstoff-ähnlichem Bismut bereits zuvor

beobachtet wurde, war ein neuartiges Nachweissystem zwingend notwendig, um die HFS-Übergangswellenlänge und die Lebensdauer von Lithium-ähnlichem Bismut erfolgreich messen zu können [HAG$^+$13]. Der Erfolg dieser Messungen inspirierte zu einer Weiterentwicklung des beweglichen Spiegel-Systems, um Photonen im extremen ultra-violetten (XUV) Bereich messen zu können. Das Design des neuen Detektorsystems, dazugehörige Simulationen mit dem Softwarepaket SimIon, sowie die Realisierung des Aufbaus sind Teil dieser Arbeit. Erste Tests wurden durchgeführt und mit den Ergebnissen der Simulationen verglichen. Die Ergebnisse deuten darauf hin, dass das neue System gut verstanden ist. Für die Weiterentwicklung des Detektorsystems konnten Möglichkeiten, für Verbesserungen ausgemacht werden.

CONTENTS

1 Introduction **1**

2 Hyperfine transitions in highly charged ions **7**

2.1 Energy splitting, transition probability and lifetimes 8

2.1.1 Hyperfine structure 11

2.1.2 Transition probabilities and lifetimes 12

2.1.3 HFS splitting for high Z, few electron ions 14

2.2 Tests of bound state QED in strong fields 17

2.2.1 The specific difference 17

2.2.2 g-factor determination 19

3 The experimental set-up **23**

3.1 The GSI accelerator structure 23

3.2 The experimental storage ring ESR 24

3.3 The LIBELLE experiment 24

3.3.1 Laser system 26

3.3.2 Detection systems 29

3.3.3 Data acquisition (DAQ) 32

3.4 Beam time 2011 33

3.5 Beam time 2014 34

3.5.1 DAQ load test 34

4 Lifetime analysis **37**

4.1 Basic data structure . . . 37

4.1.1 Ion current . . . 38

4.1.2 Accumulation of signal and reference data . . . 38

4.2 Extraction of lifetime curves . . . 41

4.2.1 Fit method . . . 42

4.2.2 Bin method . . . 43

4.2.3 Comparison of both methods . . . 45

4.2.4 Offset of lifetime curves for the Li-like HFS state . . . 46

4.3 Beam time 2011 . . . 48

4.3.1 Lifetime analysis . . . 48

4.3.2 Transformation into the ion's rest frame . . . 51

4.4 Beam time 2014 . . . 52

4.4.1 The Lorentz factor . . . 52

4.4.2 Laser light leak . . . 53

4.4.3 Evaluation of scan mode data . . . 57

4.4.4 Lifetime of hydrogen-like bismuth . . . 57

4.4.5 Systematic effects for $^{209}Bi^{82+}$ . . . 62

4.4.6 Lifetime of lithium-like bismuth . . . 67

4.4.7 Systematic effects for $^{209}Bi^{80+}$ . . . 73

4.5 Final results of the lifetime analysis . . . 75

4.5.1 H-like bismuth . . . 76

4.5.2 Li-like bismuth . . . 77

4.5.3 Extraction of the g-factor . . . 77

5 Adaption for XUV laser spectroscopy **81**

5.1 Motivation . . . 81

5.2 Modified detection system . . . 82

5.2.1 Electrode configuration . . . 85

5.2.2 Magnetic guidance . . . 85

5.2.3 Micro-Channel-Plate detector . . . 87

5.3 Simulation tool SimIon . . . 89

5.4 First commissioning and simulations 90
5.4.1 Magnetic field optimization 96
5.4.2 Photo-cathode potential optimization 99
5.4.3 Time of flight 100

6 Conclusion and outlook **105**

Appendix **109**
A.1 Cabling of the LIBELLE experiment 110
A.2 Implemented fit function with laser pulses 111
A.3 Result comparison of two fit models 112
A.4 Technical drawing of the XUV detection system 113

Bibliography **115**

CHAPTER 1

INTRODUCTION

Already in 1913 Nils Bohr very successfully described the hydrogen atom with his orbit model, improving the understanding of atomic structure. Further on it was used as base for more advanced models, due to its unpretentious structure. With more and more sophisticated experiments, the energy levels in the atom were studied in detail and discrepancies to theoretical predictions were found. Thus the hydrogen atom played an essential role for the establishment of the theories of quantum-mechanics (QM) and quantum-electrodynamics (QED). Although QED is to the present day one of the best tested theories, there are still shortcomings which need to be investigated. QED describes for example very well the energy levels and there splitting up to the tiny energy difference of the hyperfine structure (HFS). But so far, most of the experiments and corresponding calculations were limited to conditions with moderate electric and magnetic fields. Therefore the examination of hydrogen-like atomic configurations and their HFS splitting in extreme fields is the natural next step to take to test bound-state QED. Such extreme fields, which exceed even field strength generated in the laboratory using lasers or superconducting magnets, are present in highly charged ions (HCI). For example the single 1s electron in an otherwise bare bismuth atom experiences electric and

magnetic field strength around 10^{17} V/cm and 10^4 T, respectively [Bei00]. The electric field strength for example can be estimated via Coulomb's law:

$$E = \frac{1}{4\pi\epsilon_0}\frac{Ze^2}{r^2} \tag{1.1}$$

with the electric field constant ϵ_0 the charge number Z and the elementary charge e. The distance between the charge Ze and a point charge e is given by:

$$r = \frac{h^2\epsilon_0}{m_e Ze^2\pi} \cdot n^2 \tag{1.2}$$

with the Planck constant h, the electron mass m_e and the principal quantum number n. For hydrogen-like bismuth, i.e. $Z = 83$ and $n = 1$, the radius is $r \approx 6.4 \cdot 10^{-13}$ m and the electric field is $E = 2.9 \cdot 10^{17}$ V/m. Since it is the only electron, the atom is in a hydrogen-like state, which simplifies the theoretical description, being comparable to the hydrogen atom itself. Of course the much larger nucleus which cannot be treated as a point particle is accompanied with the need of further corrections besides the QED effects of interest, which can be used to obtain a better understanding of nuclear structure. Within these corrections the finite mass, relativistic effects and the charge distribution as well as the magnetic moment distribution are taken into account. The latter, called the Bohr-Weisskopf effect is burdened with a high uncertainty, which is comparable in size to the total contribution of QED corrections and hinders therefore a test of QED. To still be able to make statement about the QED contributions Shabaev and co-workers presented 2001 the so-called specific difference $\Delta E'$ between the HFS splitting in hydrogen-like ($\Delta E^{(\,1s)}$) and lithium-like ($\Delta E^{(2s)}$) electron configurations of the same isotope [SAY+01]

$$\Delta E' = \Delta E^{(2s)} - \xi\Delta E^{(1s)}. \tag{1.3}$$

The parameter ξ can be chosen such, that the contribution of the Bohr-Weisskopf effect approximately cancels out. It is largely independent of the assumed model of nuclear structure and can be calculated with high accuracy.

With the introduction of the specific difference the obstructive influence of the Bohr-Weisskopf effect can be avoided, leading to the additional task to determine the HFS transition wavelength in a lithium-like ion. An ideal candidate for such a measurement

is bismuth, since the transition wavelength of both species is accessible with laser spectroscopy. The transition wavelength for $^{209}Bi^{82+}$is $\lambda^{(1s)} \approx 244$ nm and the lifetime is $\mathcal{O}(\tau^{(1s)}) = 400$ μs. For the case of $^{209}Bi^{80+}$it is $\lambda^{(2s)} \approx 1555$ nm and $\mathcal{O}(\tau^{(2s)}) = 100$ ms, respectively. Two experiments at the Gesellschaft für Schwerionenphysik (GSI) Darmstadt are dedicated to measure both transitions. The SpecTrap experiment will store the bismuth ions of the respective species in a liquid-helium cooled, cylindric Penning trap and perform laser spectroscopy with the ions almost at rest [And12]. With this experimental setup a much higher precision is expected since the uncertainty of the velocity as well as the width of the velocity distribution is vanishingly small. Particularly challenging is then the measurement of the fluorescence photons of the 2s HFS transition due to the long wavelength in combination with a rather long lifetime. The LIBELLE experiment on the other hand stores the respective ions in the experimental storage ring (ESR) at a velocity of about 71 % of the speed of light to measure the transitions. The advantage is, that the transition wavelength is Doppler shifted to a convenient wavelength region for detection. Drawbacks are a reduced accuracy of the determination of the HFS splitting, on the order of $\mathcal{O}(10^{-4})$ due to the uncertainty of the mean velocity and its width and, especially for the lithium-like case, a low signal rate. Besides the long lifetime of the state, which is even longer in the storage ring, due to time dilation by a γ-factor of about 1.4, the difficult collection of fluorescence photons from the transition hinders the detection. While the 1s transition in hydrogen-like bismuth was already measured in the 90's [Kla94, Win99], it took until 2011 to overcome these challenges and find the 2s HFS transition in lithium-like bismuth [Loc13, Jö13]. The major difference to previous beam times, and finally the key to success was the installation of a novel detection system [HAG$^+$13]. It is designed to efficiently collect forward emitted photons to benefit most from the Doppler shift and the Lorentz boost of the emission characteristics. The system contains a movable copper mirror which can be moved in and out of the beam position (cf. chapter 3.3.2). The parabola shaped mirror has a 3 cm slit for the ions to pass through and ideal focal features to send emitted fluorescence photons towards a highly selected, red-enhanced photomultiplier. This new system made the measurement of the lithium-like bismuth transition wavelength, as well as the lifetime of the excited state possible for the first time. Shortcomings in the determination of the ions velocity during the 2011 beam time are connected to unexpectedly high uncertainties of the measured quantities

when transformed to the ions rest frame. Therefore a second beam time was performed in March 2014 with an improved determination of the ions velocity. In this beam time the transition wavelength and lifetimes of the respective species were measured and the uncertainties were improved to the $< 10^{-4}$ level concerning the transition wavelength. Besides a QED test using the specific difference, a second approach is in principle possible involving the lifetimes of the measured HFS states. The transition probability is the reciprocal of the lifetime [SST+98] and is directly connected to the g-factor of the bound electron. By measuring the lifetime precise enough, i.e. $\frac{\Delta\tau}{\tau} \leq 0.2$ %, a test of QED is possible, as well. Since the major task of the LIBELLE experiment was the determination of the transition wavelength, the collected lifetime data will not yield a sufficiently high precision for such a test.

For the successful measurement of the transition wavelength and lifetime of lithium-like bismuth the movable mirror system was mandatory. To make this successful concepts usable for other experiments, like the measurement of the $^3P_0 \rightarrow {}^3P_1$ fine structure transition in Be-like krypton [WKS+11] the detection system was adapted to the XUV wavelength region. While the system used in the LIBELLE experiment was intended for the optical wavelength region, the new system is going to convert fluorescence photons with wavelengths <10 nm to photo-electrons. For this purpose the copper mirror is replaced with a stainless steel cathode as electron source which is movable and has a slit for the ions to pass through, as before. The produced electrons are guided electromagnetically towards a micro-channel-plate detector.

This thesis can be divided into two parts; one is dealing with the lifetime analysis of the HFS states of H-like and Li-like bismuth based on the data obtained with the LIBELLE experiment. The second part is about the design of a detection system for the XUV photons based on the movable mirror concept. Therefore the outline of this thesis is as follows:

- In **chapter 2** the theoretical frame of the LIBELLE experiment is discussed. The hyperfine splitting in atoms is discussed, as well as the transition probability which can be understood as the reciprocal of the lifetime. In addition the lifetime will be

placed in context with the g-factor of the bound electron as a further option of a QED test.

- The LIBELLE experiment will be introduced briefly in **chapter 3**. Especially the aspects important for the lifetime analysis are presented.

- The major part of this thesis, namely the lifetime analysis itself is the content of **chapter 4**. After a short discussion of the data structure with the relevant measured quantities, the two beam-times, 2011 and 2014, are analyzed regarding the lifetime of the two hyperfine states. Together with results from previous theses, namely the wavelength determination of the HFS states, the g-factor can be calculated, which is presented at the end of this chapter.

- The adaption of the detection system to the XUV region is the topic of **chapter 5**. The basic modifications as well as the present realization are explained. The design process was accompanied by simulations with the software package SimIon [Sim15] which will be presented in this chapter, too. The results of the simulations are compared to first commissioning measurements to obtain a better understanding of the new setup.

- In **chapter 6** a short summary and an outlook are given.

CHAPTER 2

HYPERFINE TRANSITIONS IN HIGHLY CHARGED IONS

This chapter provides a summary of the theoretical framework required to interpret the data acquired in the LIBELLE experiment. It deals with level splitting in the atomic shell in general and the hyperfine structure in particular, with special focus on highly charged ions.

The first priority of the experiment was the determination of the 1s hyperfine transition wavelength in hydrogen-like bismuth and the 2s hyperfine transition wavelength in lithium-like bismuth to extract the specific difference $\Delta E'$ required for a test of bound state QED calculations and to pave the way for more precise measurements of the transitions in a Penning trap experiment (SpecTrap). Secondly the lifetime of the respective states is of interest and was measured as well. The main focus of this work is the lifetime analysis, defined as the reciprocal of the transition probability, which is discussed in this chapter too.

For the intended QED studies the transition energy has to be measured. Besides this, the lifetime determination can provide a QED test as well since the lifetime can be connected to the g-factor of the bound electron, as explained at the end of this chapter.

2.1 Energy splitting, transition probability and lifetimes

Nils Bohr's insight into the atomic structure was based on the equality of the electromagnetic and the centripetal force combined with a quantisation of the angular momentum. With this ansatz he was able to derive the energy levels of the hydrogen atom, i.e. an one-electron system. Quantum-mechanically, the equivalent result can be obtained for a hydrogen-like atom via the time-independent Schrödinger equation with the Coulomb potential $V_C(\vec{r})$ for a nucleus of charge Ze and an electron of charge $-e$:

$$E\psi(\vec{r}) = \left\{ -\frac{\hbar^2}{2\mu}\nabla^2 + \underbrace{\frac{(-e)\cdot Ze}{4\pi\epsilon_0 r}}_{:=\, V_C(\vec{r})} \right\} \cdot \psi(\vec{r}) \tag{2.1}$$

with $\hbar = \frac{h}{2\pi}$ and $\mu = \frac{m_e \cdot m_N}{m_e + m_N}$ being the reduced Planck constant and the reduced mass respectively. m_e and m_N are the masses of the electron and the nucleus, respectively. ϵ_0 is the vacuum permittivity. By solving this formula discrete energy levels can be calculated given by the energy eigenvalues

$$E_n = -\underbrace{\frac{1}{2}\mu c^2\alpha^2}_{\equiv\, Ry^*} \cdot \frac{Z^2}{n^2} \tag{2.2}$$

with the fine structure constant α:

$$\alpha = \frac{e^2}{4\pi\epsilon_0\hbar c} \tag{2.3}$$

and the principal quantum number $n \in \mathbb{N}$ [Dem05]. The experimental observations of energy level splitting made extensions of eq. 2.1 necessary. The first splitting observed is called fine structure and contains three contributions, which are introduced by a series expansion of the Dirac equation and are added to the non-relativistic Hamiltonian (eq. 2.1). The three contributions and their corresponding energy shifts are given as:

1. the spin-orbit coupling with

$$\Delta E_1 = -\vec{\mu}_s \cdot \vec{B} = g\mu_B \frac{\mu_0 Ze}{8\pi\hbar m_e \langle r^3 \rangle} (\vec{s}\cdot\vec{l}) \tag{2.4}$$

with $g \approx 2$ and $\mu_B = \frac{e\hbar}{2m_e}$ it yields:

$$\approx \frac{\mu_0 Z e^2}{8\pi m_e^2 \langle r^3 \rangle} (\vec{s} \cdot \vec{l}), \tag{2.5}$$

with the magnetic spin moment of the electron $\vec{\mu}_s = g\mu_B \frac{\vec{s}}{\hbar}$, the magnet field $\vec{B}$ created by the nucleus at the position of the electron and the vacuum permeability μ_0 [HH04]. The scalar product can be written as:

$$(\vec{s} \cdot \vec{l}) = \frac{1}{2}\hbar^2 \left[j(j+1) - l(l+1) - s(s+1) \right] \tag{2.6}$$

which is obtained by squaring the total angular momentum of the electron $\vec{j}$:

$$\vec{j} = \vec{l} + \vec{s} \text{ with } |\vec{j}| = \sqrt{j(j+1)} \cdot \hbar \tag{2.7}$$

Introducing the spin-orbit coupling constant $a = \frac{\mu_0 Z e^2 \hbar^2}{8\pi m_e^2 \langle r^3 \rangle}$ it can be shortened to:

$$\Delta E_1 = \frac{a}{2}[j(j+1) - l(l+1) - s(s+1)]. \tag{2.8}$$

2. a relativistic correction of the kinetic energy with [Dem05]

$$\Delta E_2 = -E_n \frac{(Z\alpha)^2}{n^2} \left(\frac{3}{4} - \frac{n}{l + \frac{1}{2}} \right). \tag{2.9}$$

3. the so-called Darwin term as correction of the potential energy [BHB83]

$$\Delta E_3 = -E_n \frac{(Z\alpha)^2}{n} \delta_{l0}. \tag{2.10}$$

In combination it yields shifts or a fine structure splitting in dependence on the total angular momentum j for a given principal quantum number n [BHB83]:

$$\boxed{E_{n,j} = E_n + \sum \Delta E_i = E_n \left[1 + \frac{(Z\alpha)^2}{n} \left(\frac{1}{j + \frac{1}{2}} - \frac{3}{4n} \right) \right]} \tag{2.11}$$

with $j = l \pm 1/2$ and $l = 0, 1, \ldots, n-1$.

Furthermore the energy levels are slightly shifted due to the interaction of the electron with the quantized electromagnetic field, e.g. the zero-point radiation field. Continuous emission and absorption of virtual photons within a time $\Delta t < \hbar/\Delta E$, like illustrated in fig. 2.1 take place. The actual point like charge becomes a sphere and the mean potential

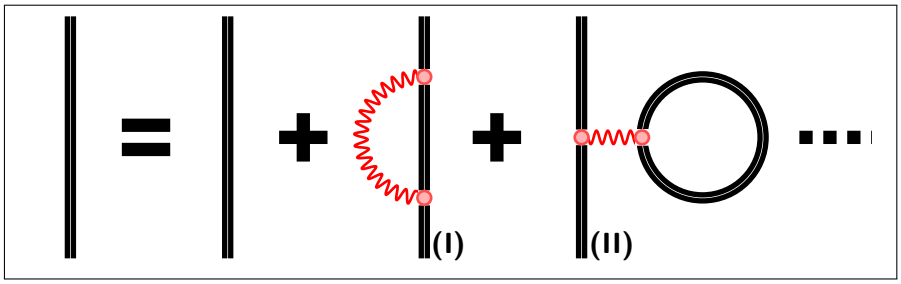

Figure 2.1: Feynman diagrams describing the propagation of an electron including self energy (I) and vacuum polarization (II) by means of a virtual photon.

energy of the electron is given by [Dem05]

$$\langle E_{\text{pot}} \rangle = -\frac{Ze^2}{4\pi\epsilon_0} \left\langle \frac{1}{r + \delta r} \right\rangle \tag{2.12}$$

The resulting shift of the energy levels is called Lamb shift.

There are still very small effects on the energy levels, which can not be explained by the previous considerations, namely the hyperfine effects. They can generally be divided into two types; those which introduce further actual splittings, called hyperfine structure (HFS) effects and those which shift the energy levels without further splitting, called isotope shifts. The former is introduced by the potentially present electromagnetic multipole moments of the nucleus. The two most important are the magnetic dipole moment and the electric quadrupole moment. The ions dealt with have one or three electrons in the ground state, are in hydrogen- or lithium-like electron configuration and therefore in a s-state over a closed shell. Since the average gradient of the electric field induced by the electron in the s-state at the nucleus is spherically symmetric, energy shifts of s-states do not have a dipole and no higher order multipole contribution. Therefore the next section deals with the HFS introduced by the magnetic dipole moment in connection with the electron spin s.

2.1.1 Hyperfine structure

The hyperfine structure splitting is due to the electromagnetic multipole moment of the nucleus and its interaction with the electromagnetic field induced at the nucleus by the electrons. For simplicity the HFS of hydrogen-like ions is explained in the following before ions with multi electron configurations are discussed.

In approximation the HFS in hydrogen-like atoms in the groundstate is only due to the dipol-dipol interaction of the magnetic moments of electron and nucleus. The magnitude of the magnetic dipole moment of the nucleus $\vec{\mu_I}$ is given by:

$$|\vec{\mu_I}| = g_I \cdot \mu_N \cdot \sqrt{I(I+1)}. \tag{2.13}$$

With the nuclear g-factor g_I, the nuclear magneton μ_N and the nuclear spin quantum number I. To describe the introduced magnetic dipole moment and the thus induced magnetic field, a perturbation term has to be added to the Hamiltonian. It can be separated into the interaction of the magnetic field with the orbital angular momentum $\vec{l}$ and with the spin of the electron $\vec{s}$.

$$\mathcal{H} = \mathcal{H}_0 + \underbrace{\mathcal{H}_{\vec{l}} + \mathcal{H}_{\vec{s}}}_{:= \mathcal{H}_{\text{pert.}}} \tag{2.14}$$

$\mathcal{H}_0$ includes already Coulomb interaction and corrections introduced by the fine structure. While $\mathcal{H}_{\vec{l}}$ can be neglected for states with $l = 0$, $\mathcal{H}_{\vec{s}}$ and thus $\mathcal{H}_{\text{pert.}}$ is given by [BHB83]

$$\mathcal{H}_{\text{pert.}} = \frac{\mu_0}{4\pi}\frac{2}{\hbar^2} g_I \mu_B \mu_N \frac{8\pi}{3}\delta(\vec{r})(\vec{s}\cdot\vec{I}), \tag{2.15}$$

the so called Fermi contact interaction with the Bohr magneton $\mu_B = \frac{e\hbar}{2m_e}$. The energy levels are than given by

$$E_{\text{HFS}}(n,l,j) = E_{n,l,j} + \frac{A}{2}[F(F+1) - j(j+1) - I(I+1)] \tag{2.16}$$

with the total angular momentum of the electron $\vec{j}$ which is $\vec{j} = \vec{s}$ for $l = 0$, the nuclear spin $\vec{I}$ and the total angular momentum of the atom $\vec{F}$ as sum of $\vec{j}$ and $\vec{I}$:

$$\vec{F} \equiv \vec{j} + \vec{I} = \vec{s} + \vec{I} \text{ (for } l = 0) \tag{2.17}$$

and the hyperfine constant A

$$A = \frac{\mu_0}{4\pi} 4 g_I \mu_B \mu_N \underbrace{\frac{1}{j(j+1)(2l+1)}}_{= \frac{4}{3} \text{ for } l=0} \frac{Z^3}{a_\mu^3 n^3} \tag{2.18}$$

containing the modified Bohr radius a_μ defined as

$$a_\mu = \frac{4\pi\epsilon_0\hbar^2}{\mu e^2}, \tag{2.19}$$

which can be written in terms of the fine structure constant α (cf. eq. 2.3)

$$a_\mu = \frac{\hbar c}{\alpha \mu}. \tag{2.20}$$

The energy difference of a electronic s-state ($l = 0$) due to the hyperfine structure effects can be written as:

$$\boxed{\Delta E_{\text{HFS}} = \alpha g_I \frac{m_e}{m_p} \frac{F(F+1) - I(I+1) - s(s+1)}{2s(s+1)} m_e c^2 \cdot \frac{(Z\alpha)^3}{n^3}} \tag{2.21}$$

The impact of the different level splittings in the atomic shell structure is schematically shown for the two lowest energy levels of the hydrogen atom in figure 2.2

2.1.2 Transition probabilities and lifetimes

The transition probability between the HFS states determines the fluorescence rate which can be expected in the experiment and needs to be known for adequate preparation. It affects which detector should be used, mainly concerning its acceptance and signal to noise ratio, and determines the needed measurement time.

To obtain an equation for the transition probability from an excited hyperfine state to the ground state $\Gamma_{F' \to F}$ the time-dependent Schrödinger equation is needed. To the time-

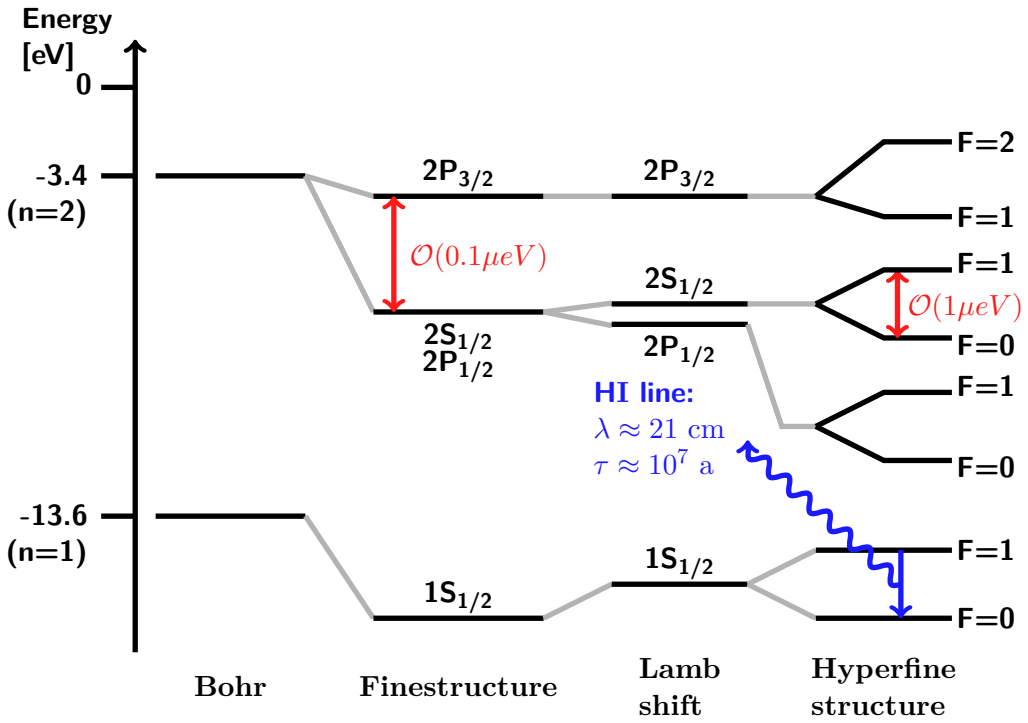

Figure 2.2: Level splittings after [Dem05] in the hydrogen atom for the two lowest levels (not to scale). With some typical values for the energy splitting and the famous hydrogen hyperfine transition line with a wavelength of about 21 cm and a lifetime of about 10^7 years. The latter provides information e.g. about the density distribution or the velocity of hydrogen atoms in the universe and is therefore important for radio astronomy and cosmology.

independent Hamiltonian $\mathcal{H}_0$ as introduced in eq. 2.1 a time-dependent Hamiltonian as perturbation $\mathcal{H}'_{\text{pert.}}(t)$ is added:

$$i\hbar\frac{\partial\Psi}{\partial t} = [\mathcal{H}_0 + \mathcal{H}'_{\text{pert.}}(t)]\Psi \tag{2.22}$$

with

$$\mathcal{H}'_{\text{pert.}}(t) = -\frac{i\hbar e}{m}\vec{A}(t)\cdot\vec{\nabla} \tag{2.23}$$

With the vector potential $\vec{A}(t)$. Equation 2.22 describes absorption as well as emission of a photon. The general solution is given by

$$\Psi = \sum_k c_k(t)\Psi_k(\vec{r})\mathrm{e}^{-iE_k t/\hbar} \tag{2.24}$$

While Ψ_k are the undisturbed eigenfunctions, $c_k(t)$ is a time dependent coefficient. For orthonormal wave-functions Ψ_k the probability to find the system in state k at a time t can be written as $|c_k(t)|^2$. The probability for a transition $\Gamma_{i\to f}$ is now given by the time derivative of the probability $|c_\mathrm{f}(t)|^2$. By applying the dipole approximation and integrating over the solid angle one obtains [BHB83]:

$$\boxed{\Gamma_{i\to f} = \frac{d}{dt}|c_\mathrm{f}(t)|^2 = \frac{4\alpha}{3c^2\hbar}\,\Delta E^3\,|\langle\Psi_\mathrm{f}|\vec{r}|\Psi_\mathrm{i}\rangle|^2} \tag{2.25}$$

With the definition $\Delta E = E_\mathrm{f} - E_\mathrm{i}$. It is worth noting that for two-level systems as discussed in the following the transition probability is the reciprocal of the lifetime and vice versa:

$$\Gamma_{i\to f} = \frac{d}{dt}|c_\mathrm{f}(t)|^2 = \frac{1}{\tau} \tag{2.26}$$

2.1.3 HFS splitting for high Z, few electron ions

For ions in hydrogen configuration the same theoretical principles as discussed so far can be applied since the quantum numbers regarding the electron are the same. For experimentalists there is a crucial difference, though. The energy splitting of hyperfine transitions depends on Z^3 as shown in eq. 2.21 and the transition wavelengths in hydrogen-like ions with $Z \gtrsim 70$ are shifted towards much shorter wavelengths into the optical region. Since the transition probability is proportional to ΔE^3 as shown in equation 2.25 the lifetime is strongly reduced as well by

$$\frac{1}{\tau} = \Gamma_{i\to f} \propto \Delta E^3 \propto (Z^3)^3 = Z^9 \Rightarrow \tau \propto Z^{-9} \tag{2.27}$$

Both aspects are in favor of laser spectroscopy. However, new corrections have to be added for high Z ions. Together with Z, the mass number A increases, and the charge radius r' defined for heavy nuclei as

$$r' \approx r_0 \cdot A^{\frac{1}{3}} \tag{2.28}$$

is larger as well. r_0 is an empirical constant with a value between 1.2 fm and 1.5 fm. At the same time with a larger Z the radius of the electron orbits r has to be reduced and is given by:

$$\langle r \rangle_{nlm} = a_\mu \frac{n^2}{Z} \left\{ 1 + \frac{1}{2} \left[1 - \frac{l(l+1)}{n^2} \right] \right\} \tag{2.29}$$

Which reads for the hydrogen ground state, i.e. $n = 1$, $l = 0$ and $m = 0$:

$$\langle r \rangle_{100} = \frac{3a_\mu}{2Z}. \tag{2.30}$$

Nucleus and electron move closer together and the nuclear structure is gaining importance. In total there are six corrections for the energy splitting in high-Z ions:

1. The motion of the nucleus is influenced by the electron's mass m_e, since the mass of the nucleus M_N is finite, resulting in a center of mass movement. The main effect of recoil is taken into account by the reduced mass. For the energy level splitting a over-all correction factor $\mathcal{M}$ has to be included [BE66] which reads in the non-relativistic approximation

$$\mathcal{M} = \left(\frac{M_N}{M_N + m_e} \right)^3 \tag{2.31}$$

   Especially for high Z this correction is very small since M_N is much larger than m_e and therefore $\frac{M_N}{M_N + m_e} \approx 1$.

2. The Coulomb interaction between electrons can be sufficiently treated non-relativistically, while for electrons seeing the almost unscreened nuclear Coulomb potential relativistic effects have to be considered, therefore the relativistic correction $A(Z\alpha)$ is introduced [PPI73]:

$$A(\alpha Z) = \frac{n^3(2l+1)\kappa(2\kappa(\gamma + n_r) - N)}{N^4\gamma(4\gamma^2 - 1)} \tag{2.32}$$

   with $\kappa = (-1)^{j+l+1/2}(j + \frac{1}{2})$, $\gamma = \sqrt{\kappa^2 - (\alpha Z)^2}$ and $N = \sqrt{n_r^2 + 2n_r\gamma + \kappa^2}$. n_r is the radial quantum number with $n = n_r + |\kappa|$.

3. Of course the assumption of a point-like nucleus is incorrect. With a spatially extended nucleus the charge distribution differs from a point-like charge. The Breit-Rosenthal effect accounts for that by amending eq. 2.21 by the factor $(1-\delta)$.

4. In analogy the Bohr-Weisskopf (BW) effect takes the spatial distribution of the nuclear magnetic moments into account via $(1-\epsilon)$.

5. QED effects like the Lamb shift, i.e. interaction of the electron with the zero-point radiation field as depicted exemplary in fig. 2.1 are summarized in a further term $\frac{\alpha}{\pi}\Delta\mathcal{E}_{\mathrm{QED}}$.

6. If more electrons are present and we have one s electron in a valence shell above a full shell, one has to account for interelectron interaction. For this reason further terms corresponding to a series expansion in the number of exchanged photons between nucleus and valence electron are added to some extend

$$\left(\frac{1}{Z}B(Z\alpha)+\frac{1}{Z^2}C(Z\alpha)+\dots\right). \tag{2.33}$$

Here $B(Z\alpha)$ is influenced by the nuclear size and the distribution of the magnetic moment and given to be

$$B(Z\alpha)=B_0(Z\alpha)(1-\delta_B)(1-\varepsilon_B), \tag{2.34}$$

as discussed in [Bei00] in more detail. $\dfrac{C(Z,Z\alpha)}{Z^2}$ can be calculated via the Breit equation as presented in [SAZ+00]. Those last two corrections are only needed for systems with more than one electron.

All extensions added to eq. 2.21 and choosing $l=0$ for an electronic s-state we obtain [VGT+08]:

$$\begin{aligned}\Delta E_{\mathrm{HFS}} =&\alpha g_I\frac{m_e}{m_p}\frac{2I+1}{(s+1)}m_ec^2\frac{(\alpha Z)^3}{n^3}\cdot\mathcal{M}\\ &\times\left\{A(\alpha Z)(1-\delta)(1-\varepsilon)+\right.\\ &\left.\frac{1}{Z}B(\alpha Z)+\frac{1}{Z^2}C(Z,\alpha Z)+\cdots+\frac{\alpha}{\pi}\mathcal{E}_{\mathrm{QED}}\right\}\end{aligned} \tag{2.35}$$

2.2 Tests of bound state QED in strong fields

Equation 2.35 would already enable bound-state QED tests, if all implied corrections are well known and the HFS energy splitting is measured. In the vicinity of the nucleus, the electric and magnetic fields exceed by far those produced artificially via pulsed lasers and superconducting magnets, respectively. Especially the $1s_{1/2}$ electron, but the $2s_{1/2}$ electron as well, is strongly influenced by those fields. Unfortunately the Bohr-Weisskopf effect (cf. point 4, p. 16) is afflicted with a high uncertainty which is comparable in size to the total contribution of QED corrections and hampers a direct test. For this reason Shabaev and co-workers have suggested a new approach by introducing the specific difference $\Delta E'$ [SAY+01], which is covered in the next section.

2.2.1 The specific difference

The uncertainty of the Bohr-Weisskopf effect was estimated to be of the order of (20-30) % [STK+97] obscuring the QED corrections. Therefore the so-called specific difference is introduced as

$$\Delta E' = \Delta E^{(2s)} - \xi \Delta E^{(1s)}. \tag{2.36}$$

$\Delta E^{(2s)}$ and $\Delta E^{(1s)}$ describe the ground state hyperfine splittings for lithium-like and hydrogen-like ions, respectively. They can be written in the following form:

$$\Delta E^{(1s)} = \Delta E^{(1s)}_{\text{Dirac}}(1 - \epsilon^{(1s)}) + \Delta E^{(1s)}_{\text{QED}} \tag{2.37}$$

$$\begin{aligned}\Delta E^{(2s)} =& \Delta E^{(2s)}_{\text{Dirac}}(1 - \epsilon^{(2s)}) + \Delta E_{\text{int}}(1 - \epsilon^{(\text{int})}) \\ &+ \Delta E^{(2s)}_{\text{QED}} + \Delta E_{\text{int-QED}}\end{aligned} \tag{2.38}$$

Here the BW contribution $\epsilon^{(is)}$ is separated from the one-electron, non-relativistic Dirac term $\Delta E^{(is)}_{\text{Dirac}}$ and the QED contribution $\Delta E^{(is)}_{\text{QED}}$ with $i = 1, 2$. While $i = 1$ stands for the 1s electron configuration in H-like, $i = 2$ represents the 2s electron configuration in Li-like ions. For the later the interelectron interaction contributes to the energy splitting via ΔE_{int}, and its corresponding BW effect ($\epsilon^{(1s)}, \epsilon^{(2s)}, \epsilon^{(\text{int})}$) is accounted by $\epsilon^{(\text{int})}$. The combined interelectron QED correction $\Delta E_{\text{int-QED}}$ can be understood as screened QED

effect.

The BW correction depends on the electronic structure only via the radial components $f(r)$ and $g(r)$ of the Dirac wave-function of the electron

$$\Psi_{nkm}(\vec{r}) = \begin{pmatrix} g_{nk}(r)\Omega_{km}(\vec{n}) \\ if_{nk}(r)\Omega_{-km}(\vec{n}) \end{pmatrix}. \tag{2.39}$$

With $f(r)$ and $g(r)$ one can define the two functions $K_S(r)$ and $K_L(r)$ [SST+98]

$$K_S(r) := \frac{\int_0^r g(r')f(r')dr'}{\int_0^\infty g(r')f(r')dr'} \tag{2.40}$$

$$K_L(r) := \frac{\int_0^r \left(1 - \frac{r'^3}{r^3}\right) g(r')f(r')dr'}{\int_0^\infty g(r')f(r')dr'} \tag{2.41}$$

which differ for the 1s and 2s states only by a small factor $f(\alpha Z)$ in the vicinity of the nucleus ($0 \leq r \leq 30$ fm) [SAY+01]:

$$\frac{K_S^{(2s)}(r)}{K_S^{(1s)}(r)} = \frac{K_L^{(2s)}(r)}{K_L^{(1s)}(r)} = f(\alpha Z). \tag{2.42}$$

The BW correction depends linearly on $K_S(r)$ and $K_L(r)$, therefore eq. 2.42 can be written in terms of the BW effect:

$$\frac{\epsilon^{(2s)}}{\epsilon^{(1s)}} = f(\alpha Z) \Leftrightarrow \epsilon^{(2s)} = f(\alpha Z)\epsilon^{(1s)}. \tag{2.43}$$

The same can be deduced for $\epsilon^{(2s)}$ and $\epsilon^{(\mathrm{int})}$

$$\frac{\epsilon^{(\mathrm{int})}}{\epsilon^{(2s)}} = f_{\mathrm{int}}(\alpha Z) \Leftrightarrow \epsilon^{(\mathrm{int})} = f_{\mathrm{int}}(\alpha Z) \underbrace{f(\alpha Z)\epsilon^{(1s)}}_{\epsilon^{(2s)}} \tag{2.44}$$

Using the two last equations the contribution of BW effect in eq. 2.37 and eq. 2.38 can be expressed using $\epsilon^{(1s)}$ only. Choosing the factor ξ in eq. 2.36 to be

$$\xi = f(\alpha Z)\frac{\Delta E^{(2s)}_{\text{Dirac}} + f_{\text{int}}(\alpha Z)\Delta E_{\text{int}}}{\Delta E^{(1s)}_{\text{Dirac}}}, \tag{2.45}$$

which is calculated for the case of bismuth to be $\xi = 0.16885$ in order to effectively cancel the influence of the BW effect on the specific difference $\Delta E'$:

$$\Delta E' = \Delta E^{(2s)} - 0.16885\Delta E^{(1s)}. \tag{2.46}$$

Now, the specific difference can be separated into a QED and a non-QED term

$$\Delta E' = \underbrace{\Delta E^{(2s)}_{\text{Dirac}} + \Delta E_{\text{int}} - \xi\Delta E^{(1s)}_{\text{Dirac}}}_{\Delta E_{\text{non-QED}}} + \underbrace{\Delta E^{(2s)}_{\text{QED}} + \Delta E_{\text{int-QED}} - \xi\Delta E^{(1s)}_{\text{QED}}}_{\Delta E_{\text{QED}}}. \tag{2.47}$$

As the non QED-term can be accurately calculated, we can then use the measured specific difference to test the predicted QED corrections.

2.2.2 *g*-factor determination

The transition probability of the hyperfine transition is directly connected to the bound g-factor of the electron. To emphasize that dependence equation 2.25 can be rewritten for the respective electron configuration. For one electron over a closed shell, e.g. in lithium-like configuration, the interelectron interactions have to be taken into account. To extract the g-factor, the transition energy needs to be known, as well as the transition probability itself. Since the latter is the reciprocal of the lifetime, it can be determined by measuring the HFS fluorescence count rate over time.

Hydrogen-like ions

For the ground state of hydrogen-like ions the transition probability can be written as follows using the Eckart-Wigner theorem [SST+98]

$$\frac{1}{\tau} = \Gamma_{F'\to F} = \frac{\alpha \Delta E_{\mathrm{HFS}}^3}{c^2} \frac{(2F'+1)(2j+1)^3}{(3j(j+1)} \cdot \begin{Bmatrix} j & F' & I \\ F & j & 1 \end{Bmatrix}^2 \cdot \left[\int_0^\infty g(r) f(r) r^3 dr \right]^2 , \tag{2.48}$$

and can be expressed as a function of the involved g-factor [Sha98] using

$$\frac{1}{\tau} = \Gamma_{F'\to F} = \frac{\alpha}{3} \frac{\Delta E_{\mathrm{HFS}}^3}{m_e^2} \frac{I}{2I+1} \left[g^{(\mathrm{e})} - g_I^{(\mathrm{n})} \frac{m_e}{m_p} \right], \tag{2.49}$$

with the nuclear g-factor given as

$$g_I^{(\mathrm{n})} = \frac{\langle IM_I | \mu_z^{(\mathrm{n})} | IM_I \rangle}{\mu_N M_I} \tag{2.50}$$

and $g^{(\mathrm{e})}$ being the sought after, bound 1s electron, g-factor. Inserting the measured HFS splitting ΔE_{HFS} and the measured lifetime, an experimental value for $g^{(\mathrm{e})}$ can be obtained.

The theoretical value has to include different corrections to the g-factor from the Dirac-equation to be comparable to the one which is experimentally determined. In [MOS+04] basically four corrections are added to the Dirac value and the g-factor amounts to:

$$g_{\mathrm{theo}} = g_{\mathrm{D}} + \Delta g_{\mathrm{QED}} + \Delta g_{\mathrm{rec}}^{(\mathrm{e})} + \Delta g_{\mathrm{NS}} \tag{2.51}$$

g_{D} is the g-factor value for an electron within a potential, i.e. a bound electron-nucleus system obtained from the Dirac equation. Δg_{QED} denotes QED corrections, $\Delta g_{\mathrm{rec}}^{(\mathrm{e})}$ corrects for the nuclear recoil and Δg_{NS} accounts for the nuclear size. These contributions are listed in tab. 2.1 respectively, after [MOS+04]. With these corrections the g-factor of the bound electron in hydrogen-like bismuth is calculated to be:

$$g_e^{\mathrm{H,theo}} = 1.731014031\ (1345). \tag{2.52}$$

Table 2.1: The individual contributions from eq. 2.51 to the bound g-factor in hydrogen-like bismuth, after [MOS+04].

g_{D}	1.727610835 (2)
Δg_{QED}	0.0028994 (9)
$\Delta g_{\mathrm{rec}}^{(\mathrm{e})}$	0.000001796 (-)
Δg_{NS}	0.000502 (1)
$g_e^{\mathrm{H,theo}}$	1.731014031 (1345)

Lithium-like ions

To account for the inter-electronic interaction equation 2.48 has to be extended. For the general case of a many-electron atom it is given after [SST+98] by

$$\frac{1}{\tau} = \Gamma_{F' \to F} = \frac{\alpha \Delta E_{\mathrm{HFS}}^3}{3c^2}(2F'+1)J(2J+1) \cdot \begin{Bmatrix} J & F' & I \\ F & J & 1 \end{Bmatrix}^2 \gamma^2(J) \tag{2.53}$$

with

$$\gamma(J) = \frac{\langle JM_J | \sum_i [\vec{r}_i \times \vec{\alpha}_i]_z | JM_J \rangle}{M_J} \tag{2.54}$$

J and M_J are the total electronic angular momentum and its projection, respectively. However, for the experimental determination of the 2s HFS in lithium-like bismuth eq. 2.49 still holds true [Sha15]. What has to be adapted is the theoretical calculation for the bound 2s electron g-factor. A term for the interelectron interaction Δg_{int} has to be added to eq. 2.51:

$$g_{\mathrm{theo}} = g_{\mathrm{D}} + \Delta g_{\mathrm{int}} + \Delta g_{\mathrm{QED}} + \Delta g_{\mathrm{rec}}^{(\mathrm{e})} + \Delta g_{\mathrm{NS}} \tag{2.55}$$

The individual contributions for Li-like bismuth are listed in tab. 2.2 respectively, after [MSQ08]. With these corrections the g-factor of the bound 2s electron in lithium-like bismuth is calculated to be [MSQ08]:

$$g_e^{\mathrm{Li,theo}} = 1.93473934\ (330). \tag{2.56}$$

Table 2.2: The individual contributions from eq. 2.55 to the bound g-factor in lithium-like bismuth, after [MSQ08].

g_{D}	1.93006882 (-)
Δg_{int}	0.002175 (3)
Δg_{QED}	0.0024077 (13)
$\Delta g_{\mathrm{rec}}^{(\mathrm{e})}$	0.0000003 (4)
Δg_{NS}	0.00008752 (17)
$g_e^{\mathrm{Li,theo}}$	1.93473934 (330)

Together with the theoretical transition wavelength, $\lambda^{\mathrm{Li,theo}} = (797.16 \pm 0.14)$ meV found by Volotka et al. [VGA+12] a more precise prediction of the lifetime can be obtained via eq. 2.49 yielding:

$$\tau^{\mathrm{Li,theo}} = (82.85 \pm 0.61)\ \mathrm{ms}. \tag{2.57}$$

Compared to the 1998 published value from Shabaev et al. [Sha98] which is given to be:

$$\tau^{\mathrm{Li,theo}} = (82.0 \pm 1.4)\ \mathrm{ms}. \tag{2.58}$$

CHAPTER 3

THE EXPERIMENTAL SET-UP

A short description of the experimental set-up is given in this chapter. The most important components and the relevant aspects for the lifetime measurements are presented. An in-depth description of the LIBELLE setup can be found in the theses of M. Lochmann [Loc13] and R. Jöhren [Jö13].

3.1 The GSI accelerator structure

The accelerator facility at the GSI is capable to provide experimentalists with ions of all known isotopes accelerated up to 90 % of the speed of light. For this purpose lowly charged ions are produced in an ion source which is in the case of bismuth a metal vapor vacuum arc ion source. After production the ions are accelerated up to 20 % of the speed of light via the universal linear accelerator (UNILAC) before they are injected into the ring accelerator SIS18. The SIS18 accelerates the highly charged ions further up to 90% of the speed of light. To produce higher charge states the ions can be send through a stripper foil where further electrons are removed from the respective ion. After selection of the desired charge state the highly charged ions (HCI) are then injected into the experimental storage ring (ESR) for the particular application.

3.2 The experimental storage ring ESR

The ESR contains six dipole and twenty multi-pole magnets spread along a beam-line with 108 m circumference to keep the stored ions on orbit and focus the ion beam in transversal direction. To improve the properties of the ion beam, concerning energy spread, divergence and spatial transversal size an electron cooler is present. Inside the cooler the ion beam is brought into overlap with the electron beam over a length of 2.5 m. The velocity of the electrons is adjusted to match average velocity of the ions and, by Coulomb interaction, the momentum spread of the ions is then reduced to $\Delta\, p/p \approx 10^{-5}$-$10^{-4}$ [NLJ+13],[UAD+15]. Via the applied acceleration potential U the device defines the velocity of the ions, β, as well:

$$\gamma = \left(1 + \frac{E_{\text{kin}}}{E_0}\right) = \left(1 + \frac{-e \cdot U}{m_e \cdot c^2}\right) \tag{3.1}$$

$$\beta = \sqrt{1 - \frac{1}{\gamma^2}} \tag{3.2}$$

e, m_e, E_0 and E_{kin} are the charge, mass, rest energy and kinetic energy of the electron. Opposite of the electron cooler another straight section with detection systems is located. The continuous ion beam can be divided into several ion bunches by changing the amplitude of radio-frequency (RF) cavities which are driven with a harmonic of the ion's revolution frequency. Zero volt amplitude leads to homogeneously distributed ions inside the ESR, the so called coasting mode; a non-zero amplitude, typically 500 V, compresses the ions in our case into two bunches.
Two entrance windows for a laser beam in the north-east and the south-east corners of the ring enable collinear and anti-collinear laser spectroscopy respectively.

3.3 The LIBELLE experiment

For the LIBELLE experiment lithium- and hydrogen-like bismuth ions were accelerated to 400 MeV/u, corresponding to a β-factor of about 0.71. During the beam time 2011 a lifetime measurement was only performed with Li-like bismuth and only in bunched mode. In 2014 lifetime data for ions with both electron configurations were taken in bunched and partly in coasting mode.

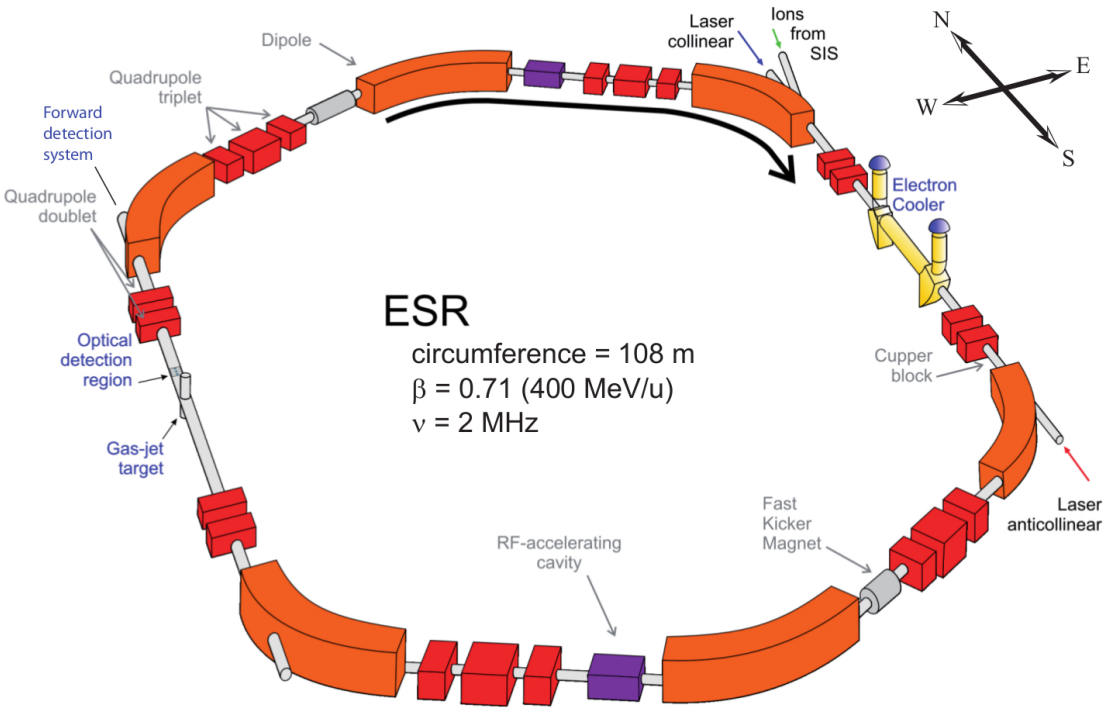

Figure 3.1: Schematic overview of the ESR with its six dipole magnets (orange), twenty multipole magnets (red) and the RF cavities in purple. The electron cooler is shown in yellow with the detection region on the opposite side labeled "Photon". The two entrance windows for the laser in the north east and south east are drawn as well. Picture taken from [San12].

The ions are excited via a laser system described in section 3.3.1 in more detail. In case of a bunched beam the RF cavities are driven with the second harmonic of the ion's revolution frequency, i.e. $\nu_{\mathrm{RF}} \approx 4$ MHz, to separate the ions into two bunches. One bunch is illuminated by the laser to be used as signal bunch, the second bunch is treated as reference. With this distinction a background correction of the data can be done. The same concept can be used for coasting beam, although no bunches are present. In that case only a part of the homogeneously distributed ions are excited, the remaining part can be used as reference. Independent whether coasting mode or bunched mode is used, a down-scaled version of the RF coming from the master oscillator applied at the cavities serves in addition as trigger for the laser as well as for the data acquisition (DAQ).
When the laser is on resonance, HFS transitions can be excited and the ions subsequently de-excite by emitting fluorescences light which has to be detected via two different detection systems for the corresponding bismuth species. Both detection systems are explained in section 3.3.2.

3.3.1 Laser system

In the rest frame the two transitions of interest have a wavelength of $\lambda_{\text{rest}}^{\text{H}} \approx 244$ nm and $\lambda_{\text{rest}}^{\text{Li}} \approx 1555$ nm, respectively. The corresponding wavelength in the laboratory frame can be calculated via eq. 3.3. The plus sign represents collinear excitation, the minus sign stands for the anti-collinear case, the ion's velocity is given by $\beta \approx 0.71$:

$$\lambda_{\text{lab}}^{\uparrow\uparrow,\uparrow\downarrow} = \lambda_0 \left(\frac{(1 \pm \beta)^2}{1 - \beta^2} \right)^{-1/2} = \lambda_0 \frac{1}{\gamma(1 \pm \beta)} \tag{3.3}$$

Since the hydrogen-like ions are excited anti-collinearly a laser wavelength of $\lambda_{\text{lab}}^{\text{H}} \approx 590$ nm is needed. The lithium-like ions are excited collinearly, therefore the required wavelength is shortened to $\lambda_{\text{lab}}^{\text{Li}} \approx 640$ nm. Both wavelengths can be provided by the same dye laser by exchanging the dye. The used laser was a SIRAH Cobra Stretch dye laser that was driven by a frequency doubled Spectra Physics Quanta Ray Pro 290-30 pulsed Nd:YAG pump laser with $\lambda = 532$ nm (cf. fig. 3.2). The incoming beam of the pump laser is split via two beam splitters into three partial beams for three amplification stages. For the first stage one part is sent directly from the first beam splitter through the active medium of the oscillator which is a cubic dye cell. For wavelength selection a diffraction grating is positioned at the end of the oscillator. In 2011 this grating was moved directly via a step motor to perform the wavelength selection (Littrow configuration, cf. fig. 3.3 (a)). In 2014 this selection was done via an additional mirror which is tiltable via a step motor, while the grating is fixed (Littman-Metcalf configuration, cf. fig. 3.3 (b)). While the line-width was about 19 GHz with the Littrow configuration it was improved with the Littman-Metcalf configuration to about 2 GHz.
After this stage the laser beam is decoupled and sent through the active medium on a higher level, where it is overlapped with the second part of the pumping beam for further amplification. The main amplification cell is a cylindric cell where the last stage takes place using the third partial beam with the major part of the pumping power.

After this amplification the dye laser emits 10 ns pulses with an energy of about 100 mJ and a repetition rate of 30 Hz.
Several optics are used to send the beam properly to the ESR entrance windows and switch between the path for collinear (cf. fig. 3.2, solid red path) and anti-collinear

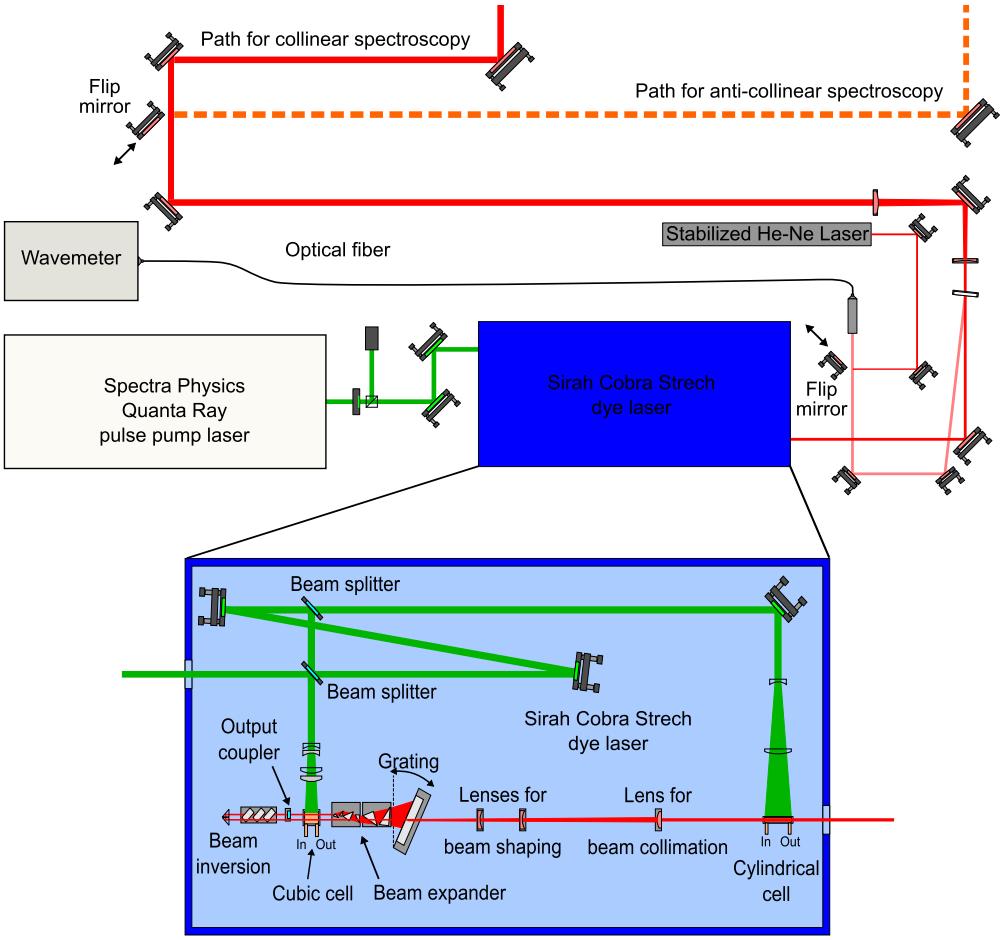

Figure 3.2: Scheme of the laser system as it was used for the LIBELLE experiment during the beam-time 2011 [San12]. The pump laser beam is split into three partial beams via two beam splitters. Two of those beams are used for pre-amplification in a cubic cell. The main amplification takes place in a cylindrical dye cell with the third part of the pump laser beam. The major difference compared to the beam-time 2014 concerns the wavelength selection via the diffraction grating, which was performed with Littrow configuration in 2011 and Littman-Metcalf configuration in 2014. The later is not shown in the scheme. Additional optics enable wavelength verification via an stabilized He-Ne-laser in combination with a wave-meter. The remaining mirrors direct the beam to the ESR via the solid red path for collinear or the dashed orange path for anti-collinear spectroscopy.

spectroscopy (cf. fig. 3.2, dashed orange path).

At each wavelength step the laser stays for several laser pulses before proceeding to the next step (cf. fig. 3.4a). To gain higher statistics the laser scans multiple times over the resonance. For a dedicated lifetime measurement the laser frequency is fixed at the wavelength with highest count rate, i.e. at resonance. As before the laser emits light with a repetition rate of 30 Hz (cf. fig. 3.4b). For $^{209}Bi^{82+}$ the time between two laser shots is long enough for the ions to decay and a lifetime measurement can be performed

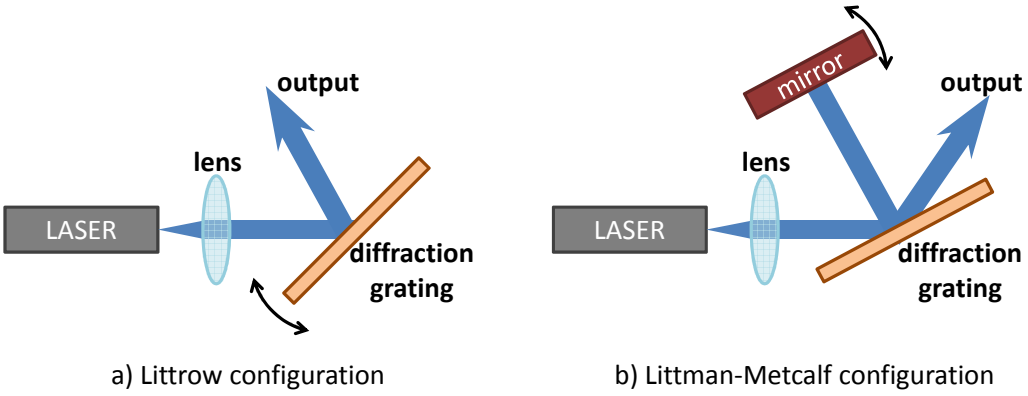

Figure 3.3: The wavelength selection is done by tilting the diffraction grating in Littrow configuration (a) and by tilting an additional mirror in Littman-Metcalf configuration (b).

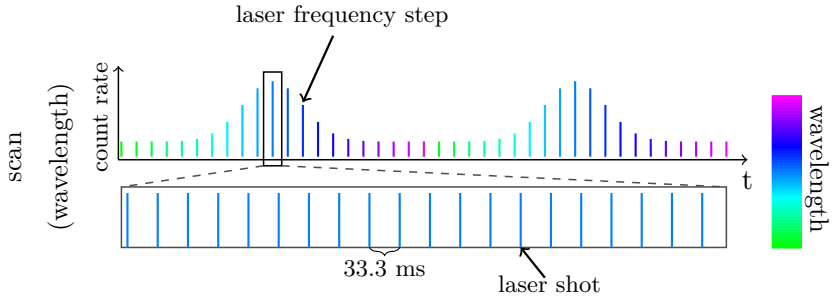

(a) In scan mode the laser frequency is varied to search for the resonance. The scanned wavelength range is about 0.4 nm wide divided in forty 0.01 nm wavelength steps. To gain higher statistics the laser is scanned repeatedly over the region of interest.

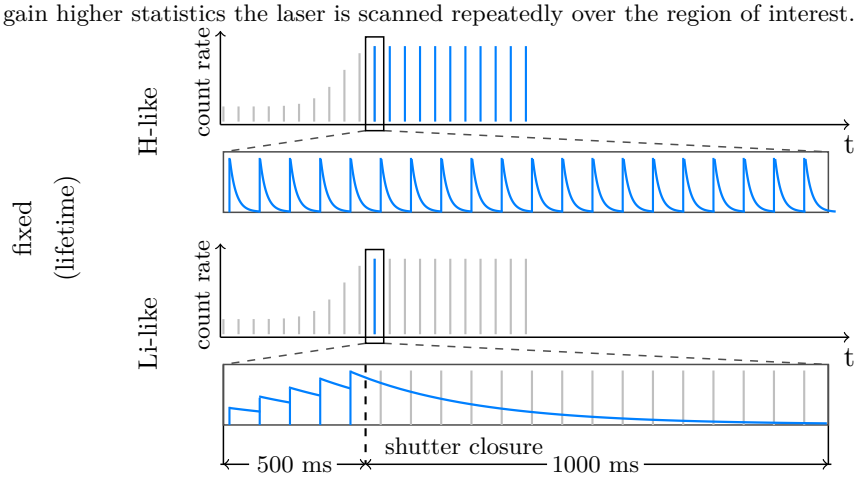

(b) For a dedicated lifetime measurement the laser frequency was set to the wavelength with highest fluorescence rate, which is at resonance. The scan was aborted and the laser was fixed at the resonance frequency. For hydrogen-like bismuth (upper part) the laser pulse scheme is unchanged and the ions can de-excite due to their short lifetime between two shots. For lithium-like bismuth (lower part) the lifetime is too long. Therefore a shutter has to be introduced which blocks the laser after about 500 ms to let the ions de-excite for about 1000 ms.

Figure 3.4: Illustration of the different measurement modes.

without any hardware changes. For $^{209}Bi^{80+}$ the interval length is not sufficient due to the long lifetime ($\mathcal{O}(\tau^{(2s)}) = 100$ ms) of the state. Therefore the laser system has to be supplemented by a shutter which is closed after several laser shots. Like this the measurement interval is extended from 33 ms to 1500 ms. The ions are excited during the first 500 ms, than the shutter closes and the excited HFS states decay over 1000 ms (cf. fig. 3.4b, bottom). To have the laser system accessible during the whole beam time for inspection and optional maintenance, the lasers were located in a laser laboratory next to the ESR cave. From this point the laser beam had to be transported over about (50-80) m through a pipe system to the ESR entrance windows as shown in fig. 3.1. During transport about half of the laser energy is lost due to the used optics and the long transport distance [Loc13]. The laser beam enters the ESR through a window at one of the dipole magnets in the north east corner for collinear, and in the south east corner for anti-collinear spectroscopy respectively. Its radius is enlarged to about 15 mm to ensure full spatial overlap with the ion beam.

Especially in bunched mode a synchronization between laser pulse and ion bunches is essential for all measurements. To guarantee the temporal overlap the RF cavities and the laser system are connected to the same 4 MHz master oscillator. The oscillator signal was discriminated, divided by a factor of two and fed into a coincidence unit together with a 30 Hz lamp trigger. For the latter a delay unit was present to adjust the phase between laser pulses and ion bunches. The output of the coincidence unit was used as trigger for the pump laser Q-switch which induced the intended light pulses of the dye laser with the appropriate timing to illuminate the signal bunch*.

3.3.2 Detection systems

The basic reason for performing this laser spectroscopy experiment at a storage ring is the Doppler shift of the transition wavelength. The Doppler shift enables the excitation of both electron configurations with the same laser (cf. eq. 3.3) and in addition the photon detection is more efficient due to a higher quantum efficiency (QE) of the photomultiplier in this wavelength region. The Doppler shifted wavelength of the emitted fluorescence

*Or a corresponding part of the homogeneous distributed ions in coasting mode.

photons is dependent on the emission angle Θ, relative to the beam direction and is given by:

$$\lambda = \lambda_0 \cdot \gamma(1 - \beta \cos \Theta) \tag{3.4}$$

One drawback is the event rate in $^{209}Bi^{80+}$, though. Since the lifetime is quite long ($\sim$ 82 ms) only a low signal rate is expected. Due to the relativistic velocity of the ions the lifetime is dilated ($\sim$ 116 ms) and the signal rate is even lower. In addition, the collection of fluorescence photons, that are emitted randomly along the circumference of the storage ring is much less efficient.

Mirror section

The straight mirror section was introduced 1993 and modified 1999 to its present state by P. Seelig ([See99]) and now contains eleven cylindrical segments on top and eleven elliptic mirror segments below the ion beam which are tilted by 15°. In the upper part three cutouts for view-ports are present where photomultiplier tubes can be mounted. With this geometry the system is most efficient to detect photons with emission angles

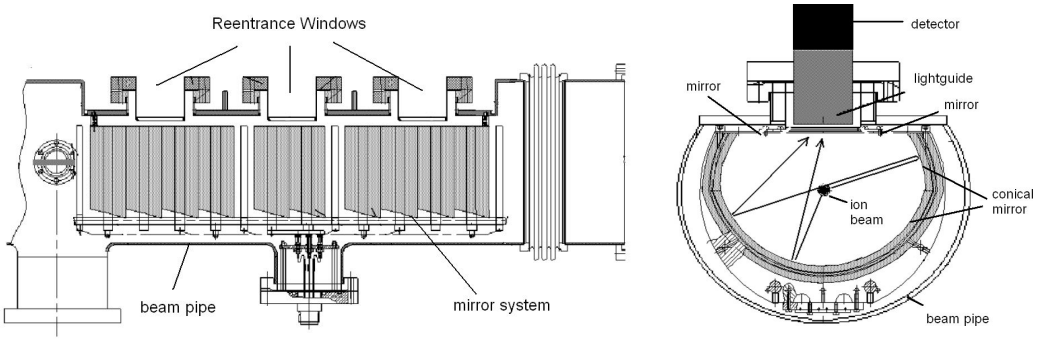

Figure 3.5: Technical drawing of the segmented mirror section, perpendicular to the ion beam direction (left) and parallel to the ion beam direction (right). The 65 cm long section contains ten mirror segments, each with a length of 5.5 cm and an opening angle of 15°. Two exemplary photon tracks towards the detector are shown in the right drawing. [See99]

$20° \leq \theta \leq 60°$. A detailed description of this mirror system can be found in the originally work of P. Seelig ([See99]) and in the work of R. Jöhren ([Jö13]) and M. Lochmann ([Loc13]) with special focus on the LIBELLE experiment.

With the segmented mirror section various experiments were performed successfully, like [Kla94],[Win99]. The LIBELLE experiment used the segmented mirror section

successfully as well to investigate the HFS transition in hydrogen-like bismuth. The detection of the HFS transition in lithium-like bismuth remained unsuccessful with this system, though [Win99, Nö11].

The reasons why the segmented mirror section is apparently not suitable to detect the HFS transition in $^{209}Bi^{80+}$was investigated in the diploma thesis of D. Anielski ([Ani10]). A crucial parameter for photon detection is the emission angle distribution which is isotropic in the co-moving frame but is deformed by the Lorentz boost in the laboratory frame. By the boost the solid angle is reduced and the emission of photons in forward direction is enhanced. Those photons with emission angles $\theta \leq 20°$ are Doppler shifted far enough into a wavelength region for which the PMTs have a high quantum efficiency (QE). Unfortunately the mirror section is not efficient in collecting those forward emitted photons, as mentioned before. For this reason a novel detection system was introduced as described in the next paragraph.

Movable mirror system

As it was shown in [Ani10] a detection system was needed capable to detect primarily forward emitted photons. For this purpose a movable parabolic, oxygen free, high conductive copper (OFHC) mirror with a central slit of about 3 cm corresponding to 3σ of the expected ion beam diameter was designed. As detector a highly selected low

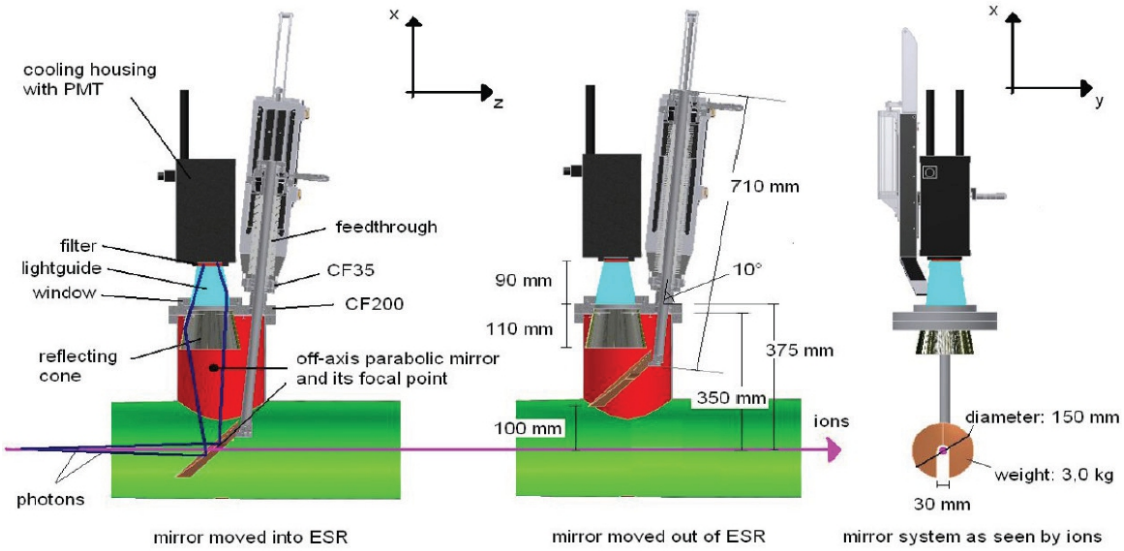

Figure 3.6: Schematic overview of the movable mirror system. The first two figures show the mirror system from above the ESR, the third from the perspective of the ions [Ani10].

Table 3.1: Comparison between the two detection systems regarding signal and background rate and the needed measurement time per wavelength to detect the signal with 3σ significance [HAG+13].

	signal rate $[s^{-1}]$	background rate $[s^{-1}]$	measurement time [s]
Segmented mirror section	15.4 ± 0.5	626 ± 7	47.6 ± 0.9
Parabolic mirror	86.0 ± 0.6	453 ± 9	1.1 ± 0.01

noise R1017 Hamamatsu photomultiplier was used. During injection of the ions in the ESR and beam preparation, i.e. beam cooling and bunching, the mirror can moved out of the beam line to prevent interaction of the uncooled ion beam with the mirror. The mirror can then be moved in to collect photons which are emitted under small angles up to about 25°. Like this forward emitted photons are collected with high efficiency. In addition those photons are most efficiently detected by the PMTs since they experience the largest Doppler shift. A comparison of the performance of the two different detection systems obtained by simulations is given in table 3.1. For further details about the parabolic mirror system please see [HAG+13].

3.3.3 Data acquisition (DAQ)

The center piece of the data acquisition was a customizable, GSI made VME based board called VUPROM in combination with a CPU to collect and organize the data. The VUPROM provides 16 scaler channels and 16 channels which were operated as multi-hit double-buffer time-to-digital-converters, short TDCs. The CPU had to read out and reset each channel, organize all accumulated data in an event structure and write it to the GSI tape storage system called Gstore.

Start and stop signal for the TDC channels are given by the detector signals and the down-scaled frequency of the master oscillator of the ESR, respectively. The TDC channel content represents the number of clock cycles before the common stop with a clock frequency of 300 MHz resulting in a 3.33 ns time resolution for the TDC channels.

The detectors read with the TDCs are four PMTs - three are of type 9422A located at the mirror section and intended for the transition in hydrogen-like Bismuth (TDC ch. 1-3) and the fourth is the R1017 PMT of the parabolic mirror system for the detection of the transition in lithium-like bismuth (TDC ch. 0). All PMT signals were amplified by a factor of 100 via two stages of a CAEN Mod. 979 16 channel fast amplifier. The

amplification is done close to the PMTs still inside the ESR cave before the signals were sent to the measurement cabin. There they were inductively decoupled and afterwards discriminated by a CAEN Mod. N843 16 channel constant fraction discriminator. The resulting logic signals were fed into the respective channels of the VUPROM. A detailed scheme of the cabling is presented in appendix A.1.

3.4 Beam time 2011

While the HFS transition in hydrogen-like bismuth was already measured before in laser spectroscopy experiments, for example by Winter and co-workers [Win99], the search after the transition in lithium-like bismuth was, for a long time, unsuccessful. Therefore the major task of the LIBELLE beam-time in 2011 was the detection of this transition. As a consequence a lifetime measurement of the upper HFS state was performed only within the last few hours of the beam-time and only for $^{209}Bi^{80+}$.
The CPU used for event readout and data organization then was a Motorola 68040, VME-based computer board running the GSI Multi Branch System (MBS) software. To reduce the data stream the 4 MHz of the master oscillator was reduced by a factor of 200 before being used as common stop signal. The data volume is enlarged during a lifetime measurement, since absolute time-stamps have to be stored for each photon in addition. The Motorola CPU was not able to handle such amount of data, therefore the frequency of the master oscillator was divided by a factor of 400 instead of 200 for the lifetime measurement.

With completion of the beam-time and start of the analysis it turned out, that the overall result of the transition wavelength was burdened with a high uncertainty. This uncertainty arose by the transformation of the wavelength to the laboratory frame, because the velocity of the ions was not determined as accurately as expected. The reason was the applied voltage of the electron cooler, which defines the velocity of the ions and was not known well enough [Jö13, Loc13].
For this reason a second beam-time was scheduled for March 2014, with a much improved determination of the ion velocities and an updated DAQ system.

3.5 Beam time 2014

The major improvement for the second beam time was the possibility to measure the high voltage applied at the electron cooler in-situ. This was achieved by the introduction of a high precision voltage divider provided by the Physikalisch-Technische Bundesanstalt Braunschweig (PTB). The divider can handle voltages up to a maximum of 250 kV. With this device the uncertainty was improved to the $< 10^{-4}$ level.

Another improvement which was important for the lifetime measurement was the upgrade of the data acquisition CPU. The old Motorola 68040 was exchanged by an new RIO4 real-time computer. The RIO4 CPU was capable of handling large data streams and timestamps could be recorded during the whole beam-time without reducing the readout frequency. Therefore the frequency of the master oscillator was divided by 200 for the common-stop during the whole beam-time. Since timestamps were stored continually, a part of the available data recorded during a scan over the resonance can also be used for lifetime analysis. This is especially true for $^{209}Bi^{82+}$, since no further modifications are needed, concerning the measurement interval. For $^{209}Bi^{80+}$all data is equipped with the needed time information as well, but the lifetime to be measured is much longer. Therefore the measurement interval has to be extended by the introduction of a shutter. Otherwise only the first 33 ms of the decay curve with a laboratory lifetime of ≈116 ms can be extracted from the recorded data, as already discussed in sec. 3.3.1.

3.5.1 DAQ load test

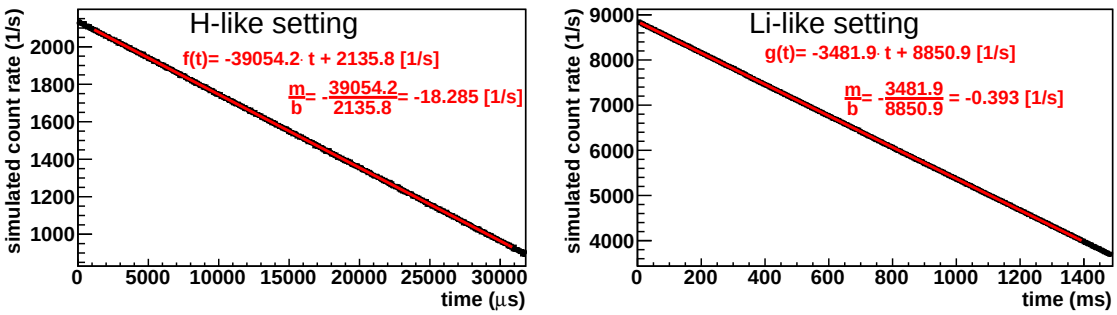

Figure 3.7: A load test was performed with the new DAQ to ensure its proper functioning. If no events are missed and the data is recorded without creating artifacts the ratio $\frac{m}{b}$ should be the same for the input values and the recorded output data.

The new DAQ has to be able to record much more data since a time-stamp has to be stored for each detected photon. Therefore it was tested by using a Tektronix arbitrary function generator (AFG) to simulate photon events. For this purpose the AFG provided a NIM signal with a certain frequency which was fed into the DAQ instead of the discriminated PMT signals. To test the behavior of the hardware for the case that many photons reach the detector a frequency roughly in the order of the expected photon count rate was used as start condition. Furthermore the absence of artifacts during the decline of the photon count rate was ensured. For that purpose the decrease of photon count rate due to the lifetime of the excited state was resembled vaguely and were programmed for the two different bismuth species as rate drops within the AFG. In both cases a linear decline from a start frequency of 2267.8 Hz to 941.51 Hz was used, which represents a decreasing photon count rate. For H-like bismuth this span was processed within a time comparable to the measurement interval of 33 ms which is given by the laser shot frequency of 30 Hz. In case of Li-like bismuth the span was processed within an appropriate time corresponding to the measurement interval of 1.5 s which was created by the introduced shutter. Those settings lead to a signal linearly decreasing in frequency described by the two following equations, $f(t)$ for the hydrogen-like settings and $g(t)$ for the lithium-like settings:

$$f(t) = \underbrace{\frac{\nu_{\text{end}} - \nu_{\text{start}}}{t_{\text{end}} - t_{\text{start}}}}_{:=m} \cdot t + \underbrace{\nu_{\text{start}}}_{:=b} = \frac{941.51 - 2267.8}{0.0032 - 0} \cdot t + 2267.8 \tag{3.5}$$

$$= -41446.56 \cdot t + 2267.8 \text{ [1/s]}$$

$$\Rightarrow \frac{m}{b} = -\frac{41446.56}{2267.8} \approx -18.28 \text{ [1/s]} \tag{3.6}$$

$$g(t) = \underbrace{\frac{\nu_{\text{end}} - \nu_{\text{start}}}{t'_{\text{end}} - t_{\text{start}}}}_{:=m'} \cdot t + \underbrace{\nu_{\text{start}}}_{:=b} = \frac{941.51 - 2267.8}{1.49 - 0} \cdot t + 2267.8 \tag{3.7}$$

$$= -890.13 \cdot t + 2267.8 \text{ [1/s]}$$

$$\Rightarrow \frac{m'}{b} = -\frac{890.13}{2267.8} \approx -0.393 \text{ [1/s]} \tag{3.8}$$

The corresponding data as recorded by the DAQ is shown in fig. 3.7 together with a linear fit function. The obtained ratio $\frac{m}{b}$ from the fit is identical to that previously calculated for both measurement settings. It was therefore shown, that the new DAQ can handle the much larger data stream adequately.

CHAPTER 4

LIFETIME ANALYSIS

In this chapter the main focus is on the lifetime analysis of data taken for both bismuth species in the different measurement modes. Systematic effects as also considered in [Win99],[Kla94], are discussed and compared to the experimental data.

4.1 Basic data structure

The DAQ records a time-stamp via a multi-hit time to digital converter (TDC) for each detected photon (TDC channels 0-3) and for the laser trigger (TDC ch. 15) with 3.33 ns time resolution (corresponding to 300 MHz clock frequency of the TDC). The stored value is the time between the event (e.g. laser shot, photon detection) and a common stop signal which is provided by the ESR high-frequency master oscillator as described in chapter 3. In case of the Li-like lifetime measurements a time-stamp for the shutter closure was stored in the same way during the beam-time 2014 (TDC ch. 12). In 2011 this reference point was stored via a scaler (scaler ch. 31) filled with an 1 MHz signal. Data were recorded at each common stop which occurs every 50 μs. For the analysis the scaler corresponding to the ion current (scaler ch. 16), the electron cooler voltage (ch. 18), the divided RF (ch. 22), the laser status (ch. 27) and a 1 MHz clock (ch. 23) are of importance. The current laser wavelength was measured by a separate PC connected to an ATOS LM-007 lambda-meter which was read out via a LabView control program.

Data from the LabView control were transfered to the RIO4 CPU responsible for the event readout and integrated into the data stream.

4.1.1 Ion current

The actual value for the ion current in mA can be calculated from the corresponding scalers N_i as follows:

$$I_{\mathrm{IC}} = \left(N_{\mathrm{IC}} \cdot \frac{1 \cdot 10^6}{N_{\mathrm{clock}}} - 2059.3 \right) \cdot 10^{-5}\ \mathrm{mA}. \tag{4.1}$$

N_{IC} contains information connected to the ion current itself and N_{clock} is a continuous 1 MHz clock. The ion current of each dataset used in the analysis was checked regarding the proper time dependence (compare fig. 4.1, upper plot). An exponential decay is expected because of losses due to interactions of the ions with the environment, like electron capture in the cooler or collisions with residual gas inside the ESR. Data exhibiting abnormal structures in the current are discarded (see fig. 4.1, lower plot). The time dependent ion current can be fitted with

$$g(t) = I_0 \cdot \exp\left\{ -t/\tau_{\mathrm{HCI}} \right\}$$

with I_0 being the amount of injected ions in mA after eq. 4.1 and τ_{HCI} the lifetime of the ion beam. The beam has an average lifetime $\tau_{\mathrm{HCI}} \approx 30$ minutes which is much larger than the studied lifetimes of the HFS states. Therefore the ion current can safely be assumed to be constant over the short time intervals (≤ 1.5 s) used in the lifetime fits. A possible influence of the ion current on the lifetime, e.g. due to de-excitation in ion-ion collisions, is discussed in section 4.4.5.

4.1.2 Accumulation of signal and reference data

For data stacking the revolution time $t_{\mathrm{rev.}}$ of the ions needs to be known. Therefore the revolution frequency of the ions was measured regularly via a Schottky pick-up in bunched beam mode to compensate deviations in the velocity of the ions due to fluctuations of the electron cooler voltage. The value obtained in this way is used for the analysis.

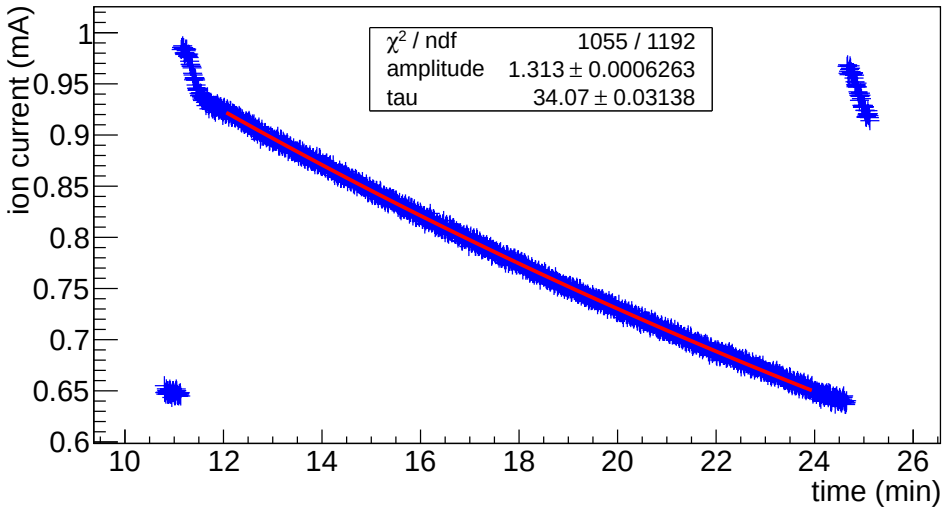

(a) Normal ion current behavior with a lifetime of about 30 min. Ion injection occurs around minute 11 and 24.5. The rapid decrease shortly after the injection is due to beam cooling.

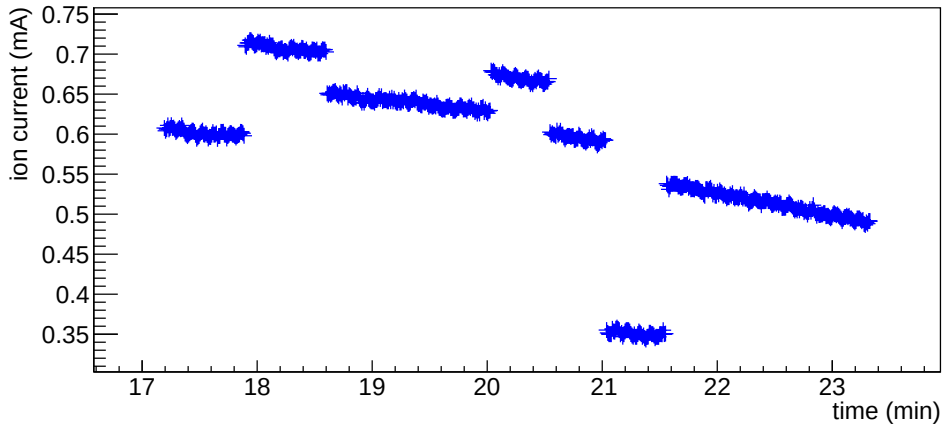

(b) Datasets with pathological ion current are rejected in the analysis.

Figure 4.1: Ion current as function of time for different datasets. The ion current can be fitted with an exponential yielding the mean storage time of the ions in the ESR. For the data analysis only sets with regular behavior of the current as shown in fig. (a) are used. In such sets time intervals shortly before and after injection are cut away as well as regions affected by beam cooling.

Since the time resolution of the TDCs is 3.33 ns the corresponding histograms are chosen to have the same bin-width such that the number of bins per revolution, the so called cycle time bins, is given by:

$$\frac{t_{\text{rev.}}}{3.33\ \text{ns/bin}} \approx 153\ \text{bins} \tag{4.2}$$

Each PMT signal has a time-stamp corresponding to its detection time relative to the common stop. By sorting the signals into one of the 153 bins depending on their TDC-time-stamp modulo the number of cycle time bins, one obtains a stacked histogram as shown in fig. 4.2. The histogram depicts the bunch structure of the stored ions, since the

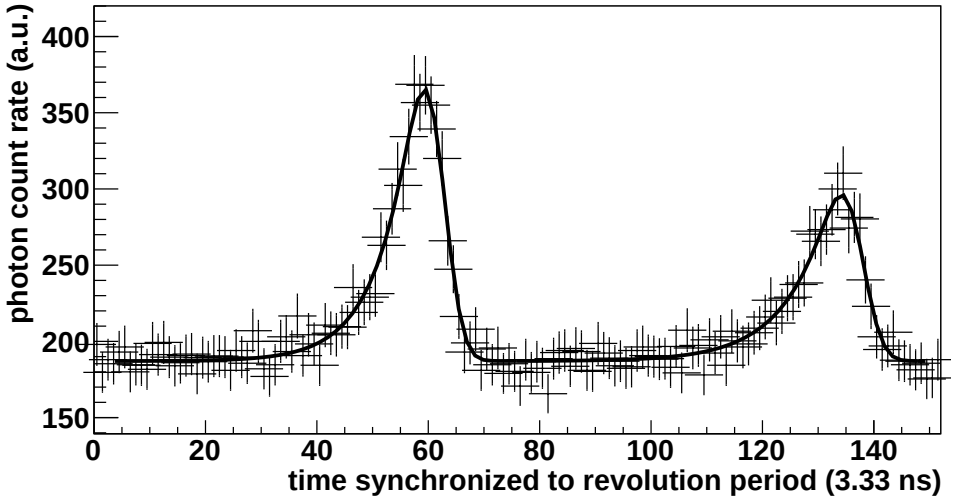

Figure 4.2: Example of a stacked histogram filled with TDC-timestamps modulo the ion revolution time together with a fit model described by eq. 4.4. The bin width matches the TDC time resolution of 3.33 ns, the total range represents one circulation of the ions in the ESR.

common stop signal is connected to the master oscillator of the ESR which drives the bunching cavities.

In such a histogram a signal, as well as a reference peak can be identified on top of a homogeneous background. The signal region contains events from the ion bunch that is excited by the laser beam (left peak in fig. 4.2), while the reference region contains background signals caused by the ion bunch not in overlap with the laser (right peak in fig. 4.2). The overall background $D(I_{\mathrm{IC}})$ is composed of four parts [HAG+13]:

$$D_{\mathrm{IC}} = D_{\mathrm{PMT}} + D_{\mathrm{ll}} + D_{\mathrm{rg}}(I_{\mathrm{IC}}) + D_{\mathrm{h}}(I_{\mathrm{IC}}) \tag{4.3}$$

D_{PMT} is given by the dark count rate of the photo-multipliers, D_{ll} accounts for photons from light leaks in the ESR, $D_{\mathrm{rg}}(I_{\mathrm{IC}})$ is the contribution of photons from residual gas excitation by the ion beam I_{IC} and $D_{\mathrm{h}}(I_{\mathrm{IC}})$ are photons produced if the ions from the beam halo hit the movable mirror. While the homogeneous background is due to the terms independent of the ion beam ($D_{\mathrm{PMT}},\ D_{\mathrm{ll}}$), leading to an offset, the reference peak is due to the terms which are dependent on the ion beam ($D_{\mathrm{rg}}(I_{\mathrm{IC}})$, $D_{\mathrm{h}}(I_{\mathrm{IC}})$). Of course

the ion current dependent terms contribute to the signal peak as well. Therefore two nearly identical peaks are expected after all excited ions are decayed.

The identification of signal and reference region is independent of the operating mode of the ESR, namely homogeneous distributed ions in coasting mode or compressed ion packets in bunched mode. For the coasting beam case, which was only used successfully for H-like bismuth ions, an example is shown in fig. 4.3. Since the free revolution frequency cannot be measured in bunched mode via a Schottky pick-up, it has to be determined regularly in coasting mode. Fig. 4.3 contains in the left half signals from those ions that are in overlap with the laser pulses, while the rest of the ions cause a homogeneous background distribution. The presence of signal and background regions

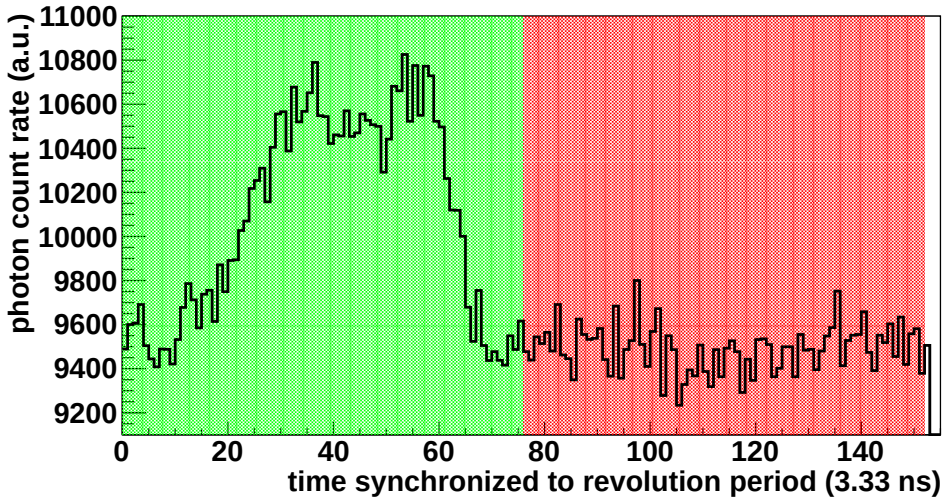

Figure 4.3: Data with coasting ion beam. One can identify a signal region (left/green) and a background region (right/red). In this case the histogram was cut in half to define the background and signal regions.

enables background correction as discussed in the next sections.

4.2 Extraction of lifetime curves

To extract the lifetime of the HFS states from the data, the fluorescence photon count rate versus time needs to be investigated. For this purpose a time-stamp as reference point is needed, hereinafter called reference-time-stamp. For H-like data it is given by the laser shot itself, for Li-like data the time of shutter closure is used. After subtraction of the reference-time-stamp, the arrival times of the observed events are then accumulated in timing bins with a width of 25 μs for the H-like case and 5 ms for Li-like ions. Two

alternative methods are used to further process the data. Firstly the fit-method where for each timing bin the peak shapes of the resulting stacked histograms (as shown in Fig. 4.2) are fitted with an appropriate model and the difference of signal and reference peak is obtained from the fit. Secondly the bin-method, where events within a chosen window around the centers of the signal and reference peak are summed up and used directly.

4.2.1 Fit method

For data taken in bunched mode a number of stacked histograms like shown in fig. 4.2 are created, each comprising data from a fixed time interval after the reference point. The two peaks in the individual histograms are fitted using two Gaussians, each convoluted with an exponential decay (so-called exponentially modified Gaussians, short EMG) on top of a constant background, using the following function

$$\begin{aligned} f(t) = \quad & \frac{A}{2\cdot\lambda_1}\cdot\exp\left\{\frac{\sigma_1^2}{2\cdot\lambda_1^2}+\frac{t_0-t}{\lambda_1}\right\}\cdot\left(\operatorname{erf}\left\{\frac{t-t_0}{\sqrt{2}\cdot\sigma_1}-\frac{\sigma_1}{\sqrt{2}\cdot\lambda_1}\right\}+\frac{\lambda_1}{|\lambda_1|}\right) \\ + \quad & \frac{A+\Delta A}{2\cdot\lambda_2}\cdot\exp\left\{\frac{\sigma_2^2}{2\cdot\lambda_2^2}+\frac{t_0'-t}{\lambda_2}\right\}\cdot\left(\operatorname{erf}\left\{\frac{t-t_0'}{\sqrt{2}\cdot\sigma_2}-\frac{\sigma_2}{\sqrt{2}\cdot\lambda_2}\right\}+\frac{\lambda_2}{|\lambda_2|}\right) \\ + \quad & c_1\ . \end{aligned} \tag{4.4}$$

The exponential tails of the EMGs describe background from residual gas atoms which are excited via collisions with the highly charged ions and produce an afterglow. The fit model is parameterized in a way that the parameter ΔA is directly the difference between the areas of the signal and background peaks. By plotting the ΔA values obtained for each timing bin against the central time value of that bin, one obtains a background corrected lifetime curve of the HFS state under consideration. Figure 4.4 displays an example of a lifetime curve obtained using the fit-method from a subset of the data taken for Li-like Bismuth in the 2014 beam-time. The plot starts with the shutter closure after which an exponential decay of the excited ions is observed. After 1 s the shutter is opened again and the upper HFS state is repopulated by laser excitation. The first part of the curve is fitted with an exponential decay model

$$f(t) = N_0\cdot\exp\left\{-\frac{t}{\tau}\right\}+c_2 \tag{4.5}$$

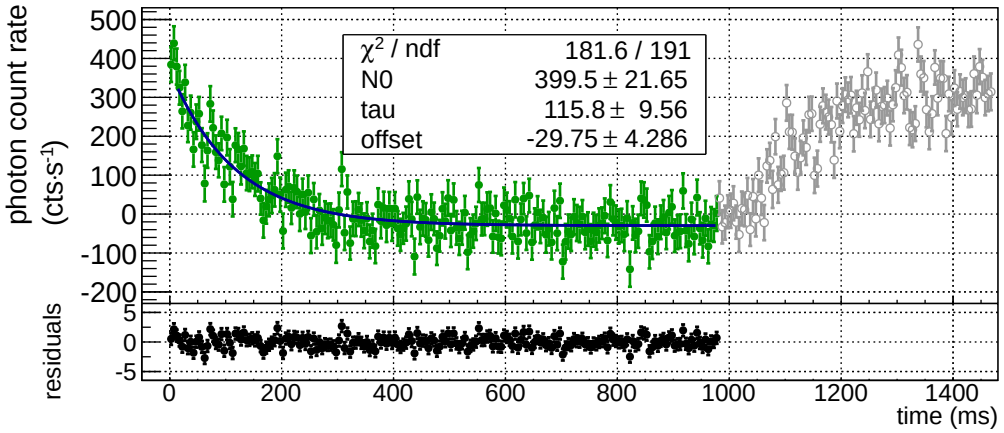

Figure 4.4: Lifetime curve obtained using the fit-method from a subset of the data taken for Li-like Bismuth in the 2014 beam-time.

where N_0 is the number of initially excited ions, τ the desired lifetime and c_2 a constant offset. While the main features of the curve are as expected, we observe a significant negative offset that should be zero if the background subtraction works as expected. The origin of this offset is discussed in section 4.2.4.

4.2.2 Bin method

While the fit-method takes the complete peak shape of the signal or reference bunches into account which, especially in the tail regions, is not always perfectly described by the EMG model, a second, simpler method has been developed that tries to improve the signal to noise ratio by discarding those parts of the peaks that are dominated by background. If we compare histograms of the bunch structure right after laser excitation of the ions (fig. 4.5, left, blue curve) to histograms compiled from data taken after several half-lives (fig. 4.5, left, red curve), we can determine which bins of the histograms contain the actual fluorescence signal of the HFS-state under consideration. Fig. 4.5, right hand side, displays the difference of the blue and red distributions, with a clear signal peak emerging around bin 60. By summing up all counts within a $\pm n\sigma$ window around the peak center and plotting the result against the central value of the timing bin, from which the histograms have been extracted, one again obtains a lifetime curve of the transition (see fig. 4.6, upper plot). Initially a window of $\pm n\sigma = \pm 2\sigma$ was chosen for the analysis. To optimize the window width for the final lifetime value a systematic variation of the window width was done and is presented later.

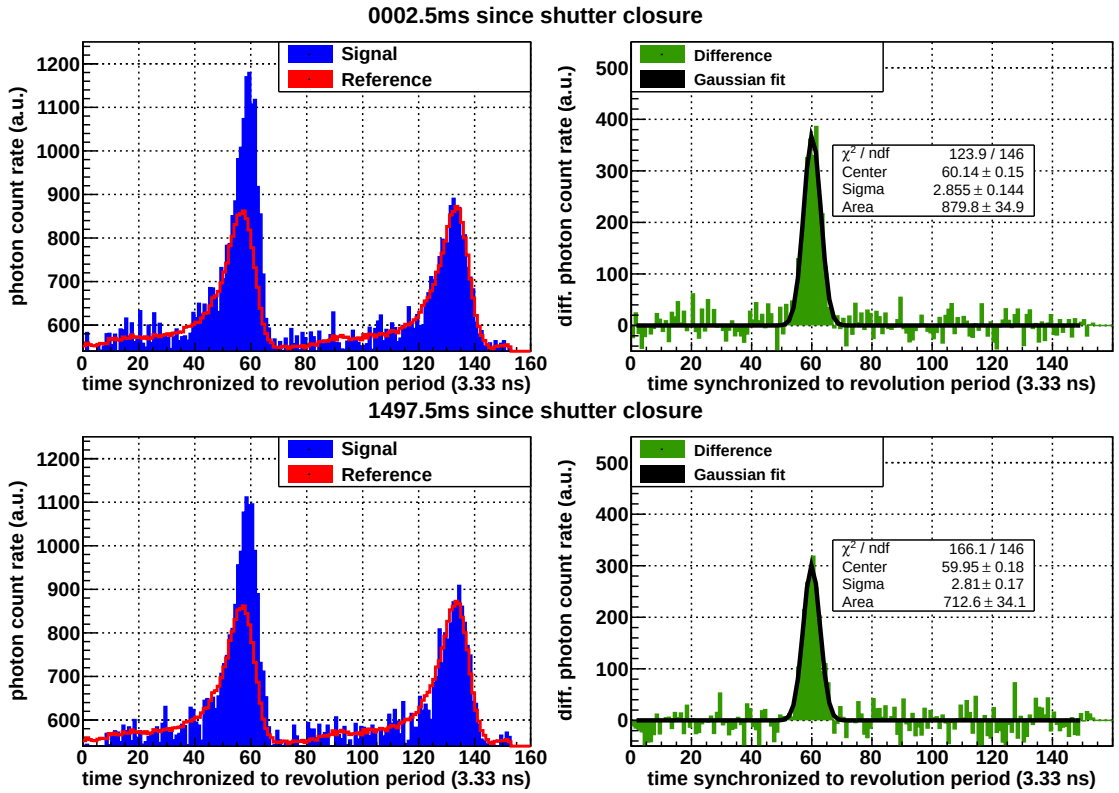

Figure 4.5: Left, blue histogram: signal and reference bunch at 2.5 ms (top) and at 1497.5 ms (bottom) after shutter closure. The red curve in the two plots corresponds to the situation at the end of the decay interval at about 800 ms. Right: difference of the two histograms shown on the left, fitted with a Gaussian function.

If the summed counts from a window of equal width around the reference peaks are subtracted for each data-point, one again obtains a background corrected version of the lifetime curve (see fig. 4.6, lower plot). As observed with the fit-method, we find an unexpected negative offset of the lifetime curve in the background corrected version that will be discussed in section 4.2.4.

When looking at figure 4.6 one finds that the background correction by subtraction of counts from the reference peak is actually counter-productive when trying to reduce the statistical uncertainty of the extracted lifetime value. This is because in order to eliminate the background we have to subtract two large quantities with statistical uncertainties given by $\sqrt{N}$ and similar magnitude. The resulting error bar on the difference is $\Delta N_{\text{diff}} = \sqrt{N_s + N_r}$, while the uncertainty on the number of counts in the signal region alone is $\Delta N_s = \sqrt{N_s}$. The background subtraction therefore only makes sense, if we observe distortions or non-statistical fluctuations in the lifetime curve, that need to be corrected

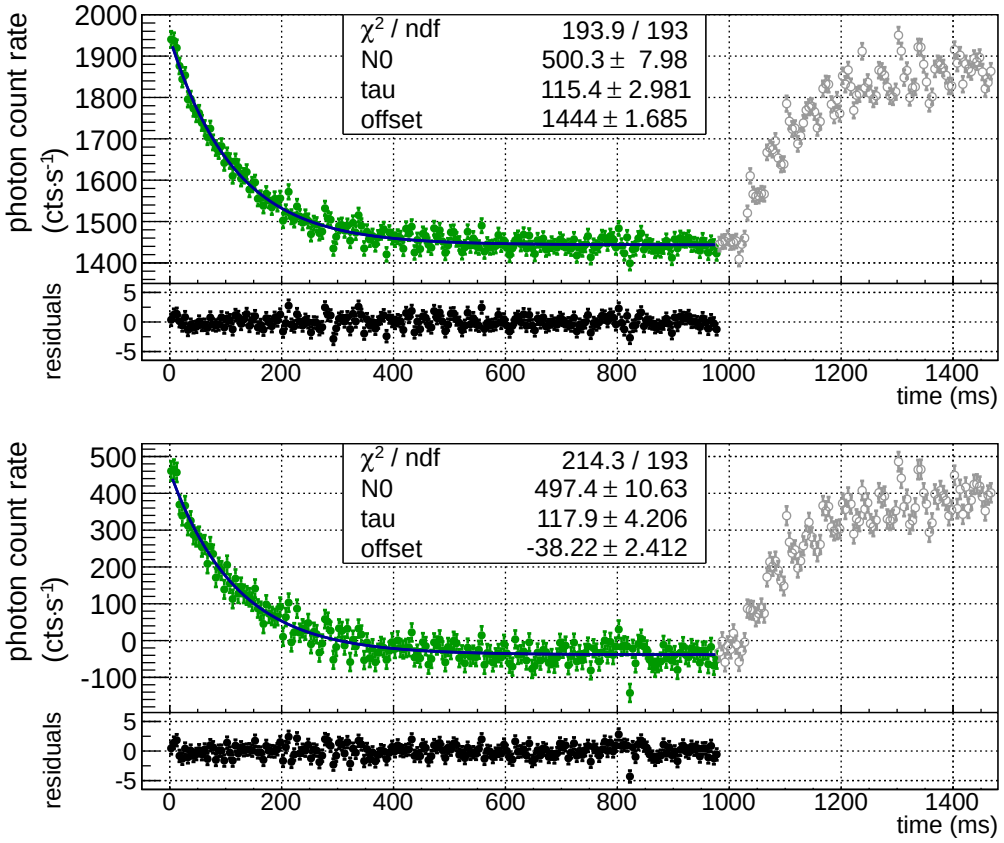

Figure 4.6: Upper plot: $^{209}Bi^{80+}$lifetime plot with uncorrected signal, $\chi^2_{\text{red.}} = 1.00 \pm 0.10$. Lower plot: Difference between signal and reference data leading to a background corrected lifetime curve, $\chi^2_{\text{red.}} = 1.11 \pm 0.10$. In both cases the signal peak emerges at bin 56 and the reference peak at bin 132 and a window of $\pm 2\sigma$, i.e. 8 bins width, was used around those positions.

for. As both lifetime curves displayed in figure 4.6 are well described by the model fit with reduced χ^2-values close to one and consistent lifetime results, we can actually omit the background subtraction in the further analysis of the data.

4.2.3 Comparison of both methods

When comparing figure 4.4 and figure 4.6, it is found that the uncorrected bin-method actually provides smaller error bars and a clearer signature of the individual laser pulses in the excitation phase of the lifetime curve for $^{209}Bi^{80+}$than the background corrected version of the bin-method or the fit-method. Furthermore the background correction in both cases does not work as intended and leads to an unexpected negative background in the lifetime curve. Therefore the uncorrected bin-method will be used for the lifetime analysis of the two LIBELLE beam-times described in sections 4.3 and 4.4.

4.2.4 Offset of lifetime curves for the Li-like HFS state

In the background corrected decay curves for $^{209}Bi^{80+}$a significant negative offset has been observed both with the fit-method and with the bin-method. Such an offset should not be present if the two ion bunches stored in the ESR contain on average the same number of ions. After all excited states in the signal bunch have decayed the remaining signal in the PMTs is only due to ion interactions with the environment. This should be the same for signal and reference bunch leading to a vanishing difference.

After thoroughly checking the analysis code and a large number of tests on the acquired data, it was concluded that there is a physical effect that causes the signal bunch to loose ions faster over time than the reference bunch. This effect can be seen when plotting the offset of the lifetime curve as a function of time after the injection of the ions into the storage ring. Figure 4.7 displays offsets determined from two minute intervals after injection. Despite relatively large uncertainties, a clear trend towards significantly

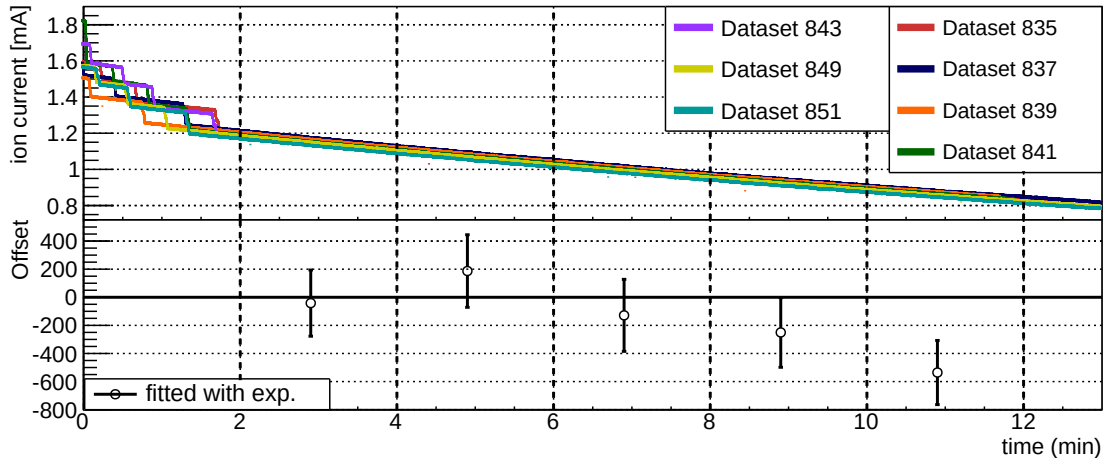

Figure 4.7: Offset of the lifetime curve versus time since last ion injection into the ESR. On the upper plot the ion current as function of time is shown for seven different datasets. Separated into five time windows, i.e. 2-4 minutes, 4-6 min., 6-8 min., 8-10 min. and 10-12 min. since injection. For those five segments a lifetime curve is extracted. To obtain the offset of the curve it is fitted with an exponential fit function (eq. 4.5). The results indicate a trend to a negative offset for longer storage times of the ions.

negative offsets is visible for larger storage times, pointing to a physical origin of the observed effect. As this loss occurs only slowly over several minutes it does not influence the lifetime extracted from 1.5 second intervals besides causing the observed offset.

A plausible explanation of this observation is provided by the effect of laser induced recombination as discussed in [KKW+97, BBE+95]. In the electron cooler of the ESR

the ion beam is overlapped with an electron beam of precisely known velocity to cool the ions. The laser excitation of the ions happens on the same side of the storage ring, which means that when a laser pulse arrives, we have an intense photon beam in addition to the ions and electrons in the cooler. By irradiation with the laser field it is possible to combine free electrons and ions into specific high-lying Rydberg states of the highly charged ions following the reaction

$$A^{n+} + e^- + \hbar\omega \rightarrow A^{(n-1)+} + 2\hbar\omega \; . \tag{4.6}$$

This effect has previously been observed using bare Ar^{18+} ions at the ESR by Borneis et al. [BBE+95]. With an additional captured electron the charge state of the HCI changes and the ions are not longer hold on orbit inside the ESR, but get lost. In contrast to

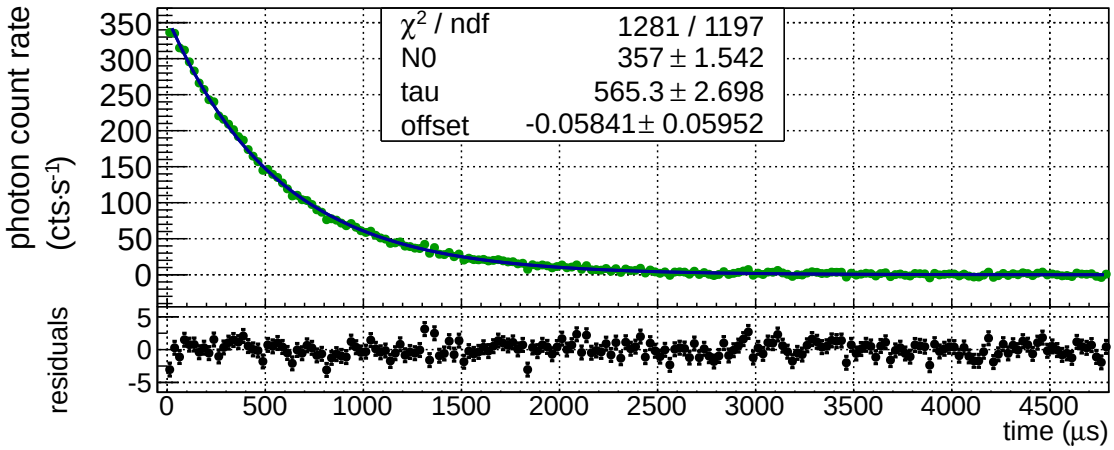

Figure 4.8: Extracted lifetime curve for $^{209}Bi^{82+}$using the background correction within the bin-method. No significant offset can be observed.

the data taken for Li-like Bismuth, no negative offset was observed for the H-like case. This is explained by the fact, that laser induced recombination is a resonant process that requires a Rydberg state with an appropriate level energy to be available. In the H-like case the energy of the laser photons in the ions rest frame is 5.1 eV, more than six times higher than in the Li-like case and at that energy, there is apparently no suitable energy level present for laser induced recombination to happen at a significant scale (cf. fig. 4.8).

4.3 Beam time 2011

The focus of the 2011 beam-time was the search for the HFS resonance in lithium-like bismuth, which was unsuccessful in earlier experiments [Kla94, Win99]. While this search was a success [Jö13, Loc13], there were only a few hours left at the end of the beam-time for a measurement of the lifetime of the state.

To measure the $^{209}Bi^{80+}$ lifetime a shutter was introduced into the laser setup to block the laser shots during periodic intervals and extend the time in which the ions can de-excite without being excited by the laser again. This is necessary due to the long lifetime of $^{209}Bi^{80+}$ of about $\tau^{\text{lab}}_{\text{theory}} \approx 116$ ms (as predicted by [SST+98]). In the last three hours of the beam-time 2011 the shutter was in operation and 12 data sets were recorded from which seven fulfilled the selection criteria (see sec. 4.1) and were used for the lifetime analysis. All datasets were recorded with bunched ion beam.

4.3.1 Lifetime analysis

The lifetime curve extracted via the bin-method is shown in figure 4.9 together with the fit function given in eq. 4.5.

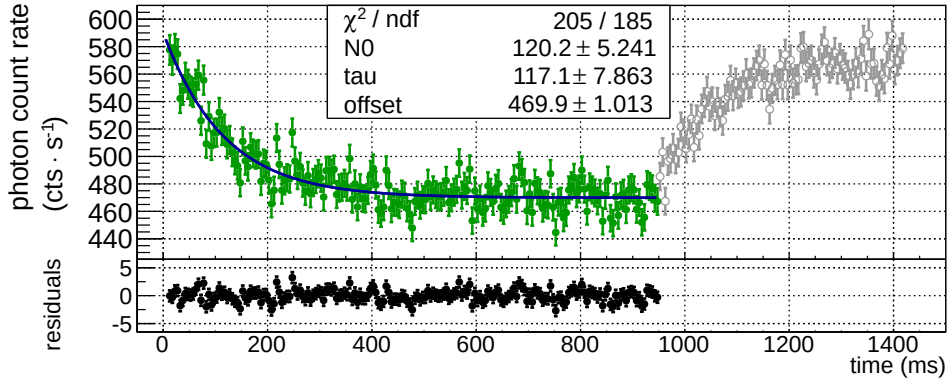

Figure 4.9: Lifetime data extracted via the bin-method for lithium-like bismuth from the beam-time 2011 together the fit function (eq. 4.5) consists out of an exponential decay and a constant offset. For the extraction a window around the signal peak at bin 116 with a width of $\pm 2\sigma$, i.e. 14 bins, was used. For the lifetime fit only the green, filled circles are used. After about 950 ms the shutter reopens and the ions are excited again. The reduced χ^2 is close to one with $\chi^2_{\text{red.}} = 1.11 \pm 0.10$.

The result for the lifetime is:

$$\tau_{\text{bin}}^{\text{Li}} = (117.1 \pm 7.9)\ \text{ms} \qquad (4.7)$$
$$\chi^2_{\text{red.}} = 1.11 \pm 0.10$$

The given error is purely statistical.
With the given fit function only about 67 % of the data, namely the first 950 ms, are used. The remaining part shown in figure 4.9 as gray, unfilled circles, depicts the excitation phase during which the upper HFS state is repopulated. To make use of those remaining 33 % of the data the previous fit-model can be extended by taking into account processes of excitation, as well as stimulated emission and spontaneous emission. The rate equation for the population of the upper HFS state $N_2(t)$ than reads:

$$\dot{N}_2(t) = N_1(t)\, B_{12}\, u - N_2(t)\, B_{21}\, u - N_2(t)\, A_{21}\ , \qquad (4.8)$$

with the Einstein coefficients

$$A_{21} = \frac{1}{\tau} \qquad B_{21} = A_{21}\frac{\lambda^3}{8\pi h} \qquad g_1\, B_{12} = g_2\, B_{21}\ . \qquad (4.9)$$

The coefficient for spontaneous emission A_{21} contains the mean lifetime τ. g_1 and g_2 are the number of magnetic sub-states of the ground state ($F = 4$) and the excited state ($F = 5$) of the given HFS transition. $N_1(t)$, $N_2(t)$ are the occupation numbers of the respective state, which yield to the total number of stored ions N via $N = N_1(t) + N_2(t)$. u denotes the spectral energy density. Equation 4.8 can be re-written as follows:

$$\begin{aligned}
\dot{N}_2(t) =& N_1(t)\frac{g_2}{g_1}B_{21}\, u - N_2(t)\, B_{21}\, u - N_2(t)\, A_{21} \\
=& \left\{\frac{g_2}{g_1}N_1(t) - N_2(t)\right\}\, B_{21}\, u - N_2(t)\, A_{21} \\
=& \left\{\frac{g_2}{g_1}(N - N_2(t)) - N_2(t)\right\}\, \frac{\lambda^3 u}{8\pi h}\, \frac{1}{\tau} - N_2(t)\, \frac{1}{\tau} \\
=& \left\{\frac{g_2}{g_1}N - \left(\frac{g_2}{g_1} + 1\right) N_2(t)\right\}\, \frac{\lambda^3 u}{8\pi h}\, \frac{1}{\tau} - N_2(t)\, \frac{1}{\tau}
\end{aligned} \qquad (4.10)$$

With the abbreviation $\phi := \frac{\lambda^3 u}{8\pi h}$ eq. 4.10 simplifies to

$$\begin{aligned}
\dot{N}_2(t) =& \frac{g_2}{g_1} N \frac{\phi}{\tau} - \left(\frac{g_2}{g_1} + 1\right) N_2(t) \frac{\phi}{\tau} - N_2(t) \frac{1}{\tau} \\
=& \frac{g_2}{g_1} N \frac{\phi}{\tau} - \left(\frac{\left(\frac{g_2}{g_1} + 1\right) \phi}{\tau} + \frac{1}{\tau} \right) N_2(t) \\
=& \underbrace{\frac{g_2}{g_1} N \frac{\phi}{\tau}}_{:= a} - \underbrace{\left(\frac{\left(\frac{g_2}{g_1} + 1\right) \phi + 1}{\tau} \right)}_{:= b} N_2(t) \qquad (4.11) \\
=& a - b N_2(t) \qquad (4.12)
\end{aligned}$$

The differential equation 4.12 can be solved by

$$N_2(t) = \frac{a}{b} + c\, e^{-b\,t}\,, \qquad (4.13)$$

where c is a constant, introduced by the boundary conditions at $t = 0$ and is therefore given by

$$N_2(0) = \frac{a}{b} + c \;\Rightarrow\; c = N_2(0) - \frac{a}{b}. \qquad (4.14)$$

Together it yields

$$N_2(t) = \frac{a}{b} + \left(N_2(0) - \frac{a}{b} \right) \exp\left(-b\,t\right) \qquad (4.15)$$

Stimulated emission as well as excitation do not take place during the full measurement interval since the laser is blocked for a defined time. Therefore a distinction is needed, with the two cases

1. $t \leq t_c$: The laser is blocked, therefore only spontaneous emission takes place

2. $t > t_c$: The ions are excited by the the laser and all three processes are taken into account

The corresponding fit function is given by

$$f(t) = \begin{cases} s \cdot N_2(0) \exp\left(-\frac{t}{\tau}\right) + d & \text{for } t \leq t_c \text{ (laser off)} \quad (4.16a) \\ s \cdot \left[\frac{a}{b} + \left(N_2(t_c) - \frac{a}{b}\right) \exp\left(-b\,(t - t_c)\right)\right] + d & \text{for } t > t_c \text{ (laser on)} \quad (4.16b) \end{cases}$$

d accounts for a constant offset and s is a scaling factor containing further experimental parameters like measurement time and observed solid angle. The part for pure decay, equation 4.16a is identical to equation 4.5. The fit results for lifetime curve over the total range is shown in fig. 4.10 and yields:

$$\tau_{\text{bin}}^{\text{Li}} = (116.9 \pm 6.5)\ \text{ms} \quad (4.17)$$

with a reduced χ^2 and $\Delta\chi^2 = \sqrt{\frac{2}{\text{NDF}}}$ value of $\chi^2_{\text{red.}} = 1.02 \pm 0.08$. Compared to the previous result eq. 4.7 the uncertainty is reduced by ≈ 20 %, while the lifetime value is nearly identical.

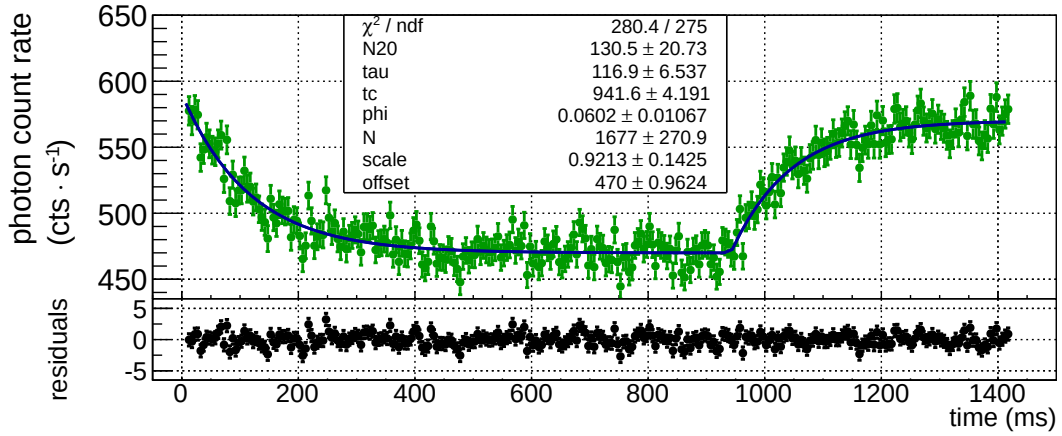

Figure 4.10: Lifetime data extracted via the bin-method for lithium-like bismuth from the beam-time 2011 (cf. fig. 4.9) together with a fit of the complete range. The fit function is given in eq. 4.16. The reduced $\chi^2 = 1.02 \pm 0.08$ agrees with one within the uncertainty and the determined lifetime is consistent with the previous value determined for the decay branch only.

4.3.2 Transformation into the ion's rest frame

All results so far are given in the laboratory frame and have to be converted into the ion's rest frame. For this transition the velocity of the ions needs to be known which is determined from the electron cooler voltage. The cooler voltage and its calibration were

thoroughly investigated in the theses of M. Lochmann and R. Jöhren and can be found in [Jö13], [Loc13] and [LJG+14]. The final result for the Lorentz factor is:

$$\gamma = 1.41865\ (22)\ . \tag{4.18}$$

With the equation for time dilation, $\tau = \tau_{\text{rest}} \cdot \gamma$, the lifetime can be calculated in the ions rest frame:

$$\boxed{\tau^{\text{Li}}_{\text{bin,rest}} = (82.4 \pm 4.6)\ \text{ms}} \tag{4.19}$$

The result agrees with the theoretical prediction of $\tau^{\text{theo}}_{\text{rest}} = (82.85 \pm 0.61)$ ms (cf. sec. 2.2.2).

4.4 Beam time 2014

The major improvement for the beam time in 2014 was the in-situ measurement of the electron cooler voltage and therefore a more precise determination of the velocity of the ions. The velocity is needed for the transformation from the laboratory frame to the ions rest frame.

4.4.1 The Lorentz factor

Via eq. 4.20 the Lorentz factor is determined from the electron cooler voltage which was measured in-situ using a high precision voltage divider provided by the Physikalisch Technische Bundesanstalt (PTB) Braunschweig.

$$\gamma = \left(1 + \frac{E_{\text{kin}}}{E_0}\right) = \left(1 + \frac{-e \cdot U_{\text{eff}}}{m_e \cdot c^2}\right) \tag{4.20}$$

E_{kin} is the kinetic energy of the electrons and E_0 its rest energy. The kinetic energy is given by the product of elementary charge e and the effective acceleration voltage U_{eff} which is the sum of the measured acceleration voltage U_e and space charge corrections Φ:

$$U_{\text{eff}} = U_e + \Phi \quad \text{with:} \tag{4.21}$$

$$\Phi = \xi \frac{[\text{V}]}{[\text{mA}]} \cdot I_{\text{EC}}[\text{mA}] \tag{4.22}$$

ξ has to be determined by performing measurements with different electron cooler currents I_{EC} as described in [UAD+15] or in sections 4.4.5 and 4.4.7. For the hydrogen-like bismuth measurements extracted factor is of the order of $\xi_{\mathrm{H}} = -0.16$ V/mA, while for lithium-like bismuth it is of the order $\xi_{\mathrm{Li}} = -0.185$ V/mA. The highest used electron cooler current was 500 mA leading to a maximum change of the Lorentz factor of $\Delta\gamma \approx 4 \cdot 10^{-4}$.

In fig. 4.11 the measured electron cooler voltage without space charge correction is shown for the whole beam time. On the left side of the vertical dashed line at data set number 737, one drift tube inside the ESR was not properly grounded which caused fluctuations of the acceleration voltage. This problem was fixed during the beam-time and afterwards the voltage was stable. Nevertheless the fluctuations of the voltage lead to an overall variation in γ of less than 0.002, and the effect on the lifetime is therefore negligible at the given level of precision. The measurements performed before the maintenance, can thus still be used for the lifetime analysis.

The mean voltage with space charge correction extracted from the datasets used for the lifetime analysis is for the case of hydrogen-like bismuth found to be $U_{\mathrm{eff}}^{\mathrm{H}} = -(213.90 \pm 0.10)$ kV and for lithium-like bismuth to be $U_{\mathrm{eff}}^{\mathrm{Li}} = -(213.87 \pm 0.05)$ kV. With eq. 4.20 the γ-factors for the two species are found to be:

$$\begin{aligned} \gamma_{\mathrm{H}} &= 1.4186\ (2) \text{ and} \\ \gamma_{\mathrm{Li}} &= 1.4185\ (1). \end{aligned} \tag{4.23}$$

4.4.2 Laser light leak

In a first rough analysis of the Li-like data during the beam time, improbably large values of $\tau \approx 140$ ms were obtained for the lifetime. This problem could be traced back to an incorrect position of the shutter blocking the laser light during the decay periods of the lifetime measurements. As shown in fig. 4.12b, the closed shutter did not block the complete laser halo. A small amount of laser light still entered the ESR through the north-east window. This remaining laser light interacted with the ions in the signal bunch and lead to excitation and stimulated emission even in the one second long decay phase of the measurement interval. In the background corrected lifetime curves this

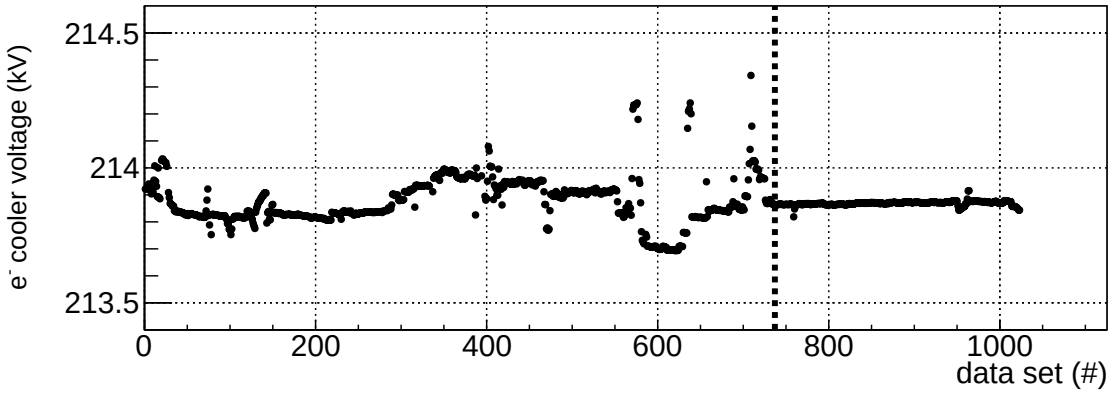

Figure 4.11: In-situ measured electron cooler voltage for the whole beam time without space charge correction. The Lorentz factor for all datasets can be calculated via eq. 4.20. The dashed vertical line marks the time at which a undefined drift tube potential was grounded.

causes a positive offset. The problem was fixed at the same time as the maintenance of the drift tube. To be able to extract a correct lifetime from datasets recorded before the maintenance the fit function introduced with eq. 4.16 has to be adapted. This is only the case for lithium-like bismuth, since the shutter was not needed for hydrogen-like bismuth.

Lifetime fit with residual laser light

To adapt the fit function only the decay phase, i.e. for $t \leq t_c$ has to be changed. In eq. 4.16a only spontaneous emission was taken into account leading to a pure exponential decay. With residual light stimulated emission and excitation have to be added using eq. 4.15 for the number of excited ions, but with a different and lower laser power given by ϕ_r:

$$a = \frac{g_2}{g_1} N \frac{\phi_\mathrm{r}}{\tau} \quad \text{and} \tag{4.24}$$

$$b = \left(\frac{\left(\frac{g_2}{g_1} + 1\right) \phi_\mathrm{r} + 1}{\tau} \right). \tag{4.25}$$

As the numerical value for the residual laser power is expected to be very small, $\phi_\mathrm{r} \ll 1$ the parameter b simplifies to

$$b \approx \frac{1}{\tau}$$

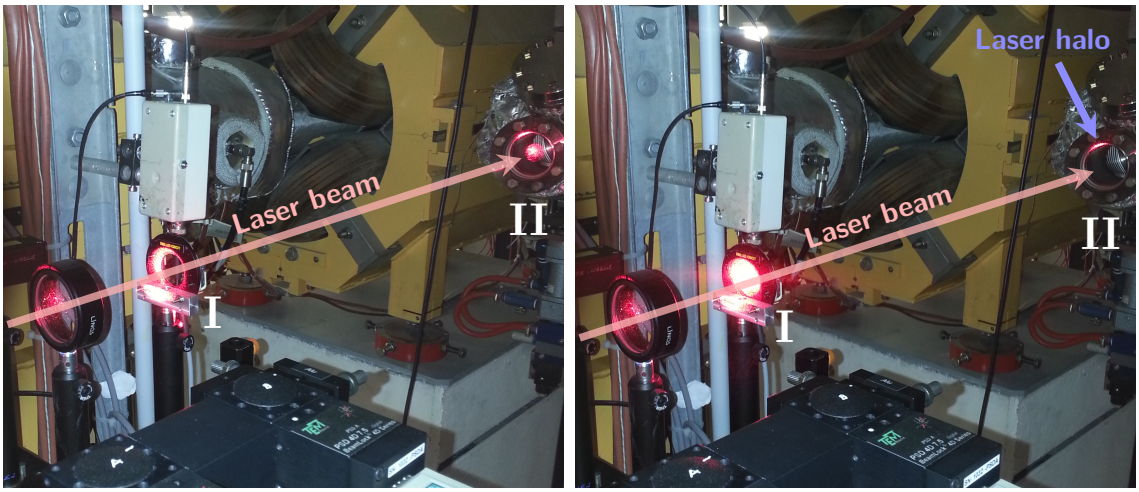

(a) shutter opened **(b)** shutter closed

Figure 4.12: Pictures of the north-east entrance window (II) for the collinear laser beam, with laser optics and shutter (I) in front for the Li-like measurements. The left picture shows the shutter as it is opened. The laser beam passes through and reaches the entrance window. In the right picture the shutter is closed and the main part of the laser beam is blocked. Nevertheless a halo of the laser beam still reaches the entrance window.

leading to

$$\frac{a}{b} \approx \frac{g_2}{g_1} N \phi_\mathrm{r} := c$$

The fit function for the extracted lifetime curves with residual laser light excitation is then given by

$$f(t) = \begin{cases} s \cdot \left[c + (N_2(0) - c) \exp\left(-\frac{t}{\tau}\right) \right] + d & \text{for } t \leq t_c \text{ (laser off)} \quad (4.26a) \\ s \cdot \left[\frac{a}{b} + \left(N_2(t_c) - \frac{a}{b} \right) \exp\left(-b\,(t - t_c)\right) \right] + d & \text{for } t > t_c \text{ (laser on)} \quad (4.26b) \end{cases}$$

The result of the fit for data obtained before the repair of the light leak is displayed in fig. 4.13. As expected the numerical value for ϕ_r is very small, $<10^{-2}$ and we can therefore simplify the fit function 4.26a further, using

$$c = \frac{g_2}{g_1} N \phi_\mathrm{r} \ll N_2(0) \quad (4.27)$$

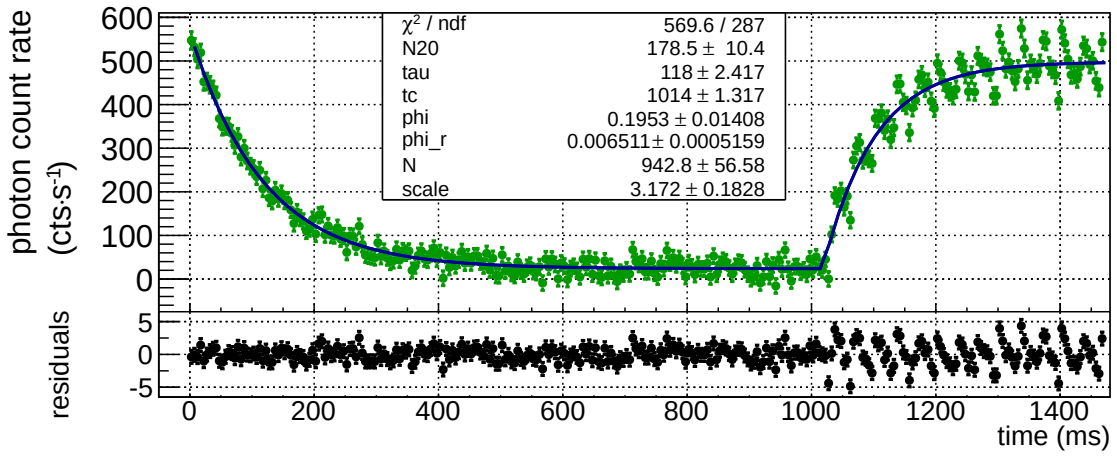

Figure 4.13: Lifetime curves recorded with residuals laser light fitted with the adapted fit function for residual laser light. The lifetime data was extracted with an $\pm 2.5\sigma$ window. The parameter $\phi_r = 0.007$ verifies that only a very small fraction of the laser beam enters the ESR and legitimates the assumption $\phi_r \ll 1$. The $\chi^2_{\text{red.}} > 2$ is due to the laser pulse structure in the excitation phase.

to obtain:

$$s \cdot N_2(0) \exp\left(-\frac{t}{\tau}\right) + d'$$

with $d' = d + c \cdot s$. This is actually equivalent to eq. 4.16. The residual laser light excitation causes a similar effect as an offset. This is displayed in fig 4.14. The lifetime

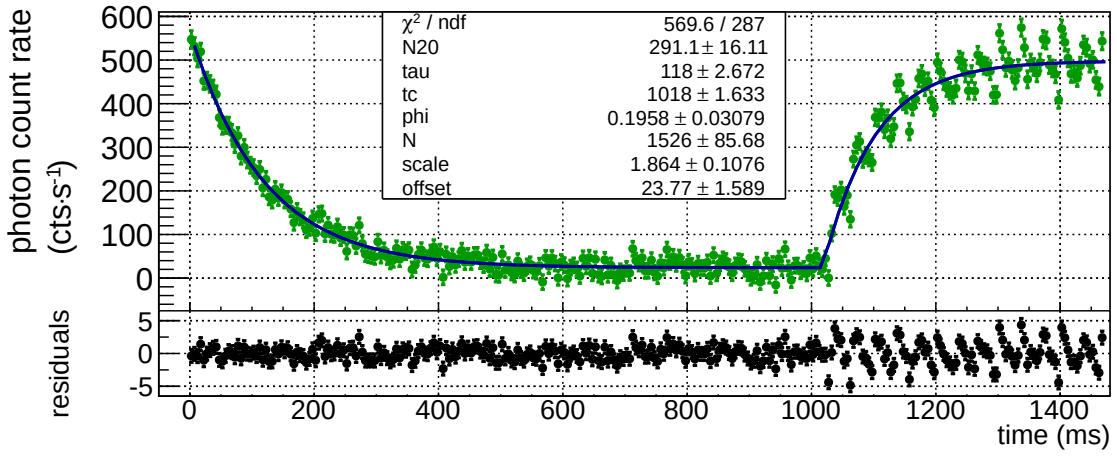

Figure 4.14: Lifetime curves recorded with residuals laser light fitted with the eq. 4.16. The results are in good agreement with the results obtained by taking residual laser power explicitly into account (cf. fig. 4.13).

extracted with the simple offset is in good agreement with the one taking into account

ϕ_r explicitly. Therefore the datasets before and after the maintenance will be handled with the same fit function as given in eq. 4.16. This is even more adequate if a lifetime curve is obtained from data without background subtraction since the contribution to the offset due to residual laser light is much smaller than the offset which is present without background correction, meaning $d \gg c \cdot s$.
An additional feature that can be observed in the high statistics dataset displayed in fig. 4.16 and 4.13 are the individual laser shots, that excite the ions in the rising branch of the data. The fit model eq. 4.16 with an average description of this rise therefore needs to be refined to yield the final fit function as will be described in section 4.4.6. This function will than be used to obtain the final results for the lifetime for lithium-like bismuth.

4.4.3 Evaluation of scan mode data

Besides significant improvements in the monitoring of the electron cooler voltage during the 2014 beam-time a RIO4 real-time computer was used for read out of the VUPROM-device and thus centerpiece of the new DAQ. With this new acquisition it was possible to record lifetime data also during the wavelength scans.

While scanning with the laser frequency over the resonance wavelength of the transition only a small fraction of the recorded data can be used for lifetime determination. To select the data recorded while the laser was on resonance, a rudimentary wavelength analysis is performed for each dataset. In the resulting graph wavelength is plotted versus count rate as shown in fig. 4.15. For lifetime analysis only data from a $\pm 2\sigma$ environment around the resonance wavelength is used. The absolute count rates and the absolute position of the resonance is not of importance for the data selection.

4.4.4 Lifetime of hydrogen-like bismuth

In contrast to the 2011 beam time in 2014 also lifetime data for the H-like HFS state was recorded. The lifetime of hydrogen-like bismuth is predicted to be $\tau_H^{\text{theo}} = (399.01 \pm 0.19)\ \mu$s [Sha98] and was already measured at the ESR in laser spectroscopy experiments by Klaft [Kla94] and Winter [Win99] (cf. tab. 4.1). While the value of Klaft shows a significant deviation from the predicted value, the later measurement by Winter

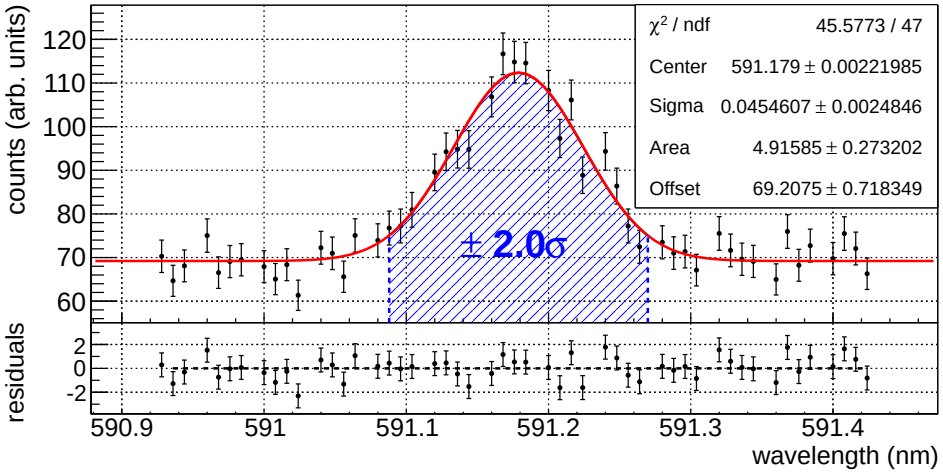

Figure 4.15: Exemplary result of the rudimentary wavelength analysis used to select only data recorded with laser wavelength on resonance. Neither the absolute wavelength nor the absolute count rate is of importance for this purpose. Only the position and width of the distribution is essential to enable for a correct data selection.

Table 4.1: Lifetime values from previous experiments at the ESR and theory.

author	**lifetime (μs)**	**exp/theo**	**year**
Klaft et al.	351 ± 16	exp.	1994 [KBE$^+$94]
Winter et al.	397.5 ± 1.5	exp.	1998 [WBD$^+$98]
Shabaev	399.01 ± 0.19	theo.	1998 [Sha98]

determined the lifetime in agreement with the theory value. With such a short lifetime no further adjustments need to be done to the experimental setup and the laser shot frequency of 30 Hz provides a measurement interval of about 33 ms. Therefore almost every dataset recorded for $^{209}Bi^{82+}$ can be used as lifetime data, as long as the transition wavelength is hit by the laser.

Data was recorded with RF amplitude at the cavities set to $U_{RF} = 0$ V, leading to a coasting beam, as well as $U_{RF} \neq 0$ V (usually $U_{RF} = 500$ V), leading to a bunched beam. The analysis of both cases is presented in the following sections. Lifetime data recorded in coasting mode is called coasting data, data recorded in bunched mode is called bunched data.

Coasting beam data

One dataset with a dedicated lifetime measurement was recorded for $^{209}Bi^{82+}$in coasting mode with standard, i.e. 250 mA, cooler current. For coasting data it is not possible to

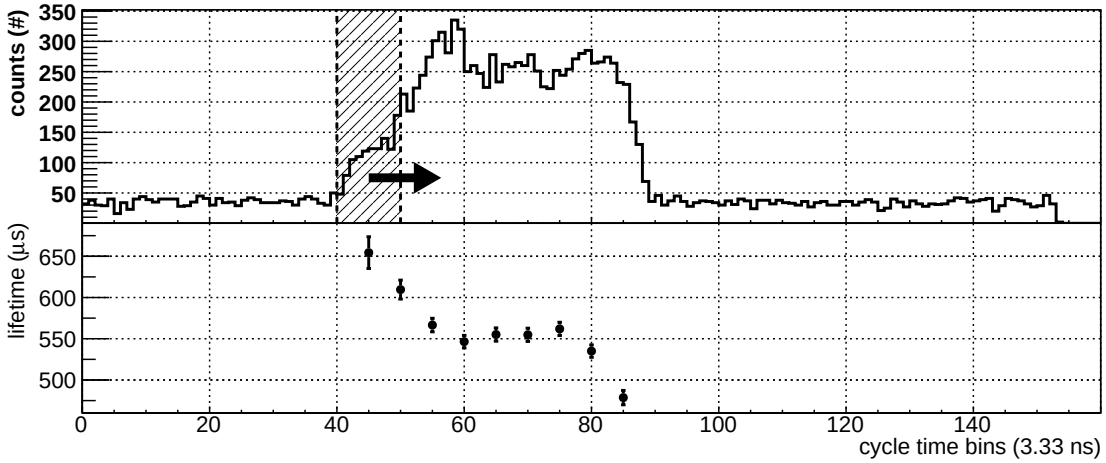

Figure 4.16: To determine the signal region used for the analysis of coasting beam data a 10 bin window indicated by the dashed lines is moved in 5 bin steps over the fluorescence signal (top). The corresponding lifetime is shown in the lower plot. While the lifetime is distorted for windows at the edges, a plateau can be found in the center of the distribution with approximately constant lifetimes. Therefore a window from bin 60 to 80 is used for the coasting beam data analysis.

determine an appropriate time window for the signal peak as presented in sec. 4.2. To choose the optimal window in which entries are considered as signal photons a 10 bin broad window is moved in 5 bin steps over the signal region (cf. fig. 4.16, top). For each window the corresponding lifetime curve is extracted as described in sec. 4.2 and fitted with an exponential fit-function with offset (cf. eq. 4.5) to obtain the lifetime value. The result is shown in fig. 4.16 (bottom) the corresponding data can be found in tab. 4.2. The

Table 4.2: Lifetimes extracted via the bin method for different windows across the signal region (cf. fig. 4.16).

window	**lifetime τ (ms)**	**reduced χ^2**
45 ± 5 bins	654.4 ± 19.2	0.98 ± 0.08
50 ± 5 bins	609.6 ± 11.5	0.92 ± 0.08
55 ± 5 bins	566.6 ± 8.2	1.04 ± 0.08
60 ± 5 bins	546.5 ± 7.6	1.01 ± 0.08
65 ± 5 bins	555.1 ± 8.0	0.96 ± 0.08
70 ± 5 bins	554.8 ± 8.0	1.11 ± 0.08
75 ± 5 bins	561.9 ± 8.1	0.94 ± 0.08
80 ± 5 bins	535.0 ± 7.5	0.88 ± 0.08
85 ± 5 bins	478.6 ± 8.7	0.85 ± 0.08

extracted lifetimes exhibit a large dependence on the window position that is presently not understood. To be able to nevertheless extract a lifetime value from the coasting data a window from bin 60 to bin 80 is used. The lifetimes in this region stay approximately constant as shown in fig. 4.16. The resulting lifetime curve is shown in fig. 4.17. From

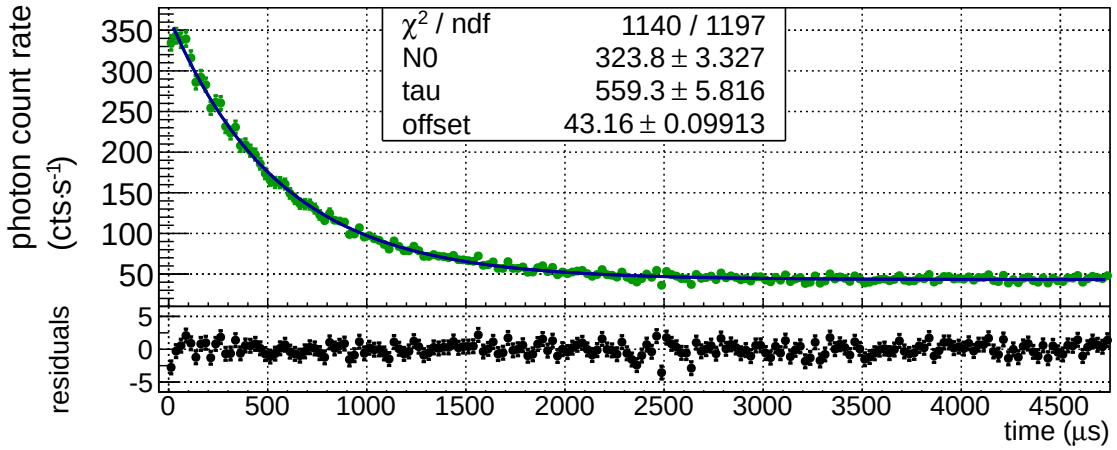

Figure 4.17: Lifetime curve for $^{209}Bi^{82+}$recorded with **coasting** ion beam using the bin-method. No background subtraction is applied, leading to a non-zero offset. The data is fitted with an exponential fit function with $\chi^2_{\text{red.}} = 0.95 \pm 0.04$. The residuals do not show any non-statistical fluctuations and are Gaussian distributed around zero.

this the lifetime for hydrogen-like bismuth recorded with coasting ion beam is found to be

$$\tau_{\text{lab}}^{\text{H,coasting}} = (559.3 \pm 5.8)\ \mu\text{s} \qquad (4.28)$$
$$\chi^2_{\text{red.}} = 0.95 \pm 0.04$$

Bunched beam data

There exists two sets of data with standard settings ($U_{\text{RF}} = 500$ V, $I_{\text{EC}} = 250$ mA) for $^{209}Bi^{82+}$, both recorded with bunched ion beam. One was a dedicated lifetime measurement, the other a scan for the transition wavelength. The location of the fluorescence peak in the bunch structure can be obtained using the procedure illustrated in fig. 4.5. For each time step the resulting fluorescence peak is fitted by a Gaussian, the fit parameters, i.e. center and width are shown in fig. 4.18. While the center of the fluorescence peak is rather stable and shifts only by about ±2 bins the width of the peak changes more pronounced. On a scale of a few 100 μs the peak becomes narrower before

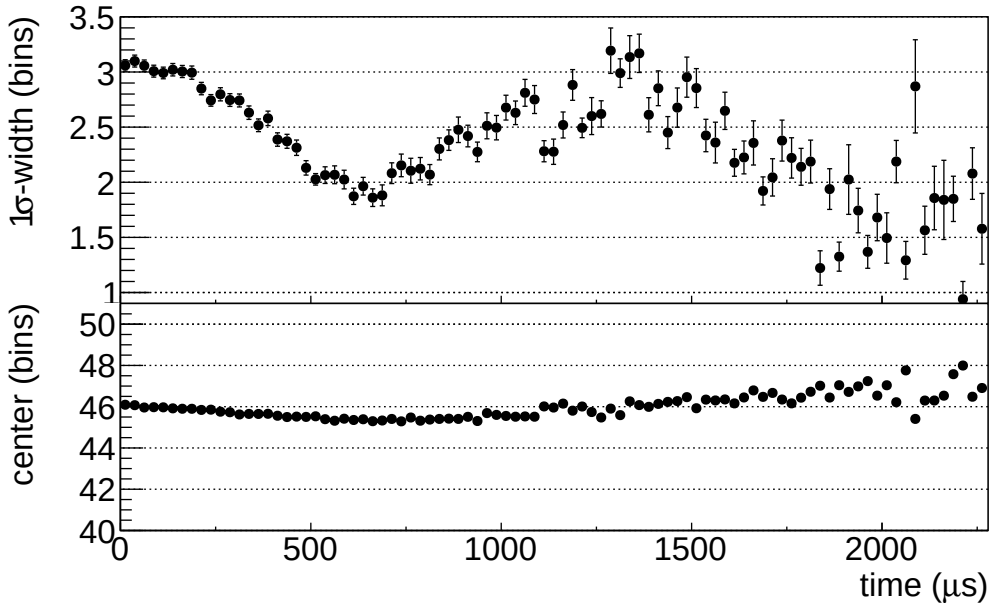

Figure 4.18: Fitted center (bottom) and 1σ-width (top) of the fluorescence peak. While the center is rather constant and shifts only by ± 2 bins the width of the peak changes more pronounced. To prevent that the extracted lifetime is influenced by the fluctuating peak width a sufficiently broad analysis window has to be chosen (cf. fig. 4.19).

it widens again, which is likely due to beam dynamics inside the storage ring. Therefore a broad analysis window is required around the fluorescence peak in order not to be affected by its fluctuating width. To determine which width is sufficient a systematic variation as depicted in fig. 4.19 was performed. For a small analysis window the lifetime is artificially enlarged. With larger windows, starting at $\pm 2.5\sigma$ the effect vanishes and a plateau with constant lifetime is reached. To limit the amount of background counts within the analysis window, a width of $\pm 2.5\sigma$ is therefore chosen.

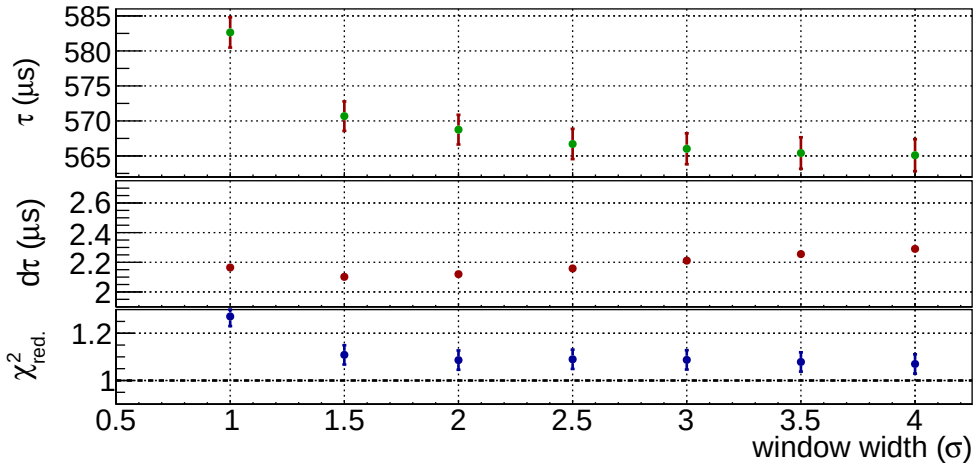

Figure 4.19: The variation of the lifetime in dependence to the analysis window width in $\pm n\sigma$. As expected from fig. 4.18 the lifetime for a small window, i.e. $< 2.5\sigma$ is artificially elongated. Above this value a plateau is reached and the lifetime is rather constant. Hence, for the analysis a window with $\pm 2.5\sigma$ is used. The difference in lifetime between a $\pm 2\sigma$ and $\pm 3\sigma$ broad window to the chosen $\pm 2.5\sigma$ can be used as systematic uncertainty of the analysis.

To determine the systematical uncertainty connected to the analysis method, we fit lifetime curves created with $\pm 2\sigma, \pm 2.5\sigma$ and $\pm 3\sigma$ window width and calculate the differences between the resulting lifetimes. The weighted mean of these differences is then our estimate of the systematical uncertainty for the combined dataset the lifetime curve is shown in fig. 4.20 and the corresponding result is found to be:

$$\begin{aligned} \tau_{\text{lab}}^{\text{H,bunched}} &= (566.7 \pm 2.2_{\text{stat.}} \pm 1.3_{\text{sys.}})\ \mu\text{s} \\ \chi^2_{\text{red.}} &= 1.09 \pm 0.04 \end{aligned} \tag{4.29}$$

The first uncertainty given is purely statistically, the second represents the systematic uncertainty due to the analysis window size.

4.4.5 Systematic effects for $^{209}Bi^{82+}$

Besides technical improvements the beam time in 2014 has the advantage that data was taken to study systematic effects in more detail. Basically there are two different systematics which were recorded:

1. The dependence of the lifetime on the bunch amplitude:

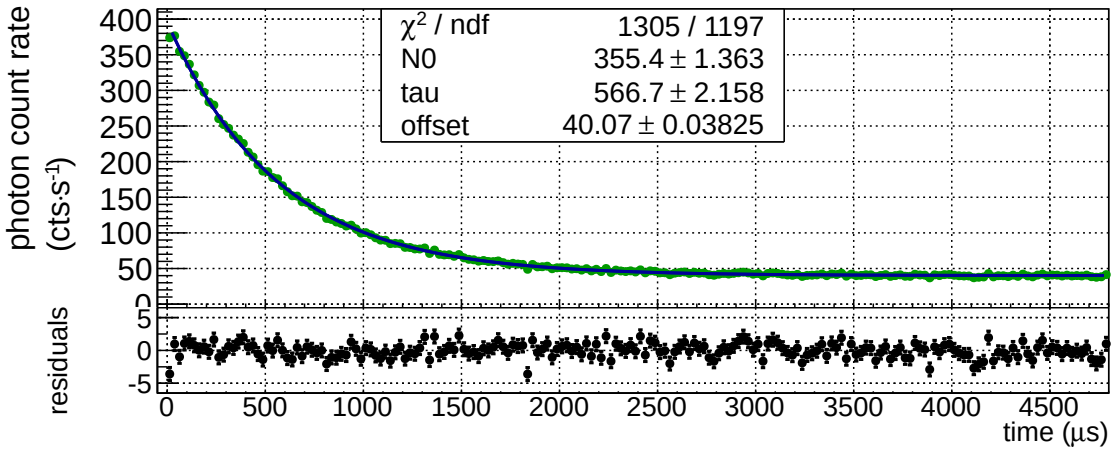

Figure 4.20: Lifetime curve for $^{209}Bi^{82+}$recorded with **bunched** ion beam using the bin-method. No background subtraction is applied, leading to a non-zero offset. The data is fitted with an exponential fit function with $\chi^2_{\text{red.}} = 1.09 \pm 0.04$. The residuals do not show any non-statistical fluctuations and are Gaussian distributed around zero.

A higher RF amplitude U_{RF} applied at the bunching cavities compresses the ion bunches more, leading to a higher ion density. This in turn creates a higher space charge and more ion-ion interactions. With more ion-ion interactions the lifetime might be expected to be shortened due to collisional broadening. To verify such an effect the cavity voltages were varied, while the electron cooler current was fixed at $I_{\text{EC}} = 250$ mA.

2. The influence of the electron cooler current on the lifetime:

   A higher electron cooler current leads to a higher space charge inside the cooler which has an effect on the effective cooler voltage and therefore affects the transition wavelength [Jö13, Loc13]. Those data sets, with systematically varied cooler current and a fixed bunching amplitude can also be used to test for a possible effect on the lifetime. As before a shorter lifetime might be expected with higher electron current, due to de-excitation of the HFS state in ion-electron interaction.

3. The influence of the ion current on the lifetime:

   A similar consideration as for the RF amplitude can be made for the ion current itself. The ion current slowly decreases between ion injections into the ESR. When the ion current is large (e.g. shortly after injection),

the ion density per bunch is higher, with the same consequences as above. To investigate a possible effect on the lifetime, subsets of data with high or low ion current were used for the analysis. As basis the datasets with highest total statistics were used to have reasonable statistics left for each subset.

In all three cases the lifetime is plotted versus the varied quantity, i.e. electron cooler current, bunching amplitude or ion beam current. The data is than fitted with a linear fit function:

$$h(x) = m \cdot x + b \tag{4.30}$$

Of major interest is the slope m of the linear fit, which is zero if no dependence is given. In the case that the lifetime depends on one of the varied quantities a negative slope is expected, as discussed before.
For the error band of the regression line the correlation between the variables is taken into account:

$$\Delta h(x) = \sqrt{\left(\frac{\partial y}{\partial m}, \frac{\partial y}{\partial b}\right) \cdot \mathcal{M}_{\text{cov}} \cdot \begin{pmatrix} \frac{\partial y}{\partial m} \\ \frac{\partial y}{\partial b} \end{pmatrix}} \tag{4.31}$$

With $\mathcal{M}_{\text{cov}}$ being the covariance matrix. To identify the degree of correlation easier the correlation matrix $\mathcal{M}_{\text{cor}}$ is shown in the respective plot with

$$\mathcal{M}_{\text{cor}} = \frac{\mathcal{M}_{\text{cov}}}{\sqrt{\sigma(m)^2 \cdot \sigma(b)^2}}.$$

Influence of RF amplitude on the lifetime

The systematic variation of the bunching amplitude was performed during a regular scan over the resonance. Five different settings were used, with 100 V, 200 V, 300 V, 400 V and 500 V. 500 V meets the standard conditions leading to more available datasets including a dedicated lifetime measurement. The determined lifetime of the combined dataset as stated in eq. 4.29 is used for this data-point. For the remaining voltages only two data files were recorded. The electron cooler current in all cases was fixed at $I_{\text{EC}} = 250$ mA. The results are presented in fig. 4.21 leading to a slope m of

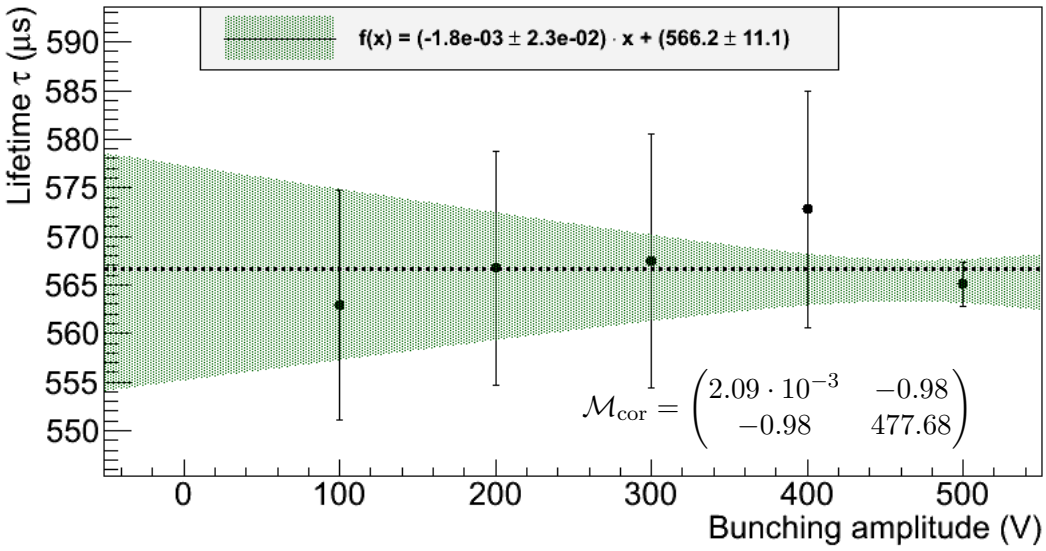

Figure 4.21: Visualized results of the systematic variation of the **bunching amplitude** U_{RF}. Most data were recorded with standard setting, i.e. 500 V bunching amplitude, resulting in the data point with smallest error bar. The dashed line represents the theoretical prediction transformed in the laboratory frame. The slope is compatible with zero within the error.

$$m_{\text{RF}}^{\text{H bunched}} = \quad (-0.0018 \pm 0.023)\ \frac{\mu\text{s}}{\text{V}}$$

indicating an independence between bunching amplitude and lifetime, albeit with the large uncertainty.

Influence of electron cooler current

During scans of the laser wavelength with bunched ion beam, systematic measurements were performed to investigate the influence of the electron cooler current on the resonance. The cooler current was set to 30 mA, 50 mA, 100 mA, 250 mA, and 500 mA. The RF amplitude was fixed at $U_{\text{RF}} = 500$ V. Except for 500 mA with only one dataset, due to instabilities of the ion bunches which occurred with this setting, six datasets were recorded. An overview over the results is shown in fig. 4.22. The graph does not display a visible trend of the lifetimes with the electron cooler current and a linear fit to the data results in a slope of

$$m_{\text{EC}}^{\text{H,bunched}} = (-0.020 \pm 0.026)\ \ \frac{\mu\text{s}}{\text{mA}}$$

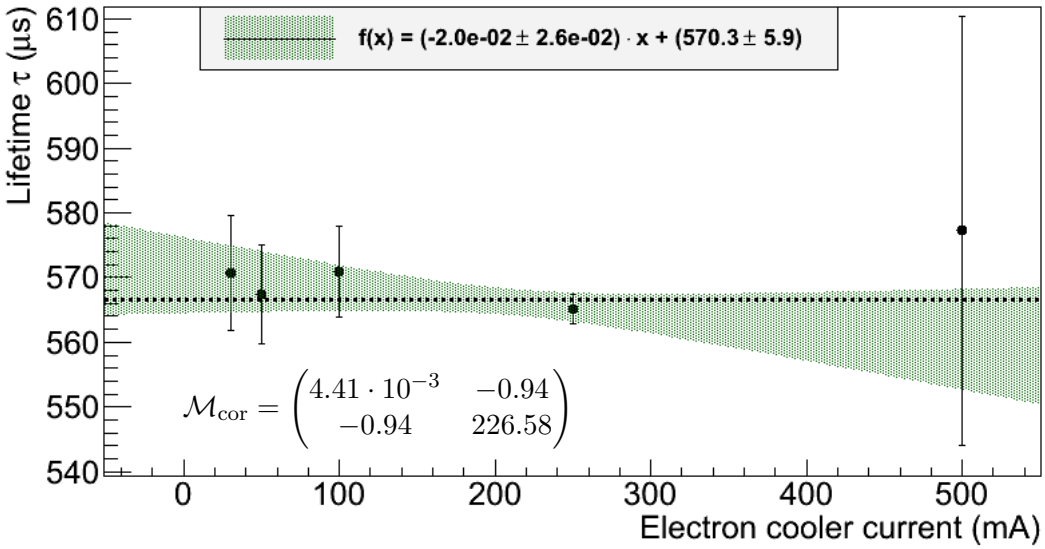

Figure 4.22: Visualized results of the systematic variation of the **electron cooler current**. Most data were recorded with standard setting, i.e. 250 mA electron cooler current, resulting in the data point with smallest error bar. The dashed line represents the theoretical prediction transformed in the laboratory frame. The slope is compatible with zero.

which is compatible with zero indicating an independence between electron cooler current and lifetime within a large uncertainty.

Influence of the ion current on the lifetime

To investigate a possible effect of the ion current on the lifetime, subsets of data with different ion current intensities were used for the analysis. As base the datasets with highest total statistics were used to have a reasonable amount of data left for each subset. Yet the statistics are quite low, leading to relatively high uncertainties. The results is presented in the fig. 4.23 leading to a slope m of

$$m_{\text{IC}}^{\text{H,bunched}} = (-0.015 \pm 0.047)\ \frac{\mu\text{s}}{\mu\text{A}}.$$

Therefore an independence between ion current and lifetime can be assumed within a large uncertainty.

Summarizing it can be said that no indications for a dependence of the lifetime on the bunch amplitude, the electron cooler current or the ion current has been observed with the caveat, that the statistical uncertainties of the systematics measurements are too large to make a strong statement.

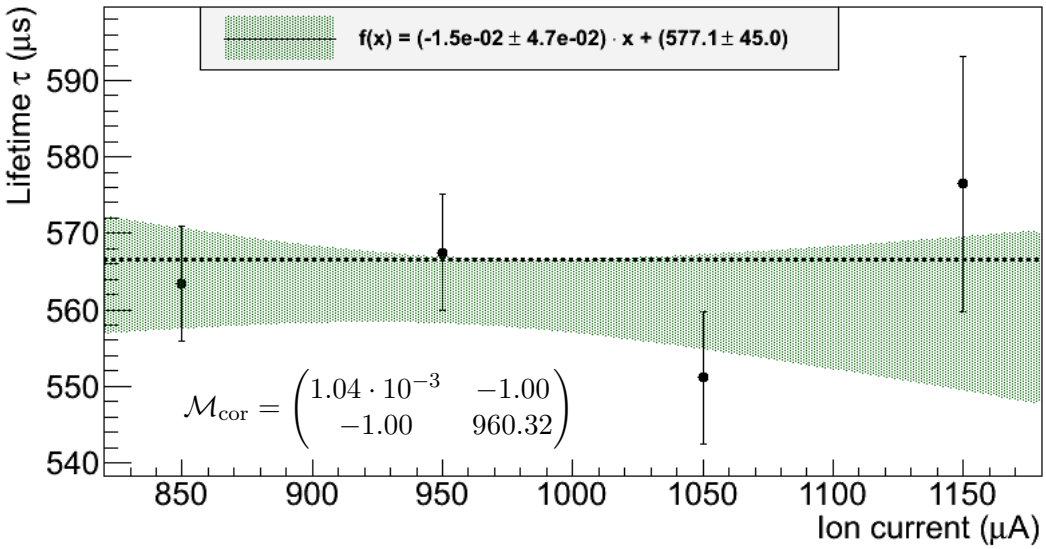

Figure 4.23: Visualization of the systematic variation of the **ion current** and its influence on the lifetime. The dashed line represents the theoretical prediction transformed into the laboratory frame. The slope is compatible with zero.

4.4.6 Lifetime of lithium-like bismuth

With the new DAQ it was possible to record lifetime data throughout the whole beam-time. However, with the long lifetime of $^{209}Bi^{80+}$ usually only the first $\approx$ 30 ms of the exponential decay are recorded if no shutter is placed in the laser beam line. After that time the ions are excited again and the decay starts from the beginning. Half of the systematic measurements were performed in scan-mode where no shutter was used and only 30 ms of the lifetime curve are available. This data is furthermore reduced, since only data taken with the laser frequency on resonance is suitable for lifetime analysis. The remaining data is not sufficient for a reliable lifetime fit. Therefore datasets recorded in scan-mode are not analyzed for $^{209}Bi^{80+}$.

Although measurements were performed with coasting and bunched beams of Li-like ions the search for the resonance with coasting beam remained unsuccessful. Therefore no coasting lifetime data is available for $^{209}Bi^{80+}$ and only bunched data is discussed in the following.

Bunched beam data

For the analysis of the lithium-like lifetime, the data sets with standard settings are used, i.e. $I_{\mathrm{EC}} = 250$ mA and $U_{\mathrm{RF}} = 500$ V. Data are analyzed using the method

described in sec. 4.2.2 without background subtraction. With this method the position of the fluorescence peak can identified accurately. To find the optimal width for the lifetime analysis a systematic variation of the analysis window width was performed for the datasets before and after the laser light leak repair (cf. fig. 4.24). The plot shows the

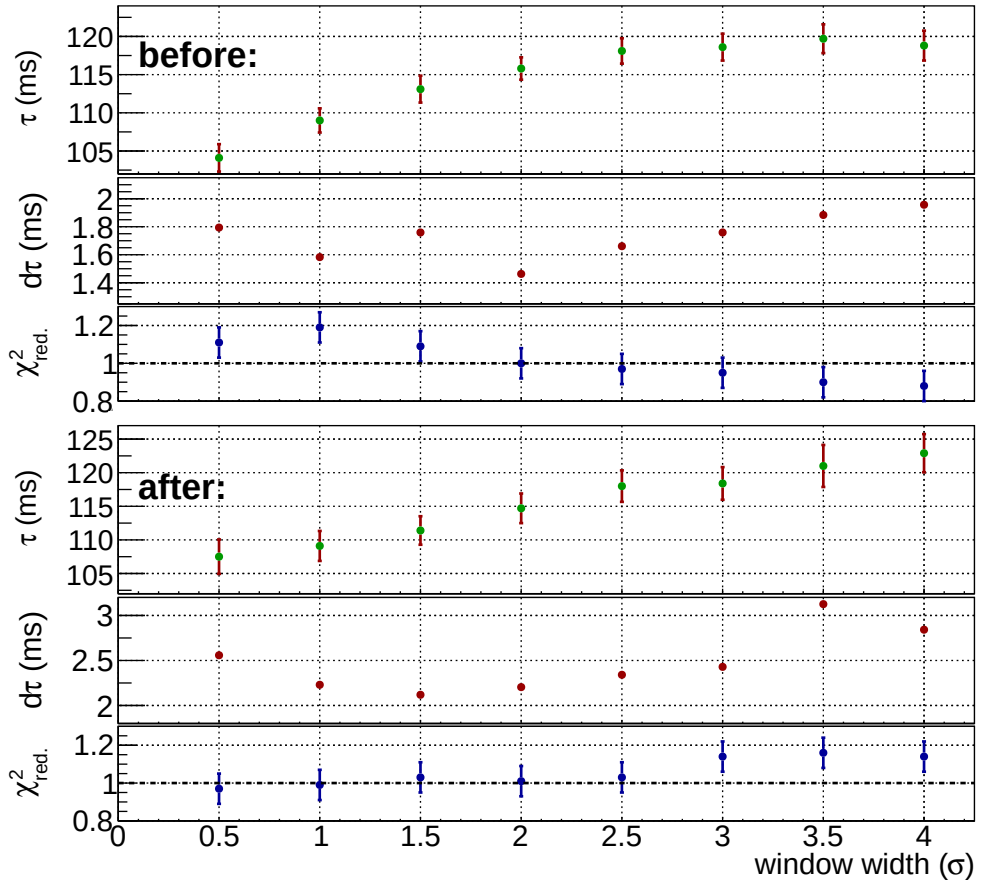

Figure 4.24: Systematic variation of the width of the time window around the fluorescence peak. Broader windows lead to longer lifetimes until a window width of $\pm 2.5\sigma$ where a plateau is reached. Since the reduced χ^2 as well as the uncertainty of the lifetime worsens with even larger windows, the lifetime curves for the final analysis are extracted with a window width of $\pm 2.5\sigma$.

lifetime, its uncertainty and the reduced χ^2 as function of $n\sigma$, respectively. In both cases (before and after the repair) the lifetime increases with increasing n until a plateau is reached at $n = 2.5$. Higher values are excluded for the analysis due to a $\chi^2_{\text{red.}}$ incompatible with 1 and larger uncertainties of the lifetime. For the final analysis the lifetime curves will therefore be extracted with a time window around the fluorescence peak of $\pm 2.5\sigma$ width.

The dependence of the lifetime on the time window width is not expected and implies

that excited highly charged ions move out of the window, get lost for the analysis and lead in this way to an artificially shortened lifetime. This can be explained either by a broadening fluorescence peak (cf. fig. 4.25 a)) or if the peak moves out of the analysis window (cf. fig. 4.25 b)). The former effect starts with the excitation by the laser, after

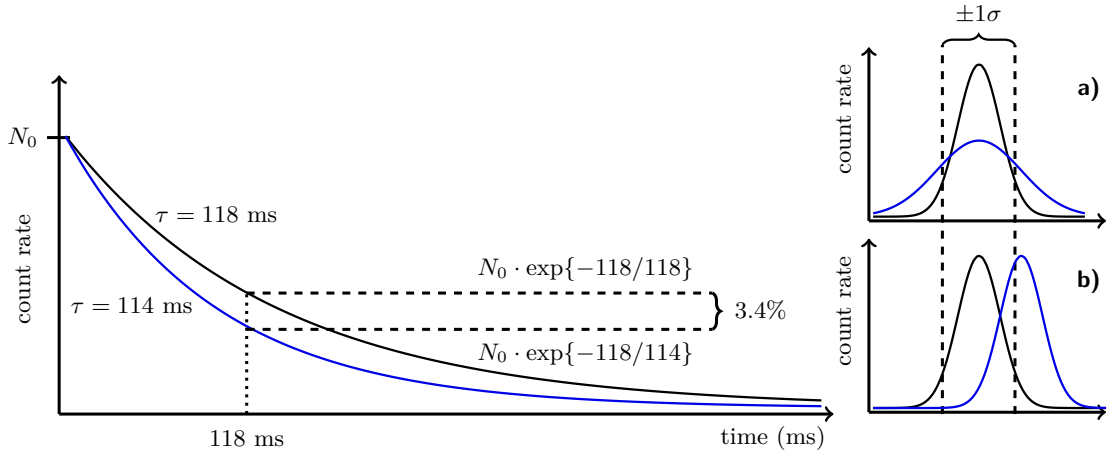

Figure 4.25: Scheme of the two possible processes leading to a artificially shortened lifetime. In both cases excited ions leave the analysis time window. This can either happen due to a broadening of the peak (a), or the entire peak is shifted out of the analysis window (b). All curves are not to scale.

which the fluorescence peak has a width of typically $1\sigma = 3$ bins. During the decay period, the peak widens until the effect is reset by the opening of the shutter after about one second. The linear effect (b) on the other hand is due to inexact timing and grows linearly throughout the complete lifetime curve.

To investigate which of the two cases describes the observed shortening of the lifetime the fluorescence peak corresponding to each time step of the lifetime curve was fitted with a Gaussian to obtain its position and width in σ. The result is shown in fig. 4.26. Between $\approx$ 400 ms and $\approx$ 1000 ms, most of the excited ions have decayed and the fluorescence peak is therefore to weak to be fitted. One can estimate the expected effect by determining which modification of the fluorescence peak will lead to the appropriate loss of count rate of e.g. 3.4 % as schematically shown in fig. 4.25, left. The result for a broadening of the peak is shown as dashed line in fig. 4.26, upper plot. Since the broadening of the fluorescence peak is reset by the next laser pulse, the dashed line in the upper plot is supposed to match only data-points within the first half of the plot. The lower dashed line shows the required effect for a shifting fluorescence peak to yield

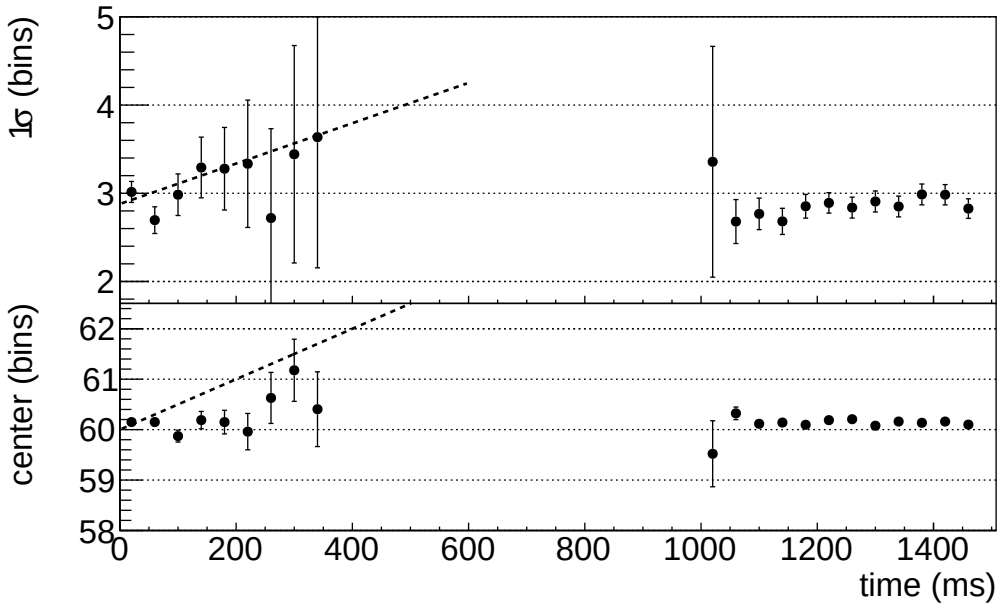

Figure 4.26: Center (bottom) and σ (top) of the fitted fluorescence peak over 1500 ms. The dashed line indicates the trend how it is expected if one or the other effect occurs. The upper dashed line has to describe only the data-points up to 1000 ms, because at this point the shutter is re-opened and the ions located in the center of the analysis time window are excited. The data-points agree well with the expectation. The lower dashed line is supposed to describe all data-points, since the shift of the fluorescence peak due to inexact timing will not restart at any time.

to a lifetime reduced by 3.4 %. Since this effect is due to inexact timing it affects the fluorescence peak continuously, i.e. the peak moves further out of the analysis window, without being relocated in its center at any time. Thus all data-points in the lower plot should match the dashed line, which is clearly not the case. Therefore it can be assumed that the decreasing lifetime with decreasing window width, as shown in fig. 4.24, is due to a broadening fluorescence peak. To counteract this effect the analysis window has to be large enough. For the final analysis a $\pm 2.5\sigma$ window is used since a rather constant lifetime is expected from this value on (cf. fig. 4.24).

Defined fit function

The fit function can be further refined by accounting for the individual laser pulses in the excitation phase. In fig. 4.14 one can see that the laser pulse structure becomes visible in the rising branch of the lifetime curve with the higher statistics collected in 2014. To take advantage of the excitation phase the total range of the lifetime should be fitted, but so far the fit model eq. 4.16 accounts only for an averaged laser power and

does not consider the individual laser pulses. Therefore a modification of the model

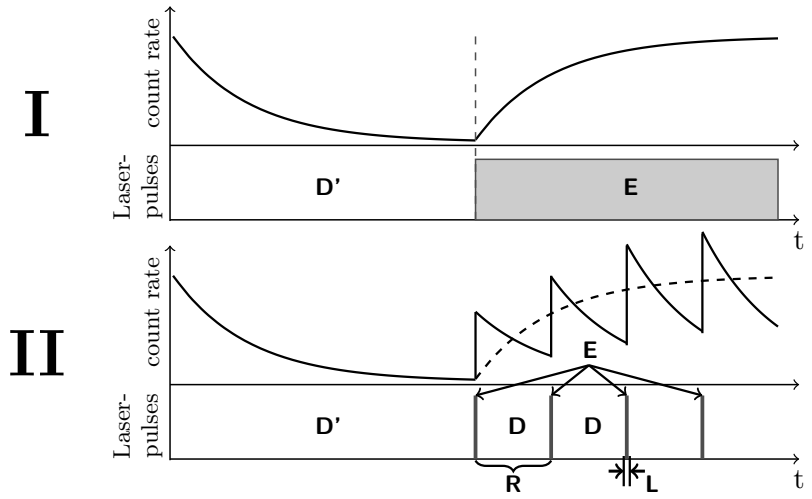

Figure 4.27: Scheme of the fit function with and without laser pulse implementation. In (**I**) only a continuous laser beam during the excitation phase with an average laser power is taken into account. (**II**) illustrates how the continuous laser beam during the excitation is split up into several short laser pulses (**E**) of length (**L**) and a rather long decay phase (**D**) within a repetition interval **R**. The used laser system emits 10 ns pulses with a repetition rate of 30 Hz. Not affected is the decay phase **D'** during which the laser is completely blocked by the shutter.

is required. The modified fit model does not use a low, average laser power to excite the ions continuously in the rising branch of the lifetime curve (cf. fig. 4.27 (I)). Instead it implements short intervals, as schematically shown in fig. 4.27 (II) with a repetition interval **R** during which laser excitation and stimulated emission are taken into account (**E**), followed by intervals of pure spontaneous emission (**D**). The used laser system emits laser pulses with a length **L** of 10 ns and a repetition rate of 30 Hz. Within the fit function each point of the rising branch is calculated from the previous excitation and the intervening decay phase. The actual implementation of the fit function can be found in appendix A.2.

The lifetime data recorded before (top) and after (bottom) the maintenance together with the fits is shown in fig. 4.28. The lifetimes of both datasets agree well with each other and are found to be:

$$\begin{aligned} \tau^{\text{Li,bunched}}_{\text{lab, before repair}} &= (118.1 \pm 1.8)\ \text{ms} \\ \chi^2_{\text{red.}} &= 0.97 \pm 0.08 \text{ and} \\ \tau^{\text{Li,bunched}}_{\text{lab, after repair}} &= (118.0 \pm 2.3)\ \text{ms} \\ \chi^2_{\text{red.}} &= 1.03 \pm 0.08 \text{ and} \end{aligned} \tag{4.32}$$

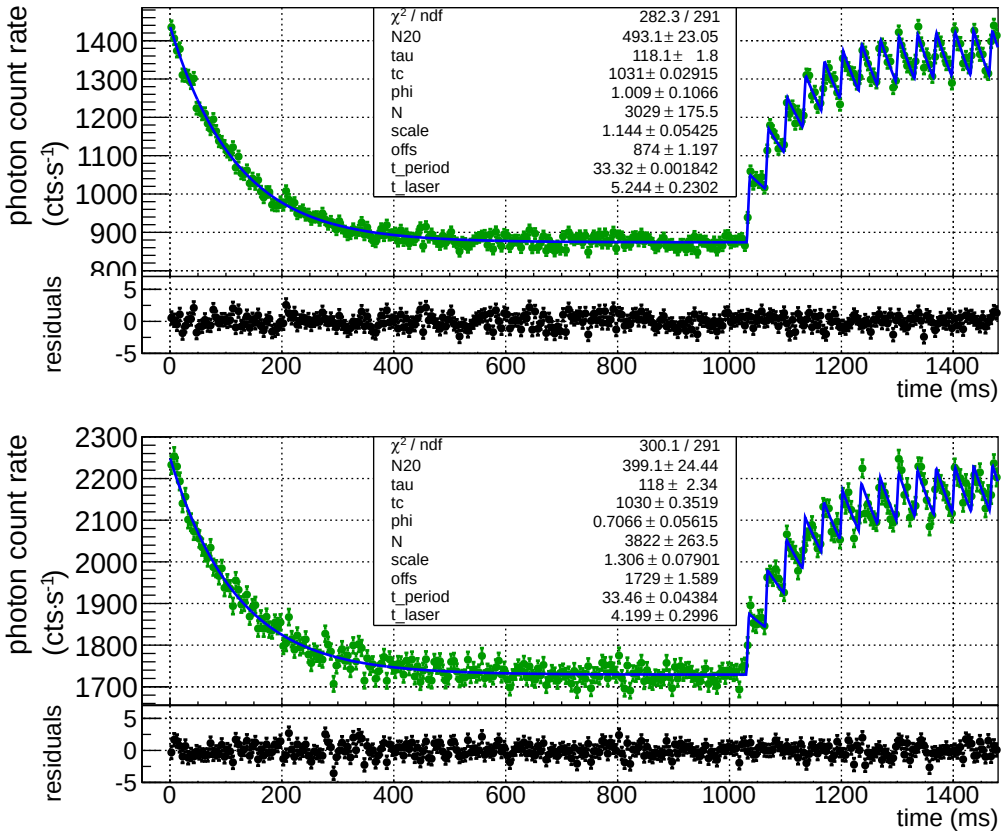

Figure 4.28: $^{209}Bi^{80+}$lifetime data taken before (top) and after (bottom) the maintenance. The result is obtained via the bin-method from the dataset recorded with standard settings ($I_{EC} = 250$ mA and $U_{RF} = 500$ V). Signals within a $\pm 2.5\sigma$ analysis window around bin 56 were used. The data is fitted with the modified fit function as stated in appendix A.2 which takes the laser pulse structure into account. The parameter `t_period` represents the laser shot period and matches quite well with the experimentally given 30 Hz. By considering the laser pulse in the fit function the $\chi^2_{red.}$ is much improved and close to one in both cases. The lifetimes agree well with each other.

In addition the dependence of the lifetime on the analysis window width entail a systematic uncertainty which is estimated from the weighted mean of the differences of lifetimes obtained with a ± 2.0, ± 2.5 and a $\pm 3.0\sigma$ analysis window, as it is displayed in fig. 4.24. For the dataset before the repair the estimated systematic uncertainty is ± 1.0 ms, while it is ± 1.3 ms after the repair. In a conservative approach the higher value is used as the systematic uncertainty for the final result, which is given as the weighted mean of the lifetime values given in eq. 4.32 and is found to be:

$$\tau^{\text{Li,bunched}}_{\text{lab, combined}} = (118.1 \pm 1.4_{\text{stat.}} \pm 1.3_{\text{sys.}})\ \text{ms} \tag{4.33}$$

The first uncertainty given is purely statistical, the second is the systematic uncertainty due to the analysis window size. As cross-check the decay phase of both data sets are fitted with a simple exponential fit function and an offset as can be found in appendix A.3.

4.4.7 Systematic effects for $^{209}Bi^{80+}$

For lithium-like bismuth only dedicated lifetime measurements can be used for the lifetime analysis. In scan mode without shutter the long lifetime of this species leads to a clipped lifetime curve which can not be used reliably for the analysis. Therefore much less data is available for systematic checks compared to the $^{209}Bi^{82+}$case. All measurements were performed in bunched mode, most of them before the repair. As already discussed they can be handled using the fit function eq. 4.26.

Influence of RF amplitude on the lifetime

For the measurement of possible effects of the bunching amplitude on the lifetime the applied voltage was varied and set to 100 V, 200 V, 500 V and 700 V. The electron cooler

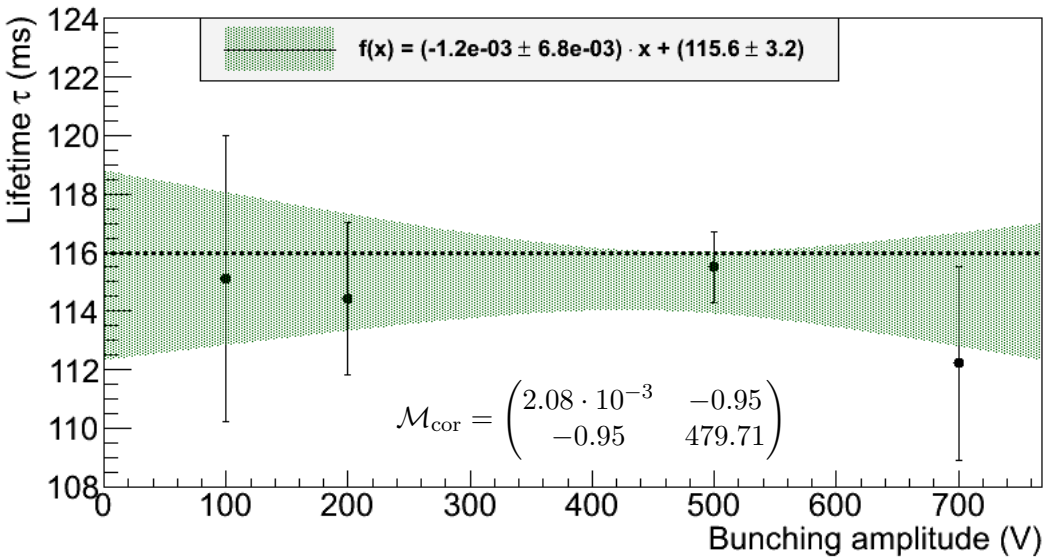

Figure 4.29: Visualized results of the systematic variation of the **bunching amplitude** U_{RF} for the uncorrected signal. The dashed lines represent the theoretical prediction transformed in the laboratory frame. The slope is compatible with zero within the uncertainty.

current was set to the standard setting of $I_{\mathrm{EC}} = 250$ mA. The corresponding results are shown fig. 4.29. The slope is found to be

$$m_{\mathrm{RF}}^{\mathrm{Li,bunched}} = (-0.0012 \pm 0.0068)\ \frac{\mathrm{ms}}{\mathrm{V}}$$

Therefore an independence between ion current and lifetime can be assumed, albeit with a large uncertainty.

Influence of electron cooler current

To investigate the dependence between electron cooler current and lifetime three data-points were recorded with the cooler current set to 50 mA, 150 mA and 250 mA. The

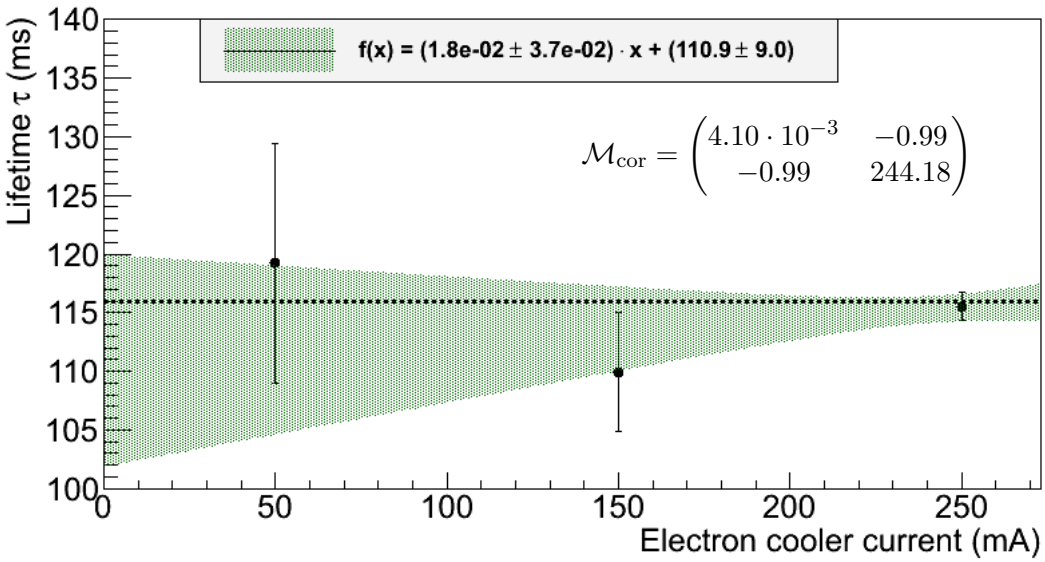

Figure 4.30: Visualization of the systematic variation of the **electron cooler current** and its influence on the lifetime. The dashed line represents the theoretical prediction transformed into the laboratory frame.

bunching amplitude was fixed at $U_{\mathrm{RF}} = 500$ V. While a large set of data is available for the data-point at 250 mA, which is the standard setting, only one dataset for 50 mA and two datasets for 150 mA are available. The corresponding visualization is shown in fig. 4.30. The linear fit returns a slope m of

$$m_{\mathrm{EC}}^{\mathrm{Li,bunched}} = (0.018 \pm 0.037)\ \frac{\mathrm{ms}}{\mathrm{mA}},$$

indicating an independence between bunching amplitude and lifetime, albeit with a large uncertainty.

Influence of the ion current on the lifetime

To obtain information about the dependence of the lifetime on the ion current the datasets with highest total statistic are used to create subsets of data with different mean ion current. The results are presented in fig. 4.31. The slope is found to be

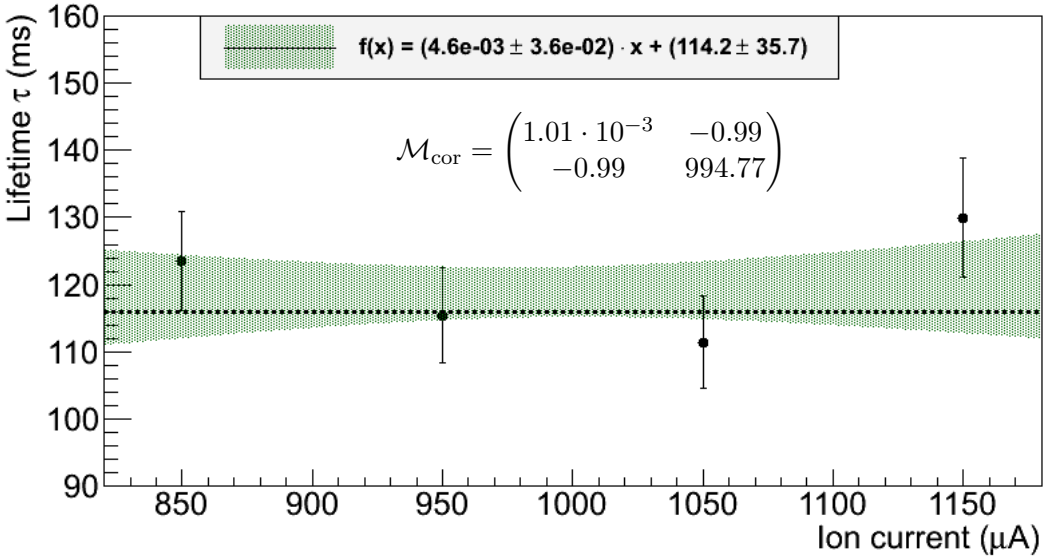

Figure 4.31: Visualization of the systematic variation of the **ion current** and its influence on the lifetime. The dashed line represents the theoretical prediction transformed into the laboratory frame.

$$m_{\mathrm{IC}}^{\mathrm{Li,bunched}} = (-0.0046 \pm 0.036)\ \frac{\mathrm{ms}}{\mu\mathrm{A}}$$

which suggests no lifetime dependence on the bunching amplitudes within the large uncertainty.

4.5 Final results of the lifetime analysis

The results of the beam-time 2014 are given in the laboratory frame so far and have to be transformed into the ions rest frame. For this purpose the acceleration voltage of the electron cooler was recorded. The voltage for measurements with hydrogen-like bismuth are found to be $U_{\mathrm{eff}}^{\mathrm{H}} = -(213.90 \pm 0.10)$ kV and for lithium-like bismuth $U_{\mathrm{eff}}^{\mathrm{Li}} =$

$-(213.87 \pm 0.05)$ kV. The resulting γ-factors for the two bismuth species are calculated with eq. 4.20 to be:

$$\begin{aligned} \gamma_{\mathrm{H}} &= 1.4186\ (2) \text{ and} \\ \gamma_{\mathrm{Li}} &= 1.4185\ (1). \end{aligned} \tag{4.34}$$

4.5.1 H-like bismuth

For the H-like case, lifetimes have been extracted both from coasting and bunched beam data. The analysis of the coasting beam data exhibits a so far not understood dependence of the lifetime on the analysis time window placed around the signal region of the stored ions (cf. fig. 4.16). The lifetime extracted with an intermediate time window is significantly lower than the one extracted from bunched beam measurements and has a large uncertainty. This is contrary to the expectation, that the lower ion density present in the coasting beam measurements should, if it has an influence at all, lead rather to a longer lifetime value. For the final result on the lifetime of the HFS state in H-like bismuth, we therefore disregard the coasting beam data. In bunched mode most statistics were accumulated with the standard settings ($U_{\mathrm{RF}} = 500$ V, $I_{\mathrm{IC}} = 250$ mA) leading to the following value for the lifetime of the 1s hyperfine transition in the lab system

$$\tau_{\mathrm{lab}}^{\mathrm{H,bunched}} = (566.7 \pm 2.2_{\mathrm{stat.}} \pm 1.3_{\mathrm{sys.}})\ \mu\mathrm{s} \quad \text{(cf. eq. 4.29)}$$

And together with the Lorentz factor it leads to a lifetime in the ion's rest frame of:

$$\boxed{\tau_{\text{H-like}} = (398.5 \pm 1.6_{\mathrm{stat.}} \pm 0.9_{\mathrm{sys.}})\ \mu\mathrm{s}} \tag{4.35}$$

Which is in good agreement with theory and with the experimental value of Winters et al.:

$$\begin{aligned} \tau_{\mathrm{H}}^{\mathrm{theo}} &= (399.01 \pm 0.19)\ \mu\mathrm{s} \quad \text{[Sha98]} \\ \tau_{\mathrm{H}}^{\mathrm{exp}} &= (397.5 \pm 1.5)\ \mu\mathrm{s} \quad \text{[Win99]} \end{aligned}$$

The uncertainty on the experimental value published by Winters et al. does not contain systematic uncertainties.

4.5.2 Li-like bismuth

For lithium-like bismuth the lifetime of the 2s hyperfine transition is found to be:

$$\tau_{\text{lab}}^{\text{Li,bunched}} = (118.1 \pm 1.4_{\text{stat.}} \pm 1.3_{\text{sys.}})\ \text{ms} \quad \text{(cf. eq. 4.33)}$$

The first uncertainty is purely statistical, the second accounts for the uncertainty due the choice of the analysis window width. Together with the Lorentz factor it leads to a lifetime in the rest frame of:

$$\boxed{\tau_{\text{Li-like}} = (83.3 \pm 1.0_{\text{stat.}} \pm 0.9_{\text{sys.}})\ \text{ms}} \tag{4.36}$$

Which is as well, in good agreement with theory:

$$\begin{aligned} \tau_{\text{Li}}^{\text{theo}} &= (82.0 \pm 1.4)\ \text{ms} \quad [\text{SST}^{+}98] \\ \tau_{\text{Li}}^{\text{theo}} &= (82.85 \pm 0.61)\ \text{ms} \quad \text{(cf. sec. 2.2.2)} \end{aligned}$$

No other experimental data are available for comparison.
The systematic uncertainty included in the lifetime results presented in this work represents the dependence of the lifetime on the analysis window chosen (see section 4.4.6). Measurements regarding a possible influence of the bunching amplitude, the electron cooler current or the ion current on the lifetime have been performed (see section 4.4.7) and no indication of such dependencies was found. However, due to the poor statistics of the systematics measurements, no realistic estimate of an upper bound on the systematic uncertainty due to these effects could be estimated.

4.5.3 Extraction of the g-factor

As described in section 2.2.2, from the measured transition energy and lifetime of the HFS state one can extract the g-factor of the bound 1s electron for hydrogen-like bismuth and the g-factor of the bound 2s electron for lithium like bismuth.

Hydrogen-like bismuth

The transition probability between the ground state hyperfine states of $^{209}Bi^{82+}$, including the first order QED and nuclear corrections, can be written as [Sha98, BLP+00]:

$$\frac{1}{\tau} = \Gamma_{F' \to F} = \frac{\alpha}{3\hbar} \frac{\Delta E_{\mathrm{HFS}}^3}{(m_e c^2)^2} \frac{I}{2I+1} \left[g^{(\mathrm{e})} - g_I^{(\mathrm{n})} \frac{m_e}{m_p} \right]^2 , \tag{4.37}$$

τ is determined within this work to be $\tau_{\text{H-like}} = (398.5 \pm 1.6_{\text{stat.}} \pm 0.9_{\text{sys.}})$ μs, ΔE is the transition energy extracted from the same data sets, given in [UAD+15] to be $\Delta E_{\mathrm{HFS}}^{\mathrm{H,exp}} = (5085.06 \pm 0.11)$ meV, I is the nuclear spin (for bismuth $I = 9/2$), g_e is the bound-electron g-factor and g_I is the nuclear g-factor. The last term can be written as [Dem05]:

$$g_I \cdot \frac{m_e}{m_p} = \frac{m_e}{m_p \cdot I} \cdot \frac{\mu_{\mathrm{Bi}}}{\mu_0} \tag{4.38}$$

The magnetic moment was determined in [Rag89] to be

$$\mu_{\mathrm{Bi}} = (4.1106 \pm 0.0002) \cdot \ \mu_0 \tag{4.39}$$

Leading to an experimentally determined g_e-factor for the 1s electron in hydrogen-like bismuth of

$$\boxed{g_e^{\mathrm{H,exp}} = 1.7316 \pm 0.0035_{\text{stat.}} \pm 0.0020_{\text{sys.}},} \tag{4.40}$$

in good agreement to the theoretical calculation done in [MOS+04] which yields

$$g_e^{\mathrm{H,theo}} = 1.731014 \pm 0.000001 \tag{4.41}$$

Lithium-like bismuth

In section 2.2.2 it is discussed, that equation 4.37 is applicable for lithium-like bismuth as well. With the above considerations and the preliminary value of the experimentally determined transition energy $\Delta E_{\mathrm{HFS}}^{\mathrm{Li,exp}} = (797.647 \pm 0.026)$ meV from the same beam time [Ull15a], as well as the lifetime presented in this work as $\tau_{\text{Li-like}} = (83.3 \pm 1.0_{\text{stat.}} \pm$

$0.9_{\text{sys.}}$) ms, the experimentally determined g_e-factor for the 2s electron in lithium-like bismuth is found to be:

$$\boxed{g_e^{\text{Li,exp}} = 1.9277 \pm 0.0116_{\text{stat.}} \pm 0.0104_{\text{sys.}}} \tag{4.42}$$

in good agreement to the theoretical value determined from [MSQ08] as described in section 2.2.2:

$$g_e^{\text{Li,theo}} = 1.934739 \pm 0.000003. \tag{4.43}$$

CHAPTER 5

ADAPTION FOR XUV LASER SPECTROSCOPY

The detection principle with a movable mirror which can be moved in and out of the ion beam at a storage ring has been proven to be very successful. With such a system it is possible to collect forward-emitted photons very efficiently and make maximum use of the Doppler shift and the Lorentz boost. Due to this success the basic principle is adapted for laser spectroscopy in the extreme ultra-violet (XUV) region.

5.1 Motivation

Highly charged ions with helium, lithium and beryllium configuration are ideal candidates to investigate effects of QED, relativity and correlation. The latter describes the inter-electron interaction within an atom. The energy level of an atom are influenced by the correlation of the electrons, e.g. due to their Coulomb interaction. For instance fine-structure transition between $^3P_0$ and $^3P_1$ in beryllium-like krypton as shown in fig. 5.1, is expected to be dominated by correlation and relativity effects but is almost unaffected by QED corrections [WKS$^+$11]. The experiment E104 at GSI aims to study this transition. As the $^3P_0$ state cannot decay directly to the ground state, but only through a combined M1E1 transition via the higher lying $^3P_1$ state, the lifetime of the $^3P_0$ state is almost

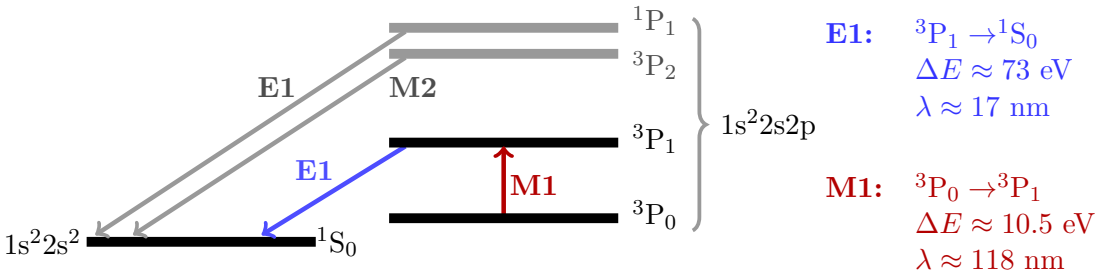

Figure 5.1: Level scheme (not to scale) of the first excited states in beryllium-like krypton after [WKS+11].

infinite ($\mathcal{O}(10^7)$ s). It is expected, that during the production of the Be-like krypton about 10 % of the ions remain in this metastable state. The ions are subsequently stored at a velocity of $\beta = 0.69$ in the ESR. To determine the fine-structure splitting, a laser beam with the wavelength of ca. 276 nm is overlapped anti-collinearly with the ion beam, resulting in a wavelength of ca. 118 nm in the ions rest frame. When the laser hits the resonance, the ion is excited to the $^3P_1$ state from which it immediately decays to the $^1S_0$ ground state, emitting a 17 nm photon. Due to the Doppler effect the mainly forward emitted photons are shifted to even smaller wavelength of < 10 nm, deep in the XUV region.

5.2 Modified detection system

For the LIBELLE experiment the mirror was a parabolically formed oxygen free, high conductivity copper (OFHC) body with high (> 95 %) reflectivity for optical photons and optimal focal features to reflect the emitted fluorescence photons into the direction of the photomultiplier. The ions are able to pass the mirror through a slit with a width of 30 mm according to about 3σ of the ion beam diameter.

For the XUV region the copper mirror was exchanged by a plane stainless steel plate. The slit size was left unchanged, since the beam properties are expected to be similar to the LIBELLE beam-times.

The new concept is, that the high energetic XUV fluorescence photons create low energy secondary electrons on the photo-cathode which are guided electro-magnetically towards a detector. The wavelength of the fluorescence photons is $\lambda_0 \approx 17$ nm, which corresponds to an energy of $E_0 \approx 73$ eV. In the laboratory frame the energy is Doppler shifted

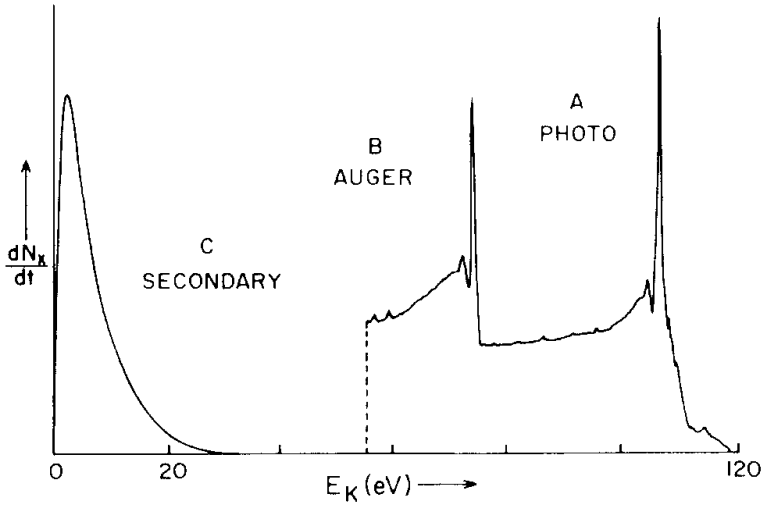

Figure 5.2: A typically x-ray-excited photo-emission spectrum. Picture taken from [HSA77].

to $E \approx 170$ eV in forward direction. Figure 5.2 displays a typical spectrum of the electron energies created by soft x-rays from a metal surface. Up to 90 % of the emitted electrons are created by secondary processes with kinetic energies in the few eV range. Only a small fraction of direct photoelectrons or Auger electrons are observed at higher energies. The design of the XUV system is therefore optimized for the detection of the low energetic secondary electrons. The former PMT is exchanged by a micro channel plate (MCP) in Chevron configuration to serve as an electron detector [Roe15]. It is situated concentrically to the mounting flange. The distance between front plate and flange is approx. 12 cm. All distances can be found in detail in the technical drawing in appendix A.4

The design and the realization of the adapted detector system was done in Münster and will be presented in the following.

The new "mirror" is only used as electron source with no special design requirements regarding the exact shape as for the parabolic copper mirror. Here only the orientation angle between photo-cathode plate and ion beam direction was chosen as a compromise between a maximum effective area (cathode plate perpendicular to the ion beam) and a convenient orientation to emit electrons preferred in the direction of the detector (cathode plate facing the detector). The remaining guidance is done via an electrode system and an applied magnetic field.

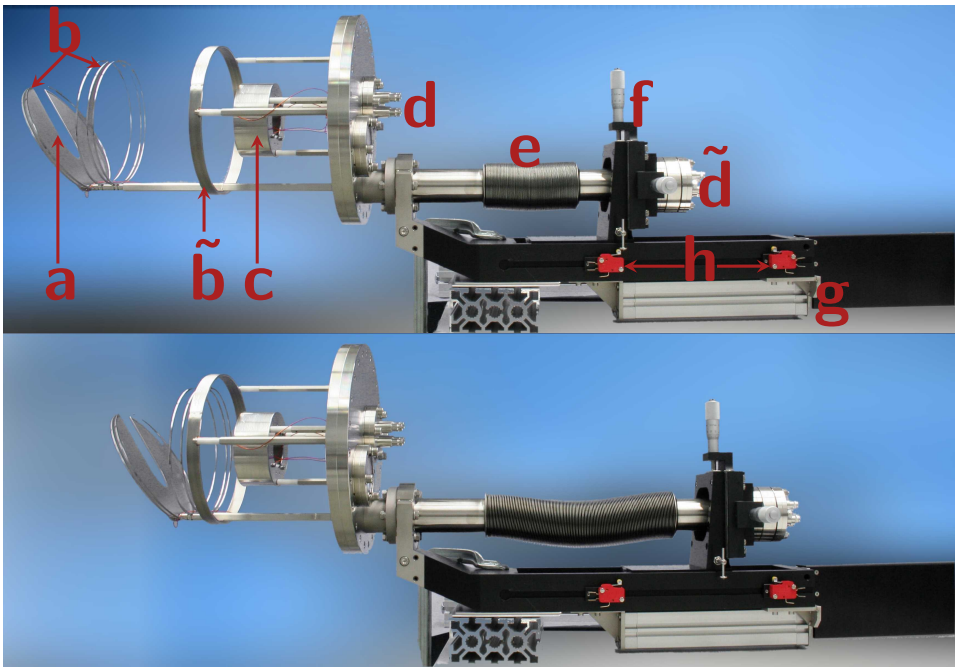

Figure 5.3: Completely mounted, movable detection system fully extended (top) and contracted (bottom). The photo-cathode (a) as well as four of the focus electrodes (b) are movable. The largest and heaviest electrode ($\tilde{b}$) and the MCP detector (c) are mounted directly on the flange. For voltage supply two electrical feed-throughs are used, one for the MCP (d) and one for the electrodes ($\tilde{d}$). The linear feed-through (e) can be adjusted via micro-meter screws (f) and will be driven by a pressured air motor (g). The movement is limited by two end switches (h).

One important design aspect is the weight, though. A problem of the old movable mirror system was the high weight of the copper mirror. Since it was mounted on a rather long linear feed-through the mirror tended to vibrate being moved in or out of the beam position causing losses of stored ions. The effect was minimized by appropriate greasing of the feed-through, and a counter weight. Therefore the new system was planned to be as light-weighted as possible.

To guide the electrons reliably from the photo-cathode to the detector it is recommendable to begin the guidance as close to the cathode plate surface as possible. The electrodes should not intrude into the ESR beam-line and disturb the ion beam, though. Therefore the electrode system is partially connected to the linear feed-through and can be moved in and out the beam line as well (cf. fig 5.3). For this reason the system is made out of thin electrodes to contribute little to the weight. The rest of the detection system, which is a further electrode and the MCP itself, are mounted directly onto a CF200 flange.

5.2.1 Electrode configuration

The electrode system has to focus the electrons onto the detector. For this purpose an Einzel lens like geometry was the basic idea. One has to compromise between an ideal Einzel lens and the light weight. The electrodes within an ideal Einzel lens have a diameter which is roughly of the same size as their thickness to influence charged particles adequately. The electrodes in this setup are optimized regarding their mass and the Einzel lens character is only vaguely recognizable. Due to the low energy of the electrons it is still sufficient to steer the electrons in the right direction, as is verified by simulations using the SimIon 8 software package [Sim15]. The electrode system contains a large electrode mounted directly at the flange (fig. 5.3 $\tilde{\text{b}}$) called focus electrode, three movable thin electrodes directly following each other (fig. 5.3 b) called Einzel electrodes 1-3 (fig. 5.3 b), a further thin electrode in front of the photo-cathode called cathode electrode (fig. 5.3 b) and the photo-cathode itself (fig. 5.3 a). Especially electrons starting from the outer regions of the plate are influenced by the thin electrodes significantly.
Which voltage settings are most efficient to collect the electrons on the detector is discussed in section 5.3.

5.2.2 Magnetic guidance

A sheer electrostatic setup can be designed to guide the electrons onto the detector. However, since the electrons have a low kinetic energy determined by the potential of the cathode plate (typically around 50 eV) they are strongly influenced by the earth's magnetic field or stray fields as they will be present at the intended location at the ESR. For this reason an external magnet coil was introduced to overrule those fields. Beyond this purpose the magnetic field of the coil can also be used as additional guidance for the electrons. Due to their low mass and their low kinetic energy the electrons follow the magnetic field lines on small cyclotron radii r_{cyc} and the magnetic guidance is the dominant process. The cyclotron radius can be calculated with:

$$r_{\text{cyc}} = \frac{m_e v_\perp}{qB} \tag{5.1}$$

With the velocity of the electron $v_\perp$ perpendicular to the magnetic field B. Since the secondary electrons have only a few eV kinetic energy when they leave the photo-cathode

their kinetic energy is dominated by the acceleration potential applied at the cathode plate U and is of the order $\mathcal{O}(50\text{ eV})$. The velocity $v = v_\perp + v_\parallel$ of the electrons is given by

$$v = \sqrt{\frac{2qU}{m_e}} \tag{5.2}$$

leading to a cyclotron radius of maximally a few millimeter in the used magnetic field up to 2.5 mT.

As guiding magnet two coils are placed concentrically around the flange containing the MCP. The coils are 20 cm apart from each other with the MCP about 4 cm of center as shown in fig. 5.4. The field strength at the MCP is of the order of 2 mT and thus

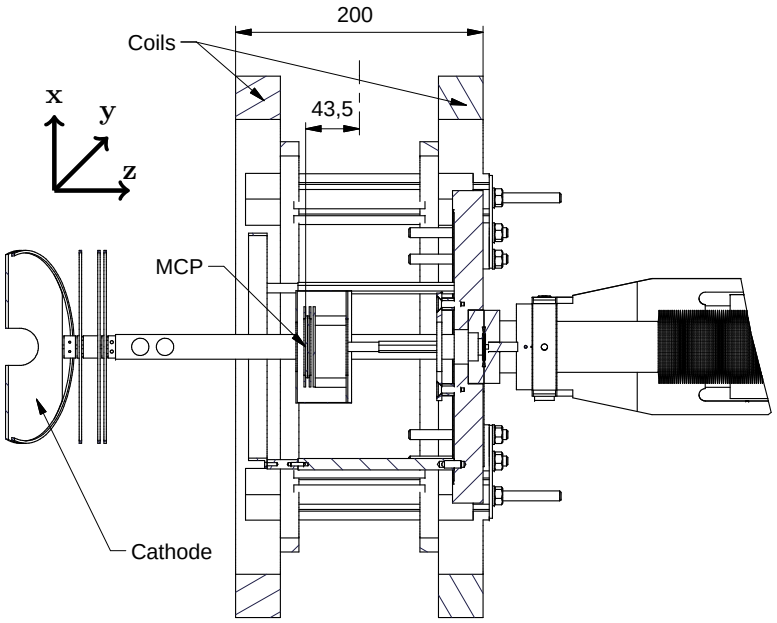

Figure 5.4: CAD drawing by H.-W. Ortjohann with the MCP orientation in respect to the magnet coils. The position of the left coil can not be shifted further towards the photo-cathode, due to the beam line of the ESR. The detector lies concentrically within the coils and is 43.5 mm off-center along the y-axis.

weak enough to not disturb the MCP which can be operated in axial magnetic fields up to 1 T. To have the magnetic field homogeneous at the MCP it would be ideal to have the coils in Helmholtz configuration. The experimental situation at the ESR does not allow this and the coil distance has to be shorter than the coils radius as required for a Helmholtz configuration. The deviation does not hinder the intended operation, actually

a non-Helmholtz configuration might be even more efficient as it will be shown later. Since the introduced magnetic field takes over the dominant part in steering the electrons to the MCP the electrode system becomes less important. While it was mandatory for pure electrostatic steering that the electrons have low kinetic energy, it is less important for the magnetic guidance. Hence an initial electric acceleration of the electrons was considered and is realized by applying a negative electric potential to the cathode electrode. With this the overall time resolution of the complete detector setup can be improved since the electrons time of flight distribution becomes narrower. The actual impact has been investigated via simulations discussed in section 5.3. Along with the higher kinetic energy of the electrons, the applied voltages at the ring electrodes have to be higher in order to be influential.

5.2.3 Micro-Channel-Plate detector

As detector the micro-channel-plate (MCP) detector DET40 from Roentdek with an active area diameter of 40 mm is used. It contains two channel plates aligned in Chevron configuration with an anode behind. To improve the gain factor and reduce electron feedback a shim ring is placed between front and back plate ([Roe15]) as seen in fig. 5.5.

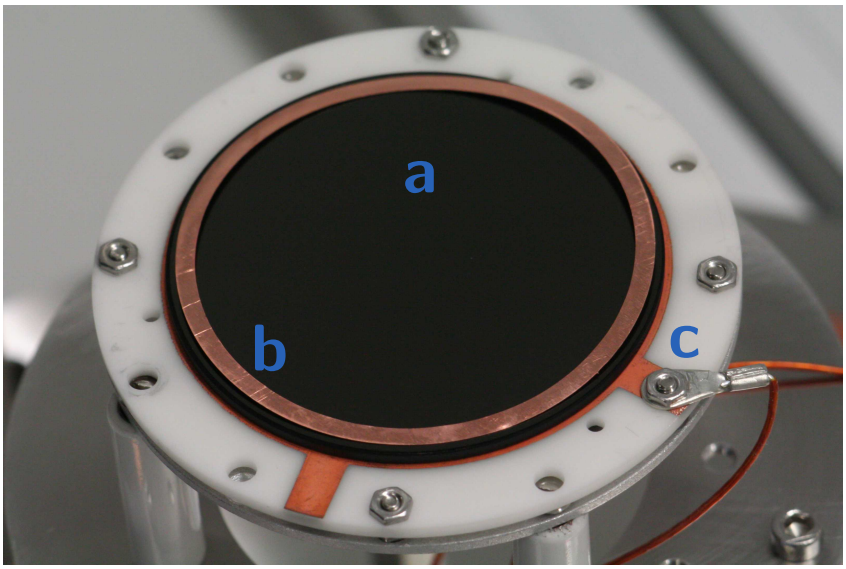

Figure 5.5: The MCP during assembly. First micro-channel plate (a) and shim ring (b) are placed. Connectors (c) may attract electrons and will be shielded in the completed setup (see fig. 5.6 (b)).

For electron detection the following voltages are suggested by the company:

MCP front:	200 V
MCP back:	2500 V
Anode:	2800 V

MCP back and anode are connected to the same high voltage supply via a voltage divider. The voltage difference can be set in discrete steps via a jumper in the divider, 300 V is the maximum. The three parts of the detector are connected with capton isolated wires to an electrical feed-through. Since electrons may be influenced by the voltage connections at the MC-plates a grounded shielding is put around the detector (fig. 5.6, (b)). The

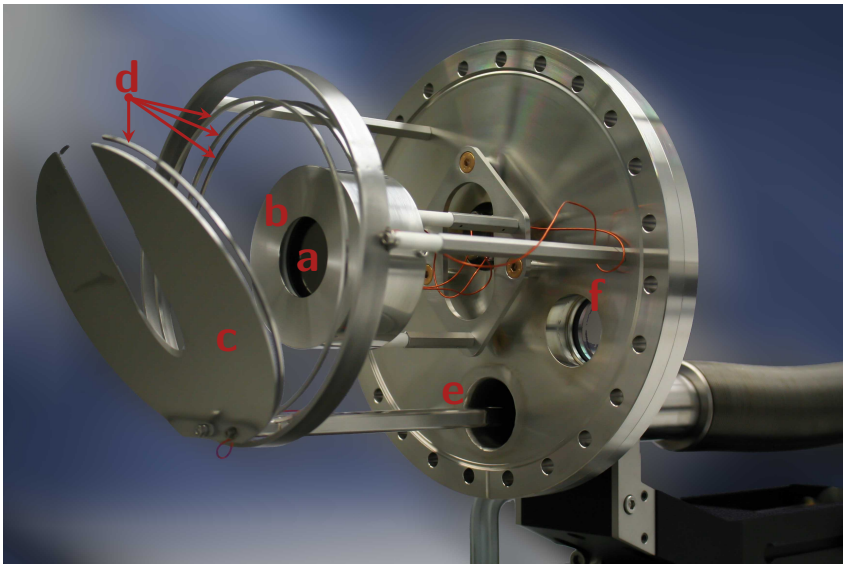

Figure 5.6: Completely mounted detector flange with the MCP (a) shielded by a ground electrode (b). The photo-cathode (c) and most of the focus electrodes (d) are connected to the linear feed-through (e). For adjustments a view port (f) is present. The system is shown in the contracted state.

wires are as short as possible to minimize noise pickup. at the electrical feed-through the signal is decoupled via an RC-coupler as shown in figure 5.7. In addition an adjustable 250 Ω resistor is introduced to optimize the signal shape. After the RC-coupler the signal is sent to a fast amplifier for further processing.

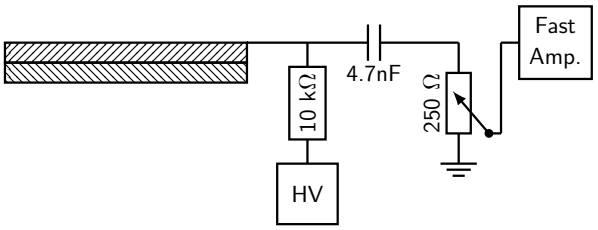

Figure 5.7: Wiring scheme after [Roe15] to decouple the signals of anode, MCP back and MCP front. At each HV connection a 10 kΩ resistor is inserted to limit the currents. The signal is decoupled via a 4.7 nF capacity and is sent to a fast amplifier. In-between an adjustable resistor up to 250 Ω can be used to minimize oscillations on the signal.

5.3 Simulation tool SimIon

To find the optimal settings for each electrode voltage and the magnetic field strength, simulations have been performed with the simulation tool SimIon 8.1 [Sim15]. The setup as described above is implemented as a SimIon geometry for which the electrostatic fields comply with boundary value problem solutions of the Laplace equation. The equation is solved via a finite difference method. The overall solution is a superposition of individual electrode contributions, which enables for fast adjustments of electrode voltages once the electric field shape is calculated. For particle trajectory determination a fourth-order Runge-Kutta integration algorithm is used.

The magnetic field created by solenoids or wires in general is obtained analytically via the Biot-Savart equation.

A user program to control the simulations is written in the programming language LUA. Besides the definition of the coils, adjustments of the electrodes can be programmed here. For this purpose loops can be implemented to carry out systematic variations of the applied voltages.

Termination conditions for the particle trajectories can be defined to distinguish between particles which are lost hitting an electrode and those which can be counted as detected by hitting the electrode defined as detector.

The LUA code loads a file for particle definition as well. In this file properties of the particles and their starting conditions can be set. In this case electrons are distributed homogeneously on a disc tilted by 30° to the beam direction, with a random starting vector isotropically distributed within 2π (compare fig. 5.8) and provided with 3 eV

kinetic energy. Since the cathode plate has a slit for the ions to pass through, electrons created in this area are discarded.

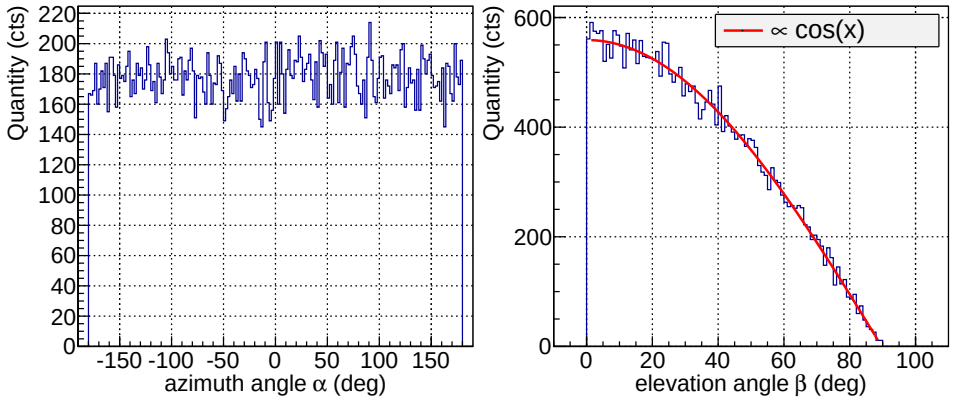

Figure 5.8: The starting vector of particles is defined via an azimuth angle $\alpha \in [-180 : 180]$ and an elevation angle $\beta \in [0 : 90]$. α is distributed homogeneously in its interval as shown in the left figure, the distribution of β is proportional to a cosine $\frac{dN}{d\beta} \sim \cos\beta$ as shown in the right figure. Together an isotropic 2π distribution is obtained.

5.4 First commissioning and simulations

For first commissioning the detector setup is put in a vacuum chamber large enough to contain the fully extended system. With the chamber a vacuum of at least $2 \cdot 10^{-6}$ mbar should be reachable to operate the MCP safely.

At first operation the MCP should be in vacuum for 24 hours and the supply voltages should be ramped up slowly (100 V every few minutes) to condition the detector and avoid electric discharges. At operation voltage a signal can be picked up as shown in fig. 5.7 from each channel. As an example a single photo-electron event is depict in fig. 5.9. The expected signal height can be estimated by Ohm's law:

$$U = R \cdot I \,. \tag{5.3}$$

With the resistance of the signal processing hardware, which is 50 Ω and the current I which corresponds to the amount of charge carriers per time $\frac{dQ}{dt}$ it yields:

$$U = R \cdot \frac{dQ}{dt}$$

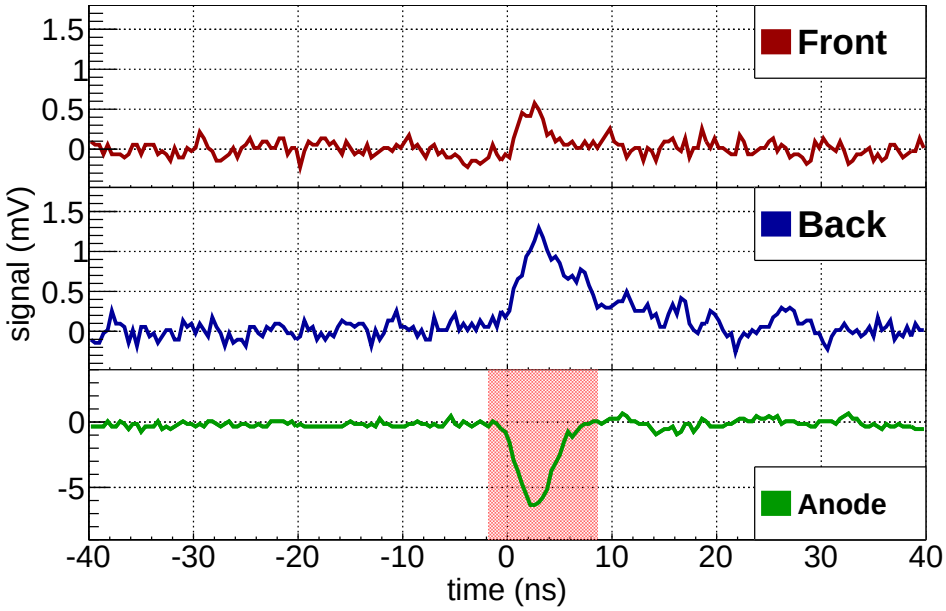

Figure 5.9: Signals of the MCP. Channel 1 is the front plate (top/red), channel 2 the back plate (middle/blue) and channel 3 the anode (bottom/green). The signal is induced by a single photo-electron event and was recorded with a voltage difference between front and back plate of the detector of 2000 V. The relevant signal is picked up at the anode. The signals coming from the micro-channel plates themselves can be used to check the proper functioning of the detector. The integrated signal over the range indicated by the red shaded area yields $|A| = 64.1$ mV·ns and leads to a gain factor of $0.8 \cdot 10^7$ (cf. eq. 5.3-5.6).

The total amount of charge carriers $Q = \int dQ$ is determined through the gain of the MCP and is given by the manufacturer to be 10^7 at 2400 V voltage difference between front and back plate of the detector. Integrating the signal over time yields:

$$\int_0^\infty U\,dt = \int_0^\infty R \cdot \frac{dQ}{dt} dt = R \cdot \int_0^\infty dQ = RQ \tag{5.4}$$

$$= 50[\Omega] \cdot 10^7[\mathrm{e}]$$

$$= 50 \frac{[\mathrm{V}]}{[\mathrm{A}]} \cdot 10^7[\mathrm{e}]$$

$$= \frac{50}{6.2415 \cdot 10^{18}} \frac{[\mathrm{V}]}{[\mathrm{e/s}]} \cdot 10^7[\mathrm{e}]$$

$$= 50 \cdot 1.6022 \cdot 10^{-19} \cdot 10^7[\mathrm{V \cdot s}] \tag{5.5}$$

$$\approx 8 \cdot 10^{-11}[\mathrm{Vs}]$$

$$= 80[\mathrm{mV \cdot ns}] \tag{5.6}$$

This matches well with the measured signal shown in fig 5.9 where the signals area is found to be 64.1 mV·ns. In reverse 64.1 mV·ns lead with eq. 5.5 to a gain of $0.8 \cdot 10^7$. Since this value was recorded with ca. 20 % lower potential difference between back and front plate, i.e. 2000 V, it matches well with the value stated by the manufacturer of $1.0 \cdot 10^7$ at 2400 V. Although the gain is not connected linearly to the bias voltage the proper functioning of the MCP can safely be assumed.
For further tests the electrode system was put in operation to be able to detect electrons coming from the photo-cathode. The optimal electrode setting given by the simulations and verified by measurements is given in table 5.1.

Table 5.1: Optimal electrode settings as found in simulations and measurements and used MCP settings. The latter differ slightly from the values recommended by the company.

Electrode settings:

Electrode	Voltage [V]	Electrode	Voltage [V]
Focus electrode	-50	1st electrode	0
3rd electrode	-100	cathode electrode	-50
2nd electrode	-20	photo-cathode	-50

MCP settings:

Part	Voltage [V]
Anode:	2500
Back:	2200
Front:	300

The standard voltages applied at the MCP are slightly different from those given by the company. The front plate is put on a 100 V higher potential to attract electrons stronger. The back plate is 300 V under the proposed value, since higher noise due to micro-discharges occurred with higher voltages. Since the difference between front and back plate defines the gain of a MCP, which is for standard settings reduced to 1900 V the expected gain factor is smaller than stated by the company for 2400 V voltage difference or calculated above. The difference between anode and back plate is fixed via jumper as mentioned earlier.

The magnetic field strength $B(z)$ is a superposition of the magnetic field generated by the individual conductor loops $B_{1,2}(z)$ which is given by [Dem06]:

$$B_{1,2}(z) = \frac{\mu_0 \cdot n \cdot I \cdot r^2}{2\left[(z \pm |d_{1,2}|)^2 + r^2\right]^{3/2}} \tag{5.7}$$

with the amount of turns $n \approx 264$, the coil's radius $r \approx 197.5$ mm and the used current $I = 1.9$ A. μ_0 is the vacuum permeability.
With two coils positioned at a distance d_1 and d_2 from their common center the superimposed field can be written as:

$$B(z) = \frac{\mu_0 n I r^2}{2}\left\{\left[(z + |d_1|)^2 + r^2\right]^{-3/2} + \left[(z - |d_2|)^2 + r^2\right]^{-3/2}\right\} \tag{5.8}$$

For Helmholtz configuration the following must apply:

$$d = |d_1| + |d_2| = r \qquad \text{and} \qquad |d_1| = |d_2|$$

The coils in the given setup are closer together and the MCP is aligned off-center in z direction (cf. fig. 5.4), such that:

$$|d_1| \approx 40 \text{ mm} \qquad \text{and} \qquad |d_2| \approx 120 \text{ mm}.$$

With this the generated field of the two coils at the MCP, i.e. $z = 0$ is calculated to be about 2.5 mT. Analogous the field at the cathode plate which is ca. 0.24 m away can be estimated to be $B(z \approx 0.24) \approx 0.7$ mT. Due to the magnetic field gradient electrons could in principle be reflected magnetically. This is not the case in the given setup, due to the applied voltages, especially the rather high potential of about +300 V applied at the front plate of the detector which attracts the electrons strongly. However, for other configurations this effect may play a roll and has to be taken into considerations.
Since no light source was available with wavelength as short as expected later in the experiment, a 265 nm UV-LED of the type UVTOP260 from Roithner LaserTechnik GmbH was used for first tests with UV photons. Via an additional feed-through the LED can be put into the vacuum chamber to illuminate the photo-cathode plate directly. In this way, it is easier to illuminate the cathode homogeneously than if an optical fiber

had been used to couple light into the setup. The light-source is located next to the MCP oriented towards the cathode plate. The distance is roughly 20 cm $< d <$ 26 cm between photo-cathode and LED. The divergence of the LED light is given to be $\alpha = 7°$ due to the ball lens that is part of the LED package (cf. fig. 5.10). With this information the

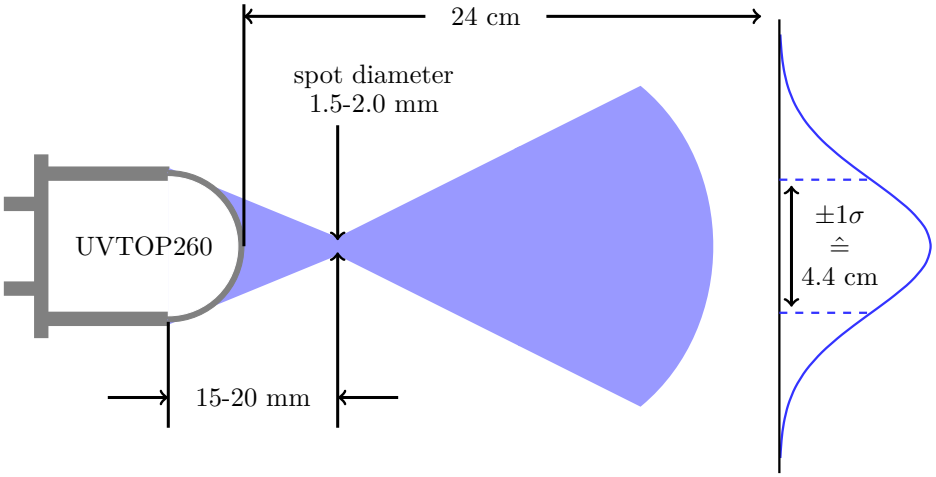

Figure 5.10: Geometry of the used LED [Roi15]. The light cone has an opening angle of 7°. At 24 cm distance a Gaussian profile can be measured with $\sigma = 2.2$ cm (not to scale).

spot size on the cathode plate has a radius r of:

$$r = d \cdot \tan\left(\frac{\alpha}{2}\right) \approx 1.2 - 1.6 \text{ cm}. \tag{5.9}$$

However the scheme in fig. 5.10 suggest that this specification is only true for the vicinity directly in front of the LED. The LED intensity distribution was checked with a photo diode in the appropriate distance of about 24 cm resulting in a Gaussian intensity distribution with $\sigma = 2.2$ cm.

Besides the spot size the location on the cathode plate is important, especially for later comparison with the simulations. Figure 5.11 shows a photograph of the faint LED spot (a), as well as the photo-cathode and electrode structures (b) and a superposition (c) of the two photos to determine the spatial extent of the LED spot on the cathode plate. The corresponding implementation in the simulation code is shown in fig. 5.11 (d). Electrons are created over the whole photo-cathode, but weighted with a Gaussian distribution with $\sigma = 2.2$ cm, centered in the red area. Those electrons with unphysical starting conditions, e.g. inside the slit, are discarded by the LUA code as described before.

A Tektronix arbitrary function generator (Tektronix AFG 3102) drove the LED using

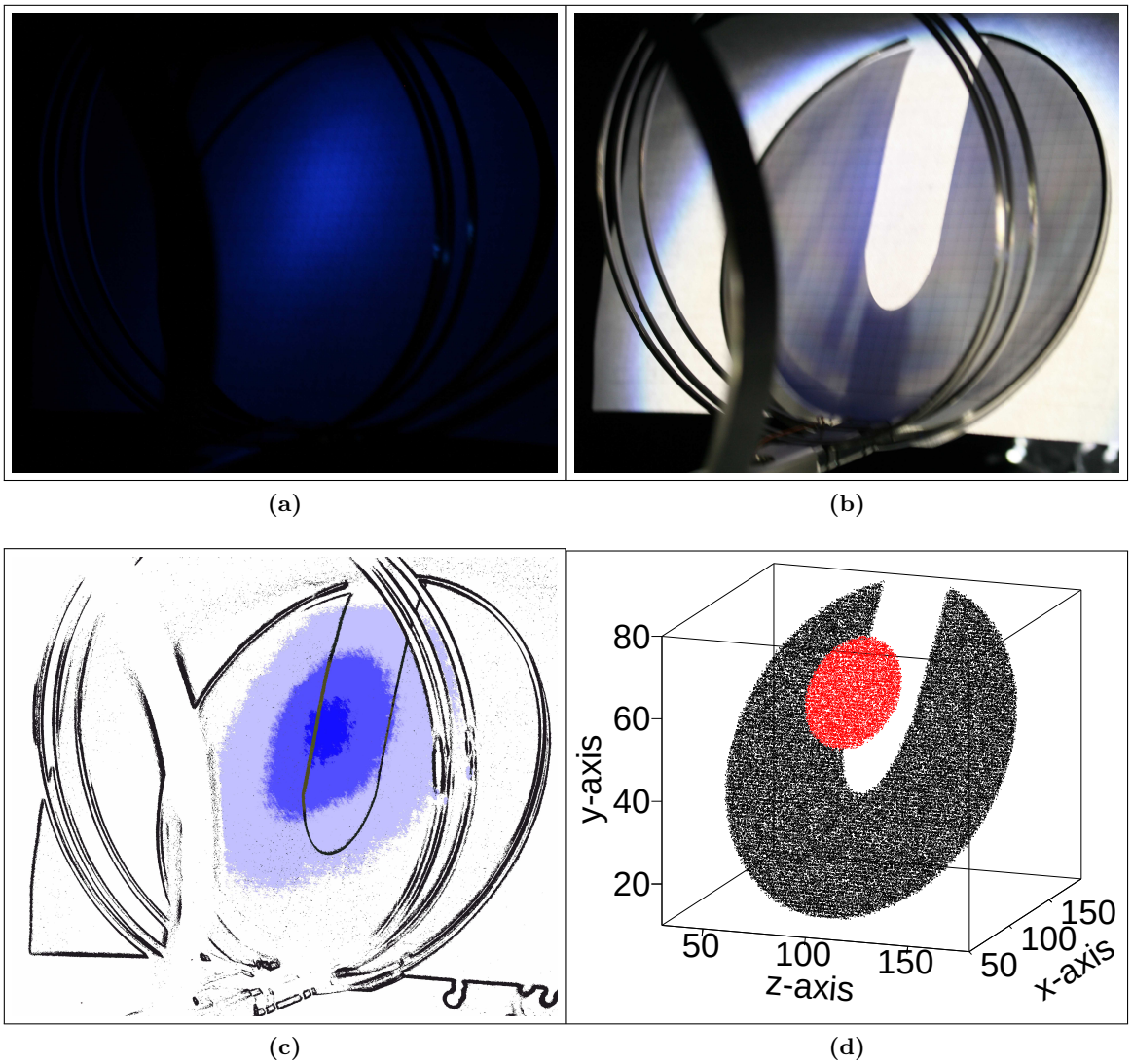

Figure 5.11: For accurate simulations the spot size of the LED in 24 cm distance and its actual location on the photo-cathode surface was investigated. (a) shows the LED spot on the cathode plate. For better orientation a photo was taken with the same settings but illuminated photo-cathode and electrode structure (b). A superposition of (a) and (b) is shown in (c). With this information the spot is implemented in simulations (d) and the starting properties of the electrons are restricted. Electrons are created over the whole photo-cathode, but weighted with a Gaussian distribution with $\sigma = 2.2$ cm, centered in the red area. Electrons with a starting point inside the slit are discarded.

30 ns pulses with an amplitude of 5.5 V and a repetition frequency of 100 kHz. To suppress electronic interference between the current pulses driving the LED and the MCP readout, the leading and trailing edges of the pulses were broadened to 15 ns.

As the amount of photons per second created by the LED is not known and because we are working at a very different wavelength compared to the later experiment, we

cannot extract a statement on the absolute detection efficiency for XUV photons from the measurements.

5.4.1 Magnetic field optimization

Since the magnetic field took over the dominant part of guiding the electrons to the detector, an optimization of the magnetic field is performed first with settings for the electrode voltages taken from simulation. The coil design itself is mostly determined by the experimental conditions. For first tests a pair of Helmholtz coils were available meeting those conditions. With these a measurement series was performed with varying current, and thus magnetic field strength versus count rate as visualized in fig. 5.12. The simulated data is plotted with triangles, experimental data with diamonds. The

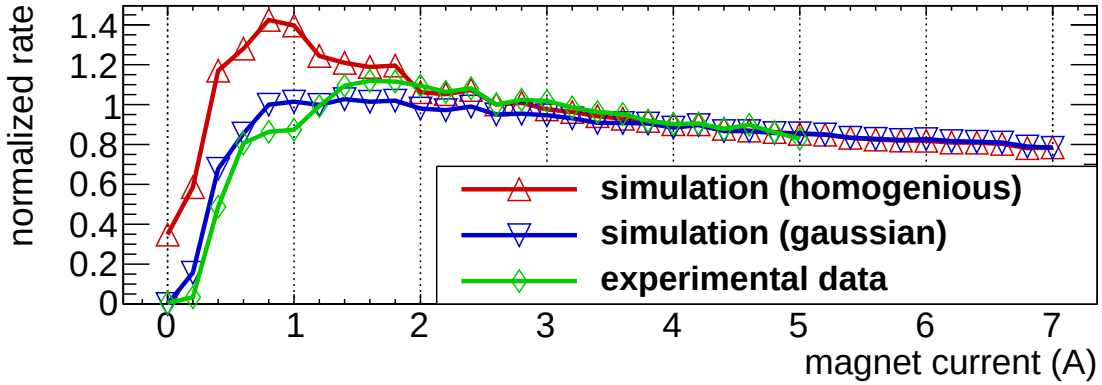

Figure 5.12: Normalized electron count rate versus magnet current and thus magnetic field strength. Green diamonds are experimental data points. Triangles represent simulations. Since the LED's spot has a Gaussian intensity distribution the simulation with electrons weighted uniformly (red, up-pointing triangles) does not agree as well with the experimental data as the simulation with electrons weighted with a Gaussian distribution (blue, down-pointing triangles) as explained in fig. 5.11.

experimental data were recorded as part of the bachelor thesis of F. Trittmaack [Tri15]. Above a current of about 1.5 A all results agree well with each other. For magnet currents below this value the red curve deviates clearly from the others. This is due to the distribution of the electron's starting points. The up-pointing triangles represent a simulation were distribution is homogeneous as is expected in the actual storage ring experiments. For the down-pointing triangles the events are weighted with a Gaussian distribution with $\sigma = 2.2$ cm as discussed before (cf. fig. 5.11). This is closer to the test setup since the LED's intensity distribution is indeed Gaussian. Taking this into account simulations agree well with the experimental data.

To optimize the given setup regarding the count rate of electrons the coils should be driven with about 1.8 A. In the later experiment the photo-cathode plate will be illuminated by fluorescence photons with a rather homogeneous intensity distribution, therefore the simulation of the whole cathode plate will be more appropriate and thus a current of 0.8 A is advisable, if the current magnet design is used. The decreasing branch in all data sets is most likely due to phase effects in the cyclotron motion of the electrons along the field lines. To achieve a better focusing a non-Helmholtz symmetry, i.e. a smaller coil-to-coil distance might be better as shown in fig. 5.13 (left column). With the small coil distance shown in fig. 5.13, 1. a), field lines running through the MCP plates cover a larger area on the cathode plate. The radius of the coil could also be reduced to image a larger area of the photo-cathode plate onto the detector as shown in fig. 5.13 (right column). The radius is restricted by the radius of the vacuum chamber. However it is in principle possible to mount a coil inside the vacuum as well, if sufficient cooling is provided or only small currents are applied.

In both cases the angle under which electrons are able to reach the detector and are not magnetically reflected is influenced, since the ratio $\frac{B_{\text{min}}}{B_{\text{max}}}$ changes. If the applied voltages at the electrodes and the detector are sufficiently high to counteract this effect, has to be investigated for the individual setting. The actual design and test of an optimized coil system is subject of further investigations.

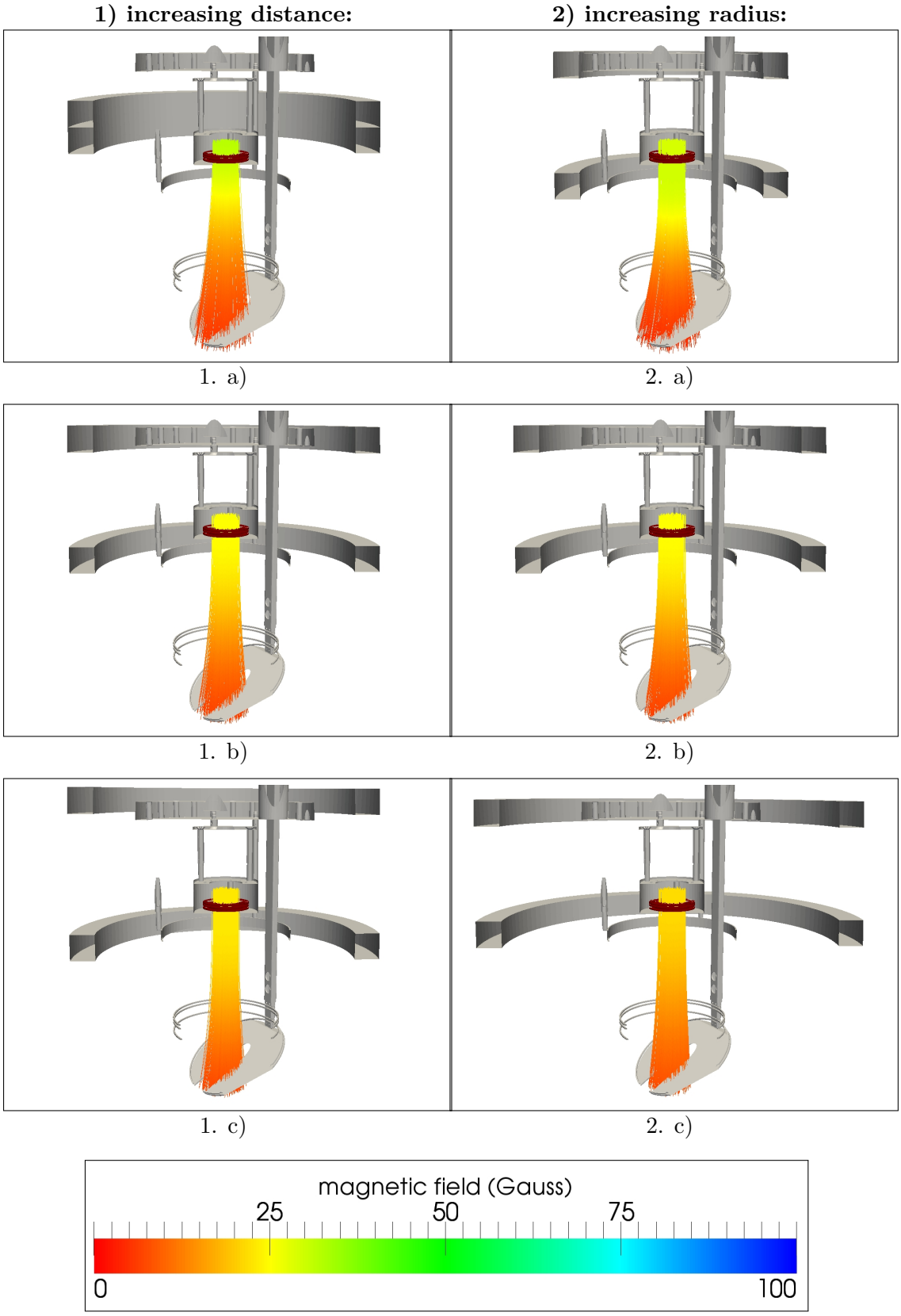

Figure 5.13: Magnetic field lines for different coil distances (left column) and coil radii (right column). The MCP is shown in red.

5.4.2 Photo-cathode potential optimization

Although the electrode settings are less significant in an electro-magnetic guidance, than in a purely electrostatic variant, the applied voltage at the cathode plate is still a critical parameter. Especially with non, or low potentials applied at the photo-cathode the created electrons have insufficient energy to reach the detector. A measurement was performed to investigate the dependence of the count rate on the cathode potential as shown in fig. 5.14. Again a distinction was made in the simulation between

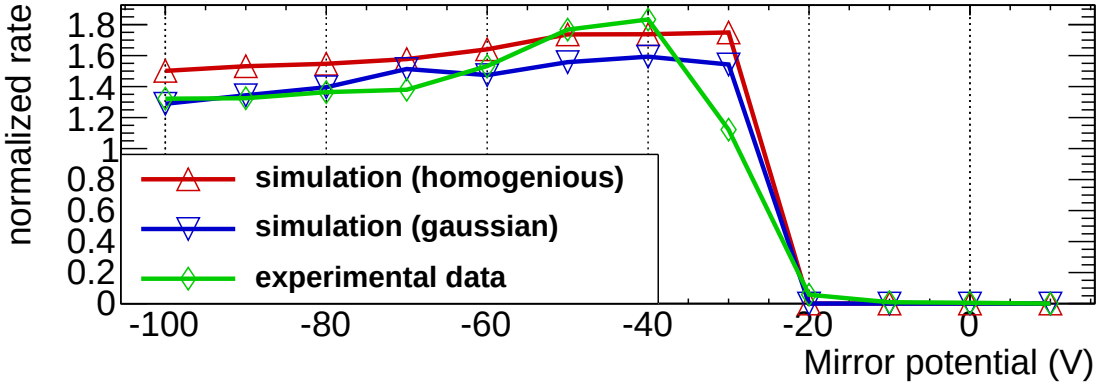

Figure 5.14: Normalized count rate versus applied cathode potential to accelerate the electrons. Green diamonds are experimental data points. Triangles represent simulations. Again it can be distinguished between electrons weighted homogeneously (red, up-pointing triangles) and Gaussian corresponding to the LED spot properties (blue, down-pointing triangles). In this case no big difference is given and all results agree with each other. Especially the minimal acceleration voltage of about -20 V is determined by all data sets.

homogeneously distributed electrons (fig. 5.14, red, up-pointing triangles) and electrons weighted with a Gaussian distribution centered in the LED spot (fig. 5.14, blue, down-pointing triangles). In this case no significant difference can be observed. Both simulated data sets agree well with the experimental data (fig. 5.14, green diamonds). In all three cases the electrons need to be accelerated with at least -20 V applied at the cathode plate to be detected. For higher voltages the count rate shows a slight decline. The optimal setting is found at -40 V acceleration potential. An even higher acceleration voltage has nevertheless an influence on the time of flight of the electrons as discussed in the following section. For details regarding the optimization of the remaining electrode voltages see the bachelor thesis of F. Trittmaack [Tri15].

Given the good agreement between the results of test measurements with the XUV setup and the results obtained with the SimIon model, we can use the simulations

to determine the photo-electron collection efficiency of the setup. For homogeneously distributed illumination of the photo-cathode, as expected in the actual experiment, the collection efficiency is found to be about 53 %. It is expected, that this value can still be improved with an improved magnet coil design.

5.4.3 Time of flight

Another important aspect to be investigated is the time of flight (TOF) of the electrons. For such a measurement the start-point is provided by the pulse from the AFG function generator driving the LED. The end-point is obviously given by the signal produced by electrons reaching the detector. In this way spectra as shown in fig. 5.15 are created, recorded by D. Winzen. To ensure the intended functioning of the whole system measurements were performed with all electrodes on standard settings as given in tab. 5.1 (fig. 5.15, red), while for reference measurements the electrodes were turned off (fig. 5.15, blue shaded). In both cases the coils were supplied with a current of 1.9 A to generate a magnetic field in the center of about 2.3 mT. In both cases the photons coming from

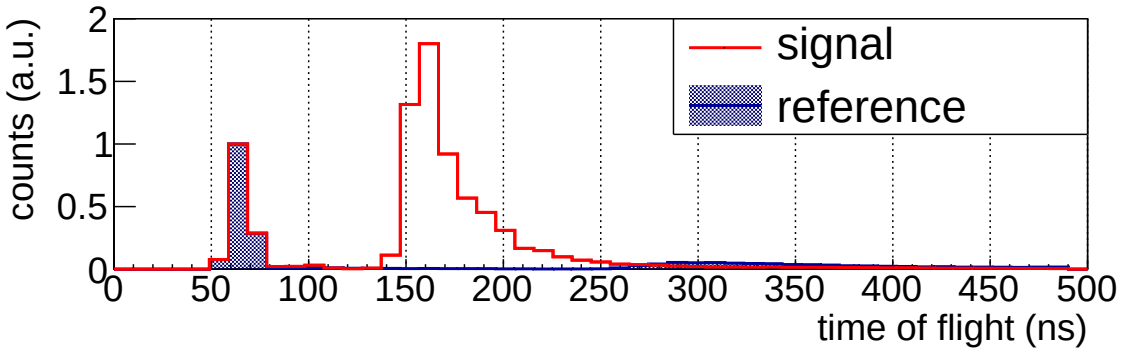

Figure 5.15: Experimental time of flight distribution. The reference data (blue) was taken with LED and magnet turned on, operated at standard settings. All electrodes were switched off. As expected from fig. 5.14 no electrons reach the detector and only the stray light from the LED causes a peak at about 60 ns. Applying the settings as shown in tab. 5.1 the produced electrons are guided to the MCP (red) and give rise to the peak at about 160 ns. Of course the LED peak is present as well and covers the LED-peak from the reference data.

the LED create a peak at about 60 ns. The LED peak in the reference measurement is completely covered by the LED peak in the standard measurement and is therefore shaded for better visibility. The two LED peaks are normalized to one. Since the TOF

starting point is the pulse provided by the AFG, the position of the LED peak contains information on the time needed for signal processing, which is given by:

$$\tau_{\text{total},\gamma} = \tau_{\text{TOF},\gamma} + \underbrace{\tau_{\text{LED}} + \tau_{\text{MCP}} + \tau_{\text{cable}} + \tau_{\text{DAQ}}}_{:= \tau_{\text{delay}}} = 60 \text{ ns} \tag{5.10}$$

τ_{LED} takes into account since the leading edge and half of the width of the pulse used to drive the emission. τ_{TOF} is the actual time of flight value, which is negligible for photons (< 3 ns) and τ_{MCP} is assumed to be in the order of a few nano-seconds as well. The major part is given by τ_{cable} because rather long cables were used from the decoupling of the signal to the electronics and τ_{DAQ} accounting for the time needed by the data acquisition. The absolute times are not relevant, because the position of the LED peak can be used to separate the actual time of flight of the electrons from the delay time introduced by the other components:

$$\tau_{\text{TOF},e^-} = \tau_{\text{total},e^-} - \tau_{\text{delay}} \tag{5.11}$$

With $\tau_{\text{delay}} \approx 60$ ns since $\tau_{\text{TOF},\gamma} \approx 0$.

As already discussed the starting position of the electrons on the cathode surface is substantial for the trajectories of the electrons and thus for the TOF. The distance for the electrons to travel is larger for electrons starting from the lower half of the cathode plate than for those starting from the upper half (cf. 5.16). More important the influence of the electric and magnetic fields is different for different starting positions and will therefore affect the time of flight. Taking those aspects into account the measured TOF spectra can be compared to simulations. In fig. 5.17 the simulated TOF distribution is shown

Table 5.2: Fitparameter of the individual Gaussian indicated as dashed line in fig. 5.17 from left to right.

#	Amplitude	Center	Sigma
1	55.2	92.3	11.7
2	15.1	118.4	14.0
3	12.1	144.5	34.0

in green, the experimental data is shown in red. The two data sets are normalized to the maximum peak height. Each electron event in the simulated data set is convoluted with

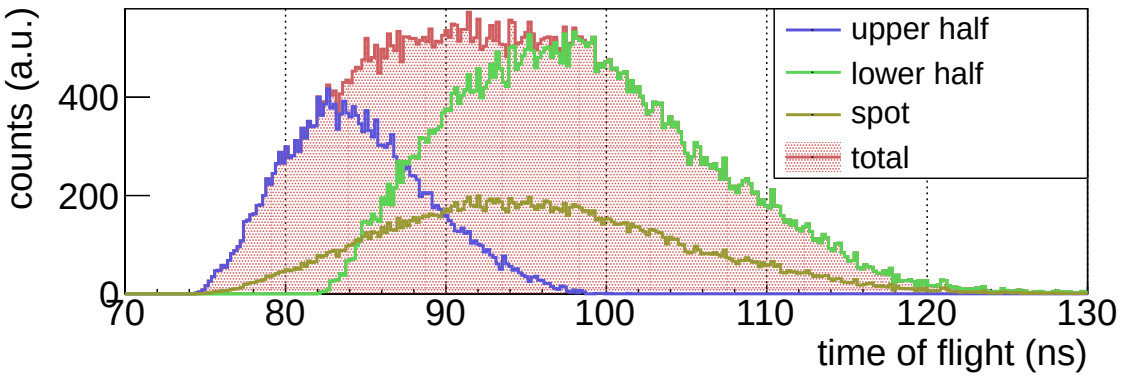

Figure 5.16: The electron t.o.f is influenced by the electromagnetic fields, depending on the starting conditions of the electrons. Electrons coming from the upper half (blue) are significantly earlier at the detector than those coming from the lower half (green), or the spot, corresponding to the center of illumination (yellow) as shown in fig. 5.11(d). This is expected since the electrons starting from the upper half have a shorter distance to the MCP.

a Gaussian distribution dependent on its origin as discussed before, to account for the experimental situation and make it comparable to the measured data. The experimental data is in addition shifted by the photon peak position as seen in fig. 5.15. Like this the data sets match well, especially regarding the actual time of flight. The remaining difference in shape is due to background events from electrons produced on other surfaces which are not included in the simulations.

The experimental data was fitted with three superimposed Gaussian distributions (dashed line in fig. 5.17). While the second and third account for electrons coming from other surfaces within the setup, the first Gaussian accounts for the electrons starting from the photo-cathode. Therefore the width of the first Gaussian defines the time resolution of the detector setup to be $\sigma = 11.7$ ns, at a cathode potential of -50 V.

In section 5.4.2 the importance of the cathode potential was already discussed, in figure 5.18 the influence on the TOF is visualized. As expected the time of flight as well as the width of the distribution is reduced with higher negative acceleration voltage applied to the photo-cathode plate. For the actual experiment a compromise needs to be found between optimum count rate, as deduced from fig. 5.14, and time resolution of the detector determined via fig. 5.18.

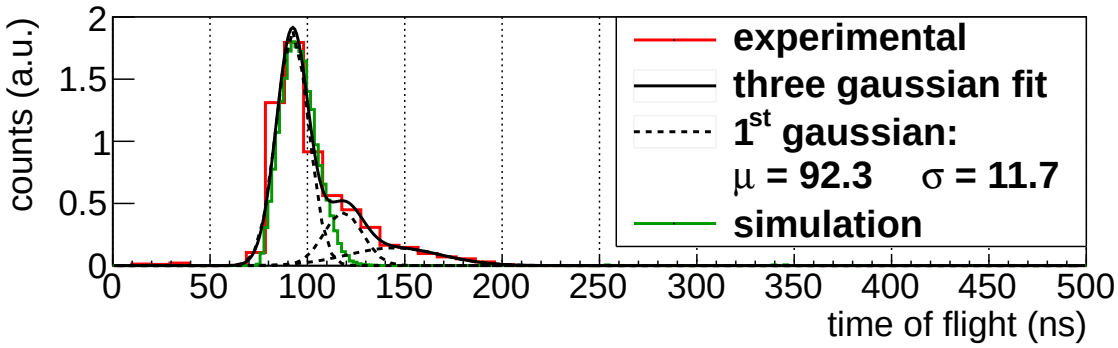

Figure 5.17: Comparison between simulated (green) and measured (red) time of flight distribution. The data sets are normalized to each other for better comparability. The measured TOF is shifted by the time of flight of the LED peak to account for the time consumed by cabling, DAQ etc. The data was fitted with three Gaussians to obtain information about the mean t.o.f. and the time resolution. The simulated data weight each event with a Gaussian distribution. Therefore the relevant electrons come from the spot shown as red area in fig 5.11(d) which represents 1σ of the LED intensity to meet the given conditions in the setup.

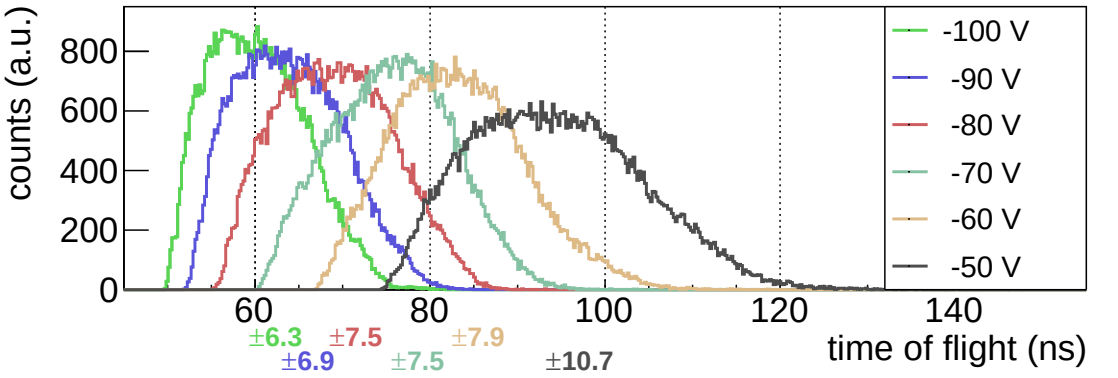

Figure 5.18: Via the applied voltage at the photo-cathode plate the properties of the detection system changes since it defines the kinetic energy of the electrons. To investigate the dependence of the t.o.f distribution on the potential applied at the cathode simulations were performed. With higher voltages the TOF distribution is narrower and shifted to shorter flight times. The TOF distributions were fitted via a Gaussian to determine its 1σ width. The outcome is shown in corresponding color code at the x-axis.

CHAPTER 6

CONCLUSION AND OUTLOOK

Conclusion

While the energies of the HFS transition in hydrogen- and lithium-like bismuth were determined in the PhD theses of R. Jöhren, M. Lochmann and J. Ullmann for data recorded during the LIBELLE beam times in 2011 and 2014, respectively, in this work the analysis of the data sets regarding the lifetime of the HFS states is presented. The lifetime of $^{209}Bi^{82+}$was already investigated before [Win99], whereas the lifetime the of $^{209}Bi^{80+}$was not experimentally determined before. The LIBELLE experiment was able to measure both lifetimes yielding:

$$\tau_{\text{H-like, exp}} = (398.5 \pm 1.6_{\text{stat.}} \pm 0.9_{\text{sys.}})\ \mu\text{s}$$
$$\tau_{\text{Li-like,exp}} = (83.3 \pm 1.0_{\text{stat.}} \pm 0.9_{\text{sys.}})\ \text{ms}$$

The determined lifetimes agree well with theoretical predictions:

$$\tau_{\text{H-like, theo}} = (399.01 \pm 0.19)\ \mu\text{s}\ \text{[Sha98]}$$
$$\tau_{\text{Li-like,theo}} = (82.85 \pm 0.61)\ \text{ms}\ \text{(cf. sec. 2.2.2)}$$

Possible systematic effects on the lifetime for both species were examined, which were only discussed briefly in previous works. For this purpose systematic measurements were

performed, albeit with a low statistics for lifetime determination.

Together with the results regarding the transition energies determined by the 2014 beam time of the LIBELLE experiment the bound g-factors of the 1s and the 2s electrons in hydrogen- and lithium-like bismuth were determined, respectively:

$$\boxed{\begin{aligned} g_e^{\mathrm{H,exp}} &= 1.7316 \pm 0.0035_{\mathrm{stat.}} \pm 0.0020_{\mathrm{sys.}} \\ g_e^{\mathrm{Li,exp}} &= 1.9277 \pm 0.0116_{\mathrm{stat.}} \pm 0.0104_{\mathrm{sys.}} \end{aligned}}$$

The experimental value for the 1s electron in hydrogen-like bismuth is in good agreement with the theoretical predictions by Moskovkin et al. [MOS+04]

$$g_e^{\mathrm{H,theo}} = 1.731014 \pm 0.000001$$

The 2s electron in lithium-like bismuth is as well in good agreement with the theoretical prediction by Moskovkin and co-worker [MSQ08]

$$g_e^{\mathrm{Li,theo}} = 1.934739 \pm 0.000003$$

For the measurements with lithium-like bismuth, the introduction of a novel, movable mirror system was mandatory. The success of this system inspired a further development for the extreme ultra-violet wavelength region. The principle changed from a direct photon detection to the detection of secondary electrons which are produced by XUV fluorescence light by the photo-effect on a photo-cathode. A suitable detection system employing electromagnetic guidance of the secondary electrons to an MCP detector in vacuum was designed and built in Münster and first commissioning tests were performed. For the design process the elementary detector structure was modeled using the electromagnetic simulation tool SimIon. After construction of the setup in the mechanical workshop of the institute, test measurements were performed and compared to the simulations. All measurements agree well with the performed simulations suggesting a good understanding of the detector and thus reliable simulations. Therefore it can be safely assumed that the extracted electron collection efficiency of about 53 % is realistic. The performed measurements in comparison with simulations suggest that the used magnet configuration can be improved. A more inhomogeneous magnetic field at the

mirror could improve the focusing properties to direct more field lines directly onto the MCP. For this reason for instance a smaller coil diameter might be advantageous, since the magnetic flux tube at the MCP becomes narrower.

Outlook

With the expected accuracy of $< 10^{-4}$ for the transition wavelength obtained from the 2014 beam time of the LIBELLE experiment, a first test of bound state QED calculations in extreme electromagnetic fields comes within reach. At the same time the knowledge obtained in the experiment paves the way for future trap assisted HFS measurements. With the SpecTrap experiment it is possible to store highly charged ions at temperatures down to <100 mK in a Penning trap and perform laser spectroscopy. With the ions cooled down the uncertainty introduced by the velocity distribution of the ions nearly vanishes and a precise transition wavelength determination up to $\frac{\Delta\lambda}{\lambda} = \mathcal{O}(10^{-7})$ is attainable [And12].

So far the total uncertainty on the HFS transition wavelength in lithium-like bismuth found with the LIBELLE beam time in 2011 is ±0.074 nm [Loc13]. To verify the result of the LIBELLE experiment by the SpecTrap experiment such a broad region has to be scanned in small wavelength steps by a tunable laser. With the soon published result of the LIBELLE beam time of 2014 [Ull15b] this region will be even more restrictive. Like this the LIBELLE experiment serves as valuable input to reduce the necessary measurement time, e.g. the time is already reduced to $3 \cdot 10^4$ s ≈ 0.5 d [Loc13] with the outcome of the analysis of 2011. With the SpecTrap experiment a more precise determination of the respective lifetime is possible as well. In combination the value for the bound g-factor in hydrogen- and lithium-like bismuth can be improved to enable a complementary QED test.

An adapted mirror system for XUV wavelength was constructed in this work and went through first test measurements. The results are in good agreement with simulations performed with SimIon and the system seems to be well understood.

Nevertheless the results suggest possibilities for further improvements. Especially the magnetic guidance can be optimized by a coil specially constructed for this set-up. The coil radius as well as the distance between the coils can be reduced to improve the

magnetic focus properties. It must be ensured in such scenario that the electric potentials applied at the electrodes and the MCP detector are sufficient to prevent the electrons to be magnetically reflected.

In addition, further tests should be performed, e.g. to determine the photo-detection efficiency. For this purpose a well defined light source with the well-defined wavelength is necessary.

Finally the set-up has to be installed at the ESR to be commissioned with an actual ion beam.

APPENDIX

A.1 Cabling of the LIBELLE experiment

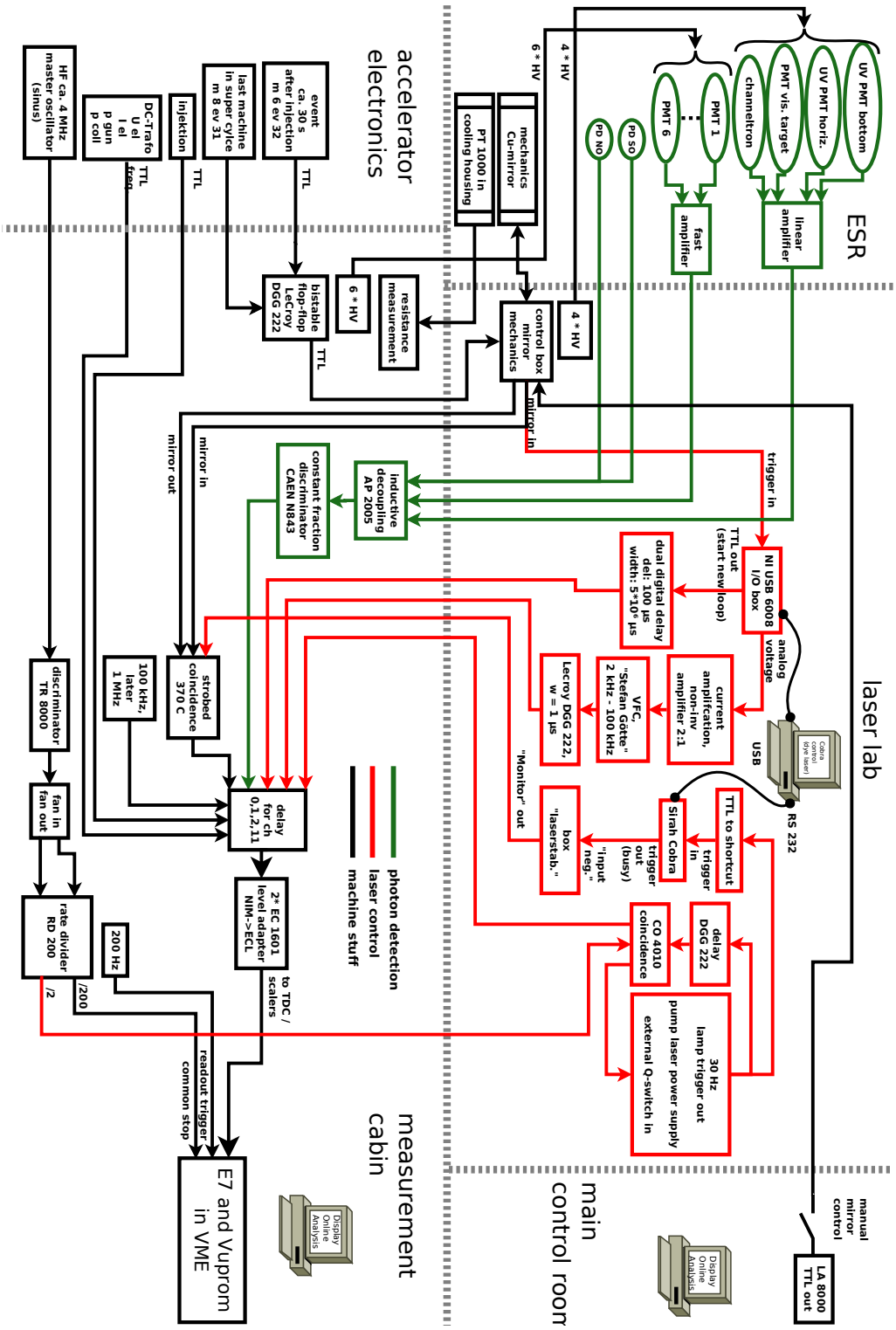

Figure A.1: Scheme of the cabling of the LIBELLE control and DAQ system [Loc13]

A.2 Implemented fit function with laser pulses

```
double fitfunction(Double_t *x, Double_t *par)
{
  double t        = *x;
  double N20      = par[0];
  double tau      = par[1];
  double tc       = par[2];
  double phi      = par[3];
  double N        = par[4];
  double scale    = par[5];
  double offs     = par[6];
  double t_period = par[7];
  double t_laser  = par[8];

  double g1 = 9;
  double g2 = 11;
  double a, b, f, N2tc;

  if(t <= tc)  f = scale * N20 * exp(-t/tau) + offs;
  else
  {
      double after_laser = (t-tc)/t_period;
      int    i_laser     = ((int)after_laser);
      double t_rest      = (after_laser - i_laser)*t_period;

      N2tc = N20 * exp(-tc/tau);
      a    = g2/g1 * N * phi/tau;
      b    = ((g2/g1 + 1)*phi + 1)/tau;

      int i = 0;
      double sum = N2tc;

      while (i<i_laser)
      {
        sum = (a/b+(sum-a/b)*exp(-b*t_laser))
              *exp(-(t_period-t_laser)/tau);
        i+=1;
      }

      if (t_rest<t_laser) sum = a/b+(sum-a/b)*exp(-b*t_rest);
      else
      {
         sum = (a/b+(sum-a/b)*exp(-b*t_laser))
               *exp(-(t_rest-t_laser)/tau);
      }
      f = scale * sum + offs;
    }
   return f;
}
```

A.3 Result comparison of two fit models

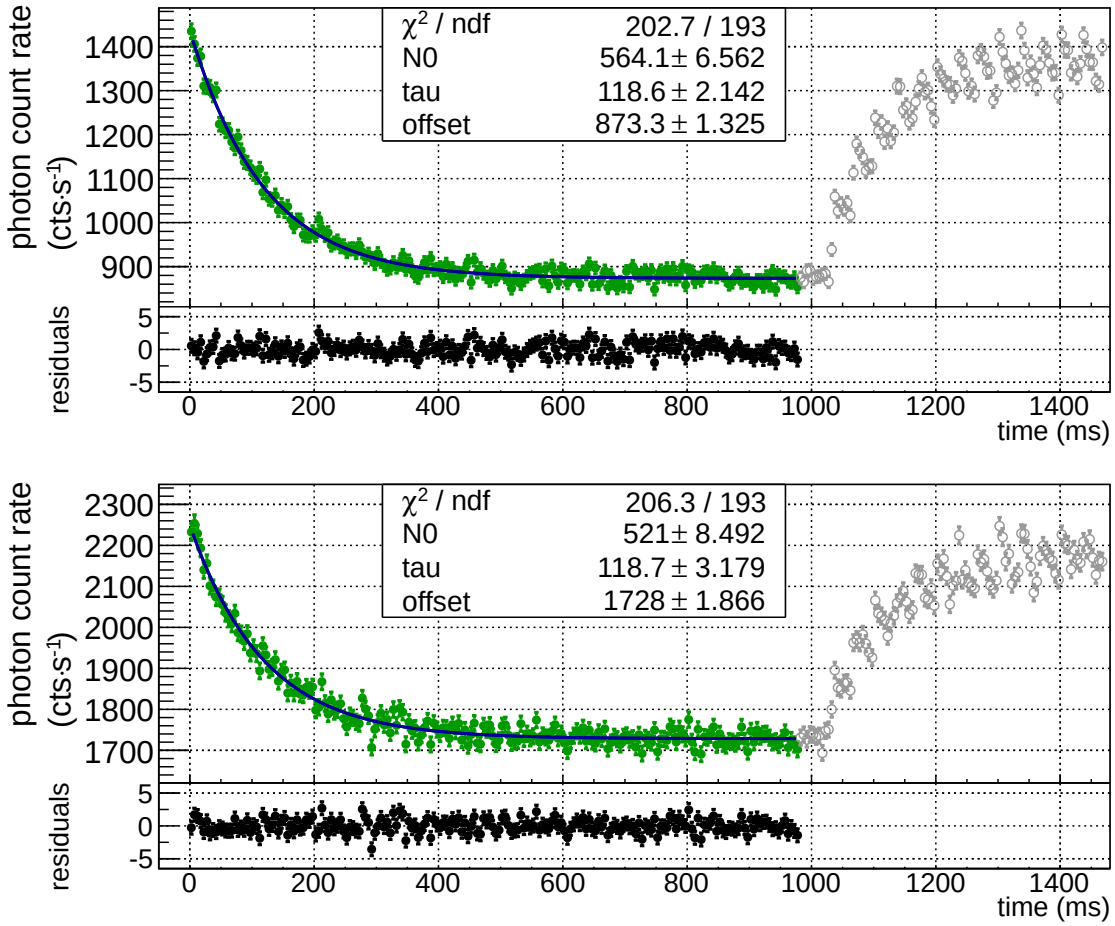

Figure A.2: $^{209}Bi^{80+}$lifetime data taken before (top) and after (bottom) the maintenance. The result is obtained via the bin-method from the dataset recorded with standard settings (I_{EC} = 250 mA and U_{RF} = 500 V). Signals within a $\pm 2.5\sigma$ window around bin 56 were used. While in fig. 4.28 the fit function accounts for the laser pulse structure, here the data was fitted with an exponential decay as a cross-check. Data taken before maintenance give a lifetime of (118.6 ± 2.1) ms with the simple fit function and (118.1 ± 1.8) ms with the extended fit function. Data taken after maintenance give a lifetime of (118.7 ± 3.2) ms with the simple fit function and (118.0 ± 2.3) ms with the extended fit function (cf. fig. 4.28). In both cases the results agree well within the uncertainty.

A.4 Technical drawing of the XUV detection system

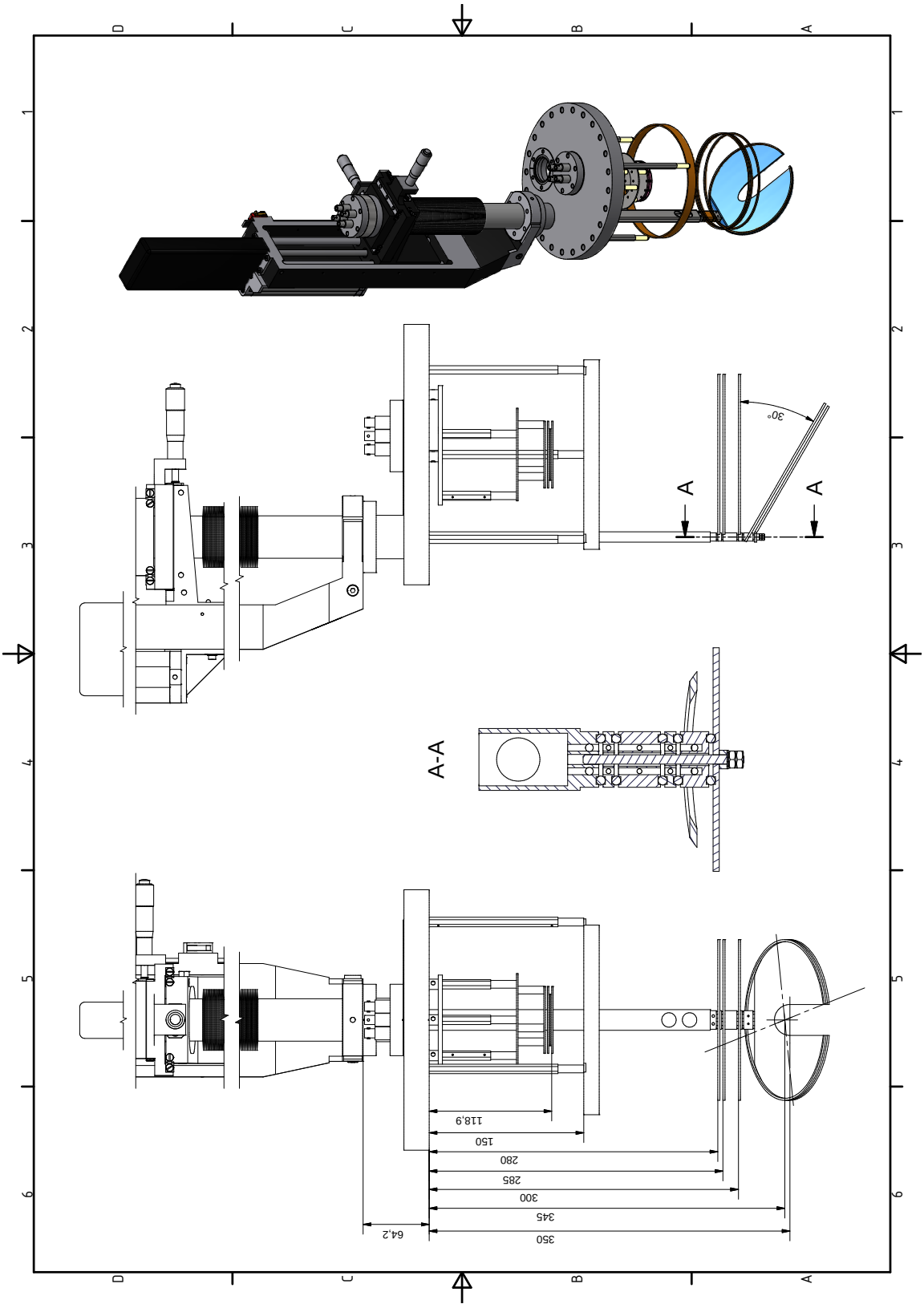

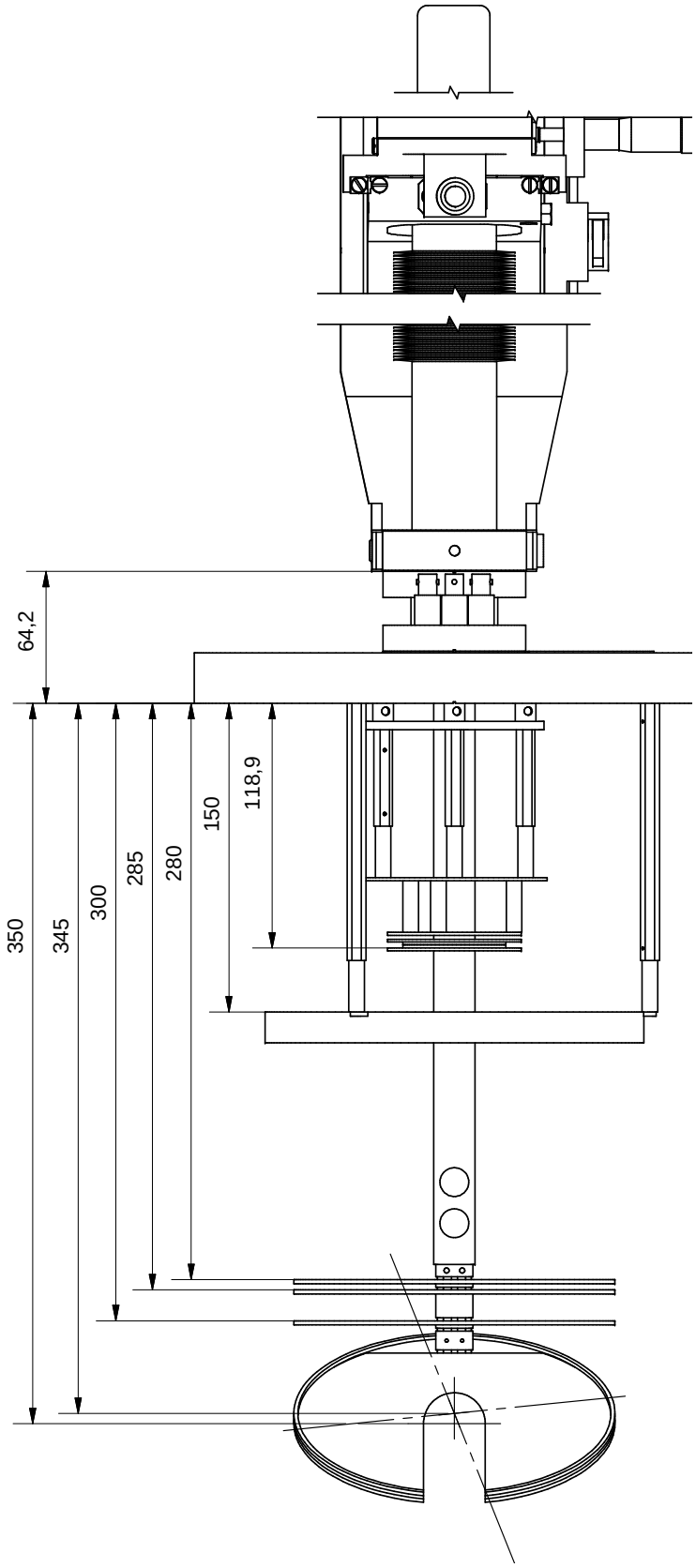

Figure A.3: Technical drawing of the XUV detection system. The MCP shielding is removed for better visibility.

BIBLIOGRAPHY

[And12] Andelkovic, Zoran: *Setup of a Penning trap for precision laser spectroscopy at HITRAP*, Johannes Gutenberg-Universität Mainz, Diss., 2012

[Ani10] Anielski, Denis: *Entwicklung eines Detektoraufbaus zur Bestimmung der 2s-Hyperfeinstrukturaufspaltung von $^{209}Bi^{80+}$ am Experimentierspeicherring an der GSI*, WWU Münster, Diss., 2010

[BBE+95] Borneis, S. ; Becker, St. ; Engel, T. ; Klaft, I. ; Klepper, O. ; Kohl, A. ; Kühl, T. ; Marx, D. ; Meier, K. ; Neumann, R. ; Schmitt, F. ; Seelig, P. ; Völker, L.: Population and spectroscopy of highly charged ions by laser induced recombination in the ESR. In: *AIP Conference Proceedings* 329 (1995), Nr. 1, 150-156. http://dx.doi.org/http://dx.doi.org/10.1063/1.47601. – DOI http://dx.doi.org/10.1063/1.47601

[BE66] Brodsky, Stanley J. ; Erickson, Glen W.: Radiative Level Shifts. III. Hyperfine Structure in Hydrogenic Atoms. In: *Phys. Rev.* 148 (1966), Aug, 26–46. http://dx.doi.org/10.1103/PhysRev.148.26. – DOI 10.1103/PhysRev.148.26

[Bei00] Beier, Thomas: The gj factor of a bound electron and the hyperfine structure splitting in hydrogenlike ions. In: *Physics Reports* 339 (2000), Nr. 2–3, 79 - 213. http://dx.doi.org/http://dx.doi.org/10.1016/S0370-1573(00)00071-5. – DOI http://dx.doi.org/10.1016/S0370–1573(00)00071–5. – ISSN 0370–1573

[BHB83] B. H. Bransden, C. J. J.: *Physik of atoms and molecules*. Longman Scientific and Technical, 1983

[BLP+00] Beier, Thomas ; Lindgren, Ingvar ; Persson, Hans ; Salomonson, Sten ; Sunnergren, Per ; Häffner, Hartmut ; Hermanspahn, Nikolaus: g_j factor of an electron bound in a hydrogenlike ion. In: *Phys. Rev. A* 62 (2000), Aug, 032510. http://dx.doi.org/10.1103/PhysRevA.62.032510. – DOI 10.1103/PhysRevA.62.032510

[Dem05] Demtröder, Wolfgang: *Experimentalphysik 3*. Springer Berlin Heidelberg, 2005

[Dem06] Demtröder, Wolfgang: *Experimentalphysik 2*. Springer Berlin Heidelberg, 2006

[HAG+13] Hannen, V ; Anielski, D ; Geppert, C ; Jöhren, R ; Kühl, T ; Lochmann, M ; López-Coto, R ; Nörtershäuser, W ; Ortjohann, H W. ; Sánchez, R ; Vollbrecht, J ; Weinheimer, C ; Winters, D F A.: Detection system for forward emitted photons at the Experimental Storage Ring at GSI. In: *Journal of Instrumentation* 8 (2013), Nr. 09, P09018. http://stacks.iop.org/1748-0221/8/i=09/a=P09018

[HH04] H. Haken, H. Ch. W.: *Atom- und Quantenphysik*. Springer Berlin Heidelberg, 2004

[HSA77] Henke, Burton L. ; Smith, Jerel A. ; Attwood, David T.: 0.1–10 keV x-ray induced electron emissions from solids. Models and secondary electron measurements. In: *Journal of Applied Physics* 48 (1977), Nr. 5, 1852-1866. http://dx.doi.org/http://dx.doi.org/10.1063/1.323938. – DOI http://dx.doi.org/10.1063/1.323938

[Jö13] Jöhren, Raphael: *Spectroscopy of the hyperfine transition in lithium like bismuth at the ESR at GSI and an APD based single photon detector for laser spectroscopy on highly charged ions*, WWU Münster, Diss., 2013

[KBE+94] Klaft, I. ; Borneis, S. ; Engel, T. ; Fricke, B. ; Grieser, R. ; Huber, G. ; Kühl, T. ; Marx, D. ; Neumann, R. ; Schröder, S. ; Seelig, P. ;

Völker, L.: Precision Laser Spectroscopy of the Ground State Hyperfine Splitting of Hydrogenlike $^{209}Bi^{82+}$. In: *Phys. Rev. Lett.* 73 (1994), Oct, 2425–2427. http://dx.doi.org/10.1103/PhysRevLett.73.2425. – DOI 10.1103/PhysRevLett.73.2425

[KKW+97] Kohl, A. ; Kühl, T. ; Winter, H. ; Bruske, C. ; Dax, A. ; Engel, T. ; Faber, S. ; Gerlach, M. ; Heeg, P. ; Klepper, O. ; Marx, D. ; Meier, K. ; Schmitt, F. ; Seelig, P. ; Würtz, M.: A new detector for laser induced recombination at the ESR. In: *Hyperfine Interactions* 108 (1997), Nr. 1-3, 319-324. http://dx.doi.org/10.1023/A:1012679200515. – DOI 10.1023/A:1012679200515. – ISSN 0304–3843

[Kla94] Klaft, Ingo: *Messung der Hyperfeinstruktur im Grundzustand von wasserstoffartigem $^{209}Bi^{82+}$ am Schwerionen-Speicherring ESR*, Mainz, Diss., 1994

[LJG+14] Lochmann, Matthias ; Jöhren, Raphael ; Geppert, Christopher ; Andelkovic, Zoran ; Anielski, Denis ; Botermann, Benjamin ; Bussmann, Michael ; Dax, Andreas ; Frömmgen, Nadja ; Hammen, Michael ; Hannen, Volker ; Kühl, Thomas ; Litvinov, Yuri A. ; López-Coto, Rubén ; Stöhlker, Thomas ; Thompson, Richard C. ; Vollbrecht, Jonas ; Volotka, Andrey ; Weinheimer, Christian ; Wen, Weiqiang ; Will, Elisa ; Winters, Danyal ; Sánchez, Rodolfo ; Nörtershäuser, Wilfried: Observation of the hyperfine transition in lithium-like bismuth $^{209}Bi^{80+}$: Towards a test of QED in strong magnetic fields. In: *Phys. Rev. A* 90 (2014), Sep, 030501. http://dx.doi.org/10.1103/PhysRevA.90.030501. – DOI 10.1103/PhysRevA.90.030501

[Loc13] Lochmann, Matthias: *Spectroscopy of the hyperfine transition in lithium like bismuth at the ESR at GSI and an APD based single photon detector for laser spectroscopy on highly charged ions*, Johannes Gutenberg-Universität Mainz, Diss., 2013

[MOS+04] Moskovkin, D. L. ; Oreshkina, N. S. ; Shabaev, V. M. ; Beier, T. ; Plunien, G. ; Quint, W. ; Soff, G.: g factor of hydrogenlike ions with nonzero nuclear spin. In: *Phys. Rev. A* 70 (2004), Sep, 032105.

http://dx.doi.org/10.1103/PhysRevA.70.032105. – DOI 10.1103/PhysRevA.70.032105

[MSQ08] Moskovkin, D.L. ; Shabaev, V.M. ; Quint, W.: g factor of Li-like ions with a nonzero nuclear spin. In: *Optics and Spectroscopy* 104 (2008), Nr. 5. http://dx.doi.org/10.1134/S0030400X08050019. – DOI 10.1134/S0030400X08050019. – ISSN 0030–400X

[NLJ+13] Nörtershäuser, Wilfried ; Lochmann, Matthias ; Jöhren, Raphael ; Geppert, Christopher ; Andelkovic, Zoran ; Anielski, Denis ; Botermann, Benjamin ; Bussmann, Michael ; Dax, Andreas ; Frömmgen, Nadja ; Hammen, Michael ; Hannen, Volker ; Kühl, Thomas ; Litvinov, Yuri A. ; Volbrecht, Jonas ; Stöhlker, Thomas ; Thompson, Richard C. ; Weinheimer, Christian ; Wen, Weiqiang ; Will, Elisa ; Winters, Danyal ; Sánchez, Rodolfo M.: First observation of the ground-state hyperfine transition in 209 Bi 80+. In: *Physica Scripta* 2013 (2013), Nr. T156, 014016. http://stacks.iop.org/1402-4896/2013/i=T156/a=014016

[Nö11] Nörtershäuser, Wilfried: Laser spectroscopy for QED tests in highly charged ions. In: *Hyperfine Interactions* 199 (2011), Nr. 1-3, 131-140. http://dx.doi.org/10.1007/s10751-011-0315-7. – DOI 10.1007/s10751–011–0315–7. – ISSN 0304–3843

[PPI73] Pyykkö, P. ; Pajanne, E. ; Inokuti, Mitio: Hydrogen-like relativistic corrections for electric and magnetic hyperfine integrals. In: *International Journal of Quantum Chemistry* 7 (1973), Nr. 4, 785–806. http://dx.doi.org/10.1002/qua.560070415. – DOI 10.1002/qua.560070415. – ISSN 1097–461X

[Rag89] Raghavan, Pramila: Table of nuclear moments. In: *Atomic data and nuclear data tables* 42 (1989), S. 189–291

[Roe15] RoentDek: *MCP detector with timing anode. Manual for MCP ToF detector DET40/75*, 2015. www.roentdek.com

[Roi15] Roithner, LaserTechnik G.: *UVTOP260 data-sheet*, 2015. http://www.roithner-laser.com/led_deepuv.html

[San12] Sanchez, R: *private communication*. GSI Darmstadt, 2012

[SAY+01] Shabaev, V. M. ; Artemyev, A. N. ; Yerokhin, V. A. ; Zherebtsov, O. M. ; Soff, G.: Towards a Test of QED in Investigations of the Hyperfine Splitting in Heavy Ions. In: *Phys. Rev. Lett.* 86 (2001), Apr, 3959–3962. http://dx.doi.org/10.1103/PhysRevLett.86.3959. – DOI 10.1103/PhysRevLett.86.3959

[SAZ+00] Shabaev, V.M. ; Artemyev, A.N. ; Zherebtsov, O.M. ; Yerokhin, V.A. ; Plunien, G. ; Soff, G.: Calculation of the hyperfine structure of heavy H and Li like ions. In: *Hyperfine Interactions* 127 (2000), Nr. 1-4, 279-286. http://dx.doi.org/10.1023/A:1012616322709. – DOI 10.1023/A:1012616322709. – ISSN 0304–3843

[See99] Seelig, Peter: *Laserspektroskopie der 1s-Hyperfeinstrukturaufspaltung an wasserstoffähnlichem* $^{207}Pb^{81+}$, Mainz, Diss., 1999

[Sha98] Shabaev, V M.: Transition probability between the hyperfine structure components of hydrogenlike ions and bound-electron g-factor. In: *Canadian Journal of Physics* 76 (1998), Nr. 11, 907-910. http://dx.doi.org/10.1139/p98-064. – DOI 10.1139/p98–064

[Sha15] Shabaev, V M.: *private communication*. Department of Physics, St. Petersburg State University, July 2015

[Sim15] SimIon: *Industry standard charged particle optics simulation software.* http://www.simion.com/. Version: 2015

[SST+98] Shabaev, V. M. ; Shabaeva, M. B. ; Tupitsyn, I. I. ; Yerokhin, V. A. ; Artemyev, A. N. ; Kühl, T. ; Tomaselli, M. ; Zherebtsov, O. M.: Transition energy and lifetime for the ground-state hyperfine splitting of high-Z lithiumlike ions. In: *Phys. Rev. A* 57 (1998), Jan, 149–156. http://dx.doi.org/10.1103/PhysRevA.57.149. – DOI 10.1103/PhysRevA.57.149

[STK+97] Shabaev, V. M. ; Tomaselli, M. ; Kühl, T. ; Artemyev, A. N. ; Yerokhin, V. A.: Ground-state hyperfine splitting of high-Z hydrogenlike ions. In: *Phys. Rev. A* 56 (1997), Jul, 252–255. http://dx.doi.org/10.1103/PhysRevA.56.252. – DOI 10.1103/PhysRevA.56.252

[Tri15] Trittmaack, Florian: *TBA*, WWU Münster, Diplomarbeit, 2015

[UAD+15] Ullmann, Johannes ; Andelkovic, Zoran ; Dax, Andreas ; Geithner, Wolfgang ; Geppert, Christopher ; Gorges, Christian ; Hammen, Michael ; Hannen, Volker ; Kaufmann, Simon ; König, Kristian ; Litvinov, Yuri ; Lochmann, Matthias ; Maass, Bernhard ; Meisner, Johann ; Murböck, Tobias ; Sánchez, Rodolfo ; Schmidt, Matthias ; Schmidt, Stefan ; Steck, Markus ; Stöhlker, Thomas ; Thompson, Richard C. ; Vollbrecht, Jonas ; Weinheimer, Christian ; Nörtershäuser, Wilfried: An improved value for the hyperfine splitting of hydrogen-like 209 Bi 82+. In: *Journal of Physics B: Atomic, Molecular and Optical Physics* 48 (2015), Nr. 14, 144022. http://stacks.iop.org/0953-4075/48/i=14/a=144022

[Ull15a] Ullmann, J: *private communication.* October 2015

[Ull15b] Ullmann, Johannes: *PhD thesis, in preparation*, Diss., 2015

[VGA+12] Volotka, A. V. ; Glazov, D. A. ; Andreev, O. V. ; Shabaev, V. M. ; Tupitsyn, I. I. ; Plunien, G.: Test of Many-Electron QED Effects in the Hyperfine Splitting of Heavy High-Z Ions. In: *Phys. Rev. Lett.* 108 (2012), Feb, 073001. http://dx.doi.org/10.1103/PhysRevLett.108.073001. – DOI 10.1103/PhysRevLett.108.073001

[VGT+08] Volotka, A. V. ; Glazov, D. A. ; Tupitsyn, I. I. ; Oreshkina, N. S. ; Plunien, G. ; Shabaev, V. M.: Ground-state hyperfine structure of H-, Li-, and B-like ions in the intermediate-Z region. In: *Phys. Rev. A* 78 (2008), Dec, 062507. http://dx.doi.org/10.1103/PhysRevA.78.062507. – DOI 10.1103/PhysRevA.78.062507

[WBD+98] Winter, Helmut ; Borneis, S. ; Dax, A. ; Faber, S. ; Kühl, T. ; Marx, D. ; Schmitt, F. ; Seelig, P. ; Seelig, W.: Bound electron f-

factor in hydrogen-like Bismuth. In: *Gesellschaft für Schwerionenforschung: Scientific report 1998. Darmstadt: GSI, 1999. S. 87 (GSI; 99-1)* (1998), January. http://tubiblio.ulb.tu-darmstadt.de/9206/

[Win99] Winter, Helmut: *Laserspektroskopie an schweren Ionen: Laserinduzierte Zweistufen-Rekombination, Hyperfeinstrukturaufspaltung und g-faktor des gebundenen Elektrons*, TU Darmstadt, Diss., 1999

[WKS+11] Winters, D F A. ; Kühl, Th ; Schneider, D H. ; Indelicato, P ; Reuschl, R ; Schuch, R ; Lindroth, E ; Stöhlker, Th: Laser spectroscopy of the (1s 2 2s2p) 3 P 0 – 3 P 1 level splitting in Be-like krypton. In: *Physica Scripta* 2011 (2011), Nr. T144, 014013. http://stacks.iop.org/1402-4896/2011/i=T144/a=014013